2016

Growth and Characterization of Wide Bandgap Quaternary BeMgZnO Thin Films and BeMgZnO/ZnO Heterostructures

Mykyta Toporkov
Virginia Commonwealth University

Growth and Characterization of Wide Bandgap Quaternary BeMgZnO Thin Films and

BeMgZnO/ZnO Heterostructures

A dissertation submitted in partial fulfillment of the requirements

for the degree of Doctor of Philosophy at Virginia Commonwealth University.

by

Mykyta Toporkov

Committee in charge

Prof Özgür, Ümit (Director)

Prof. Morkoç, Hadis

Prof. Avrutin, Vitaliy

Prof. Reshchikov, Michael

Prof. Demchenko, Denis

Prof. Baski, Alison

Electrical and Computer Engineering

Virginia Commonwealth University

Richmond, Virginia

May 2016

Abstract

This thesis reports a comprehensive study of quaternary BeMgZnO alloy and BeMgZnO/ZnO heterostructures for UV-optoelectronics electronic applications. It was shown that by tuning Be and Mg contents in the heterostructures, high carrier densities of two-dimensional electron gas (2DEG) are achievable and makes its use possible for high power RF applications. Additionally, optical bandgaps as high as 5.1 eV were achieved for single crystal wurtzite material which allows the use of the alloy for solar blind optoelectronics (E_g>4.5eV) or intersubband devices.

A systematic experimental and theoretical study of lattice parameters and bandgaps of quaternary BeMgZnO alloy was performed for the whole range of compositions. Composition independent bowing parameters were determined which allows accurate predictions of experimentally measured values.

The BeMgZnO thin films were grown by plasma assisted molecular beam epitaxy (P-MBE) in a wide range of compositions. The optimization of the growth conditions and its effects on the material properties were explored. The surface morphology and electrical characteristics of the films grown on (0001) sapphire were found to critically depend on the metal-to-oxygen ratio. Samples grown under slightly oxygen-rich conditions exhibited the lowest RMS surface roughness (as low as 0.5 nm). Additionally, the films grown under oxygen-rich conditions were semi-insulating ($>10^5$ $\Omega{\cdot}cm$), while the films grown under metal-rich conditions were semiconducting ($\sim10^2$ $\Omega{\cdot}cm$). Additionally, with increasing bandgap Stokes shift increases, reaching ~0.5 eV for the films with 4.6 eV absorption edge suggests the presence of band tail states introduced by potential fluctuations and alloying.

From spectrally resolved PL transients, BeMgZnO films grown on a GaN/sapphire template having higher Mg/Be content ratio exhibit smaller localization depth and brighter photoluminescence at low temperatures. The optimum content ratio for better room temperature optical performance was found to be ~2.5.

The BeMgZnO material system and heterostructures are promising candidates for the device fabrication. 2DEG densities of MgZnO/ZnO heterostructures were shown to improve significantly (above 10^{13} cm^{-2}) by adding even a small amount of Be (1-5%). As an essential step toward device fabrication, reliable ohmic contacts to ZnO were established with remarkably low specific contact resistivities below 10^{-6} Ohm-cm^2 for films with 10^{18} cm^{-3} carrier density.

Executive Summary

Zinc oxide (ZnO) based semiconductor materials are highly attractive for a wide range of optical and electronic device applications due to their direct wide bandgap (Eg~3.3 eV for ZnO at 300K), large excitonic binding energy (~60 meV for ZnO), optical transparency in highly conductive state, and scalability to large volume native substrates. Alloying ZnO with BeO and MgO allows tuning of optical and electronic properties, inclusive of bandgap, band offsets, lattice parameters, and spontaneous polarization. However, compositions, and therefore, tunability achievable in MgZnO and BeZnO ternaries are restricted by limited solubility of BeO and MgO in wurtzite ZnO lattice and the associated phase segregation. Quaternary alloy BeMgZnO alleviates these limitations, and is attractive particularly for solar blind photodetectors, intersubband transition devices, and heterostructures with two-dimensional electron gas (2DEG) as well as light emitting devices. This thesis is dedicated to synthesis and investigation of structural, electrical, and optical properties of quaternary BeMgZnO thin films and (Be,Mg)ZnO/ZnO heterostructures with 2DEG.

$Be_xMg_yZn_{1-x-y}O$ thin films with a wide range of compositions of $x = 0 – 0.19$ and $y = 0 – 0.52$ were grown by plasma assisted molecular beam epitaxy (MBE) on (0001) sapphire substrates. Optical bandgaps as high as 5.1 eV were achieved for single crystal wurtzite material. Using the atomic compositions measured (1-2 atom % uncertainty) by means of a combination of nondestructive Rutherford backscattering spectrometry with He^+ analyzing ion beam and non-Rutherford elastic backscattering experiments with high energy protons, composition independent ternary BeZnO and MgZnO bowing parameters were determined for a and c lattice parameters and the bandgap. It was shown that precise control over lattice parameters by tuning the quaternary

composition would allow strain control in $Be_xMg_yZn_{1-x-y}O/ZnO$ heterostructures with the possibility to achieve both compressive and tensile strain, where the latter supports formation of 2DEG at the interface with ZnO.

The surface morphology and electrical properties of BeMgZnO thin films on grown on (0001) sapphire were found to critically depend on the metal-to-oxygen ratio. Samples grown under slightly oxygen-rich conditions (metal-to-oxygen ratio ~0.9) showed nearly 2D growth mode and exhibited the lowest RMS surface roughness (as low as 0.5 nm). Additionally, the films grown under oxygen-rich conditions were semi-insulating ($>10^5$ $\Omega\cdot$cm), while the films grown under metal-rich conditions were more conductive (~10^2 $\Omega\cdot$cm).

To explore the further effect of growth conditions on the incorporation rate of Zn, Mg and Be during plasma-assisted MBE growth of quaternary alloy BeMgZnO, the effect of oxygen to metal (Be+Mg+Zn) ratio was investigated. Samples grown under fixed metal fluxes showed bandgap widening and c lattice parameter shrinking with reduced oxygen flow due to relative increase of Be and Mg content. This dependence may be explained by the differences in formation energies of the binary compounds.

$Be_xMg_yZn_{1-x-y}O$ thin films were found to exhibit strong Stokes shift, which increased with bandgap, reaching ~0.5 eV for BeMgZnO grown on c-sapphire with 4.6 eV absorption edge suggesting the presence of band tail states introduced by potential fluctuations and alloying.

To improve the quality of the alloy, O-polar and Zn-polar $Be_xMg_yZn_{(1-x-y)}O$ samples were grown on GaN templates that offer high structural quality and low lattice mismatch (only 1.9% compared to 18% on sapphire for ZnO thin films).

The performance of heterostructure devices is highly sensitive to the material quality, which is governed by defects. Carrier dynamics are extremely sensitive to the type and quality of defects

and can be used as a powerful measure of material characteristics. The carrier lifetimes are also strongly affected by carrier localization, which is well pronounced in wide-bandgap semiconductor alloys due to large differences in metal covalent radii and the lattice constants of the binaries. These differences result in strain-driven compositional variations within the film and consequently large potential fluctuations, in addition to that possibly caused by defects. To investigate the effects of localization in Zn-polar BeMgZnO quaternary alloys, temperature-dependent carrier dynamics were investigated by time resolved photoluminescence (TRPL). From spectrally resolved PL transients, BeMgZnO samples with higher Mg/Be content ratio were found to exhibit smaller localization depth for $Be_{0.03}Mg_{0.18}Zn_{0.79}O$ ($r_{Mg/Be}$=6) compared to $Be_{0.11}Mg_{0.15}Zn_{0.74}O$ ($r_{Mg/Be}$=1.4). Similar correlation was observed in temporal redshift of the PL peak position that originates from removal of the band filling effect in the localized states. The S-shaped behavior of PL peak with change in temperature was observed for the quaternary alloy $Be_{0.04}Mg_{0.17}Zn_{0.79}O$ ($r_{Mg/Be}$=4.3). The carriers were found to be localized even above room temperature in $Be_{0.11}Mg_{0.15}Zn_{0.74}O$ ($r_{Mg/Be}$ =1.4). Additionally, the inverse proportionality of low temperature PL intensity and $r_{Mg/Be}$ content ratio was observed. However, at room temperature this proportionality was broken. With reducing $r_{Mg/Be}$, the compensation effect between Mg and Be weakens, which increases both number of defects as well as strain induced localization, Δ_0. Since localization depth and defect density are somewhat coupled, there exists an optimum $r_{Mg/Be}$ content ratio, which was found to be in the vicinity of 2.5 for the highest optical efficiency.

The quaternary BeMgZnO material was also considered as a barrier material to explore heterostructures with 2DEG and their device potential. 2DEG densities, limited to 7.5 x 10^{12} cm^{-2} in O-polar MgZnO/ZnO heterostructures (for 45% of Mg), were shown to improve significantly to above 10^{13} cm^{-2} with the quaternary BeMgZnO barrier having even a small amount of BeO

content (1-5 %). As another essential component to development of devices based on these structures, reliable Ohmic contacts to ZnO were established with remarkably low specific contact resistivities below 10^{-6} Ohm-cm^2 for films with 10^{18} cm^{-3} carrier density. Further optimization of BeMgZnO/ZnO heterostructures with 2DEG and establishment of Schottky contacts with large barrier height would lead to ZnO-based high speed heterostructure field effect transistors.

Acknowledgments

First of all, I greatly appreciate the support and help of my advisor Professor Ümit Özgür. Over all my graduate studies at Virginia Commonwealth University (VCU) he gave me exceptional professional guidance and personal support. He had the most influential effect on the completion of this work. I'm also grateful to Professor Hadis Morkoç for numerous discussions and feedback on my research. I'm thankful to Dr. Vitaliy Avrutin for his guidance and priceless help with experiments and systems support. I also greatly appreciate help from Dr. Huiyong Liu for his patience and support during my initial training and adaptation at VCU. I'm confident that it would be much easier for me if he stayed at VCU longer. Nevertheless, working with him was an honor for me.

I have a deep appreciation for Dr. Janos Volk for countless discussions, suggestions and laughs. He is always a reminder for me of how one can be passionate and happy with the research he is doing despite copious hurdles of experimental work and disappointments with results.

I'm especially grateful to Professor Denis Demchenko for theoretical calculations of lattice parameters, bandgaps and formation energies as well as useful insights into underlying physical phenomena of the formation and the quaternary alloy. I appreciate the efforts that he has made in my development as a researcher and numerous discussions required by this study.

I'm grateful to Professor Michael Reshchikov for his teaching and many patient discussion and conversations on the optical characterizations. I'm also thankful to Dr. Emilis Šermukšnis for his invaluable noise measurements and discussions and discussion of random processes. I'm also grateful to Dr. Zsolt Zolnai for necessary ion beam analysis and valuable suggestions on the composition evaluations.

I cannot give ample thanks to all my lab mates who were my colleagues, classmates and friends without whose help I most likely would not been able to finish most of my experiments. These titans are Shopan Hafiz, Barkat Ullah, Serdal Okur, Saikat Das, Morteza Monavarian, Mahbub Alam and Tanner Nakagawara.

Most importantly, I want to thank to my parents and my family Olga Perfilieva and Eric Wirth and my friend Roger York for their constant love, encouragement, and support. They made and make me a better person as well as better researcher.

Table of Consents

List of Figures

xvii

List of Tables

Introduction

Zinc oxide (ZnO) based materials have attracted a great deal of interest in recent years due to their direct wide bandgap (Eg~3.3 eV for ZnO at 300K), large excitonic binding energy (~60 meV for ZnO), optical transparency in highly conductive state, and scalability to large volume native substrates.[1,2] In regard to potential applications, ZnO shares some similarities with another wide-gap semiconductor, GaN, (Eg~3.4 eV at 300K) which is widely used in production of light emitting diodes (LED) and heterostructure field effect transistors (HFETs). However, reliable and reproducible p-type conductivity has not been achieved as yet which limits many potential applications of ZnO.

1.1. ZnO family of materials

Figure 1 shows bandgaps and in-plane lattice parameters for ZnO related family of materials. The solid line and shaded area between binaries in wurtzite phase corresponds to wurtzite ternary and quaternary alloys, respectively.

1
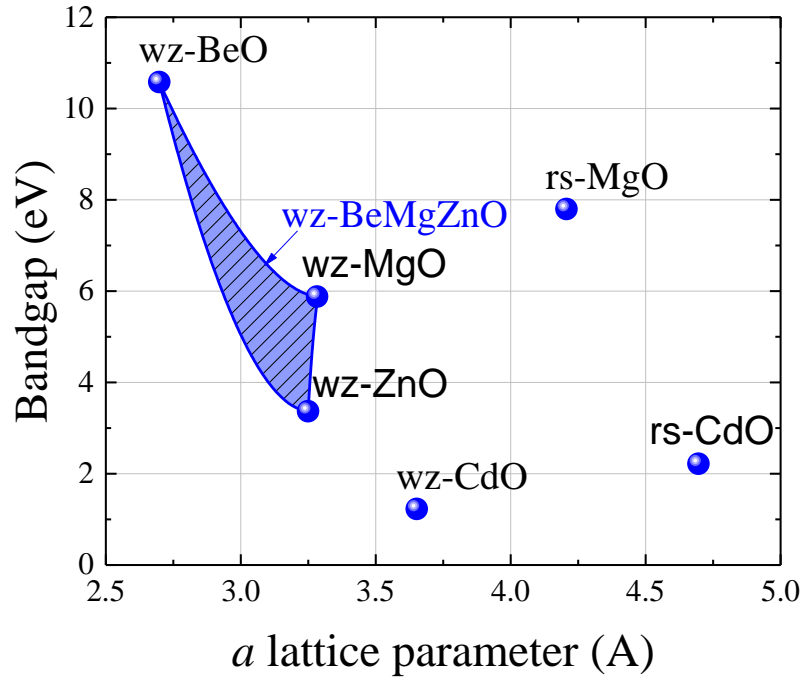
Figure 1. Bandgap and in-plane lattice parameter a for ZnO family of materials. The solid line and shaded area between binaries in wurtzite phase correspond to wurtzite ternary and quaternary alloys, respectively. The parameters for wz-CdO are calculated in Ref. 3.

Table 1 summarizes bandgaps and lattice parameters for the related binaries and compares them with other theoretical results and representative experimental values. Alloying ZnO with MgO (7.8 eV bandgap in stable rock-salt phase) is conventionally used to increase the bandgap. However, MgO has a cubic rocksalt lattice, and therefore, the ternary MgZnO alloy provides limited bandgap tuning in the wurtzite phase (wurtzite MgO bandgap 5.88 eV). Consequently, phase segregation becomes inevitable as the Mg content of the MgZnO solid solution increases. Ohtomo et al.[4] and Sharma et al.[5] were able to tune the bandgap to ~4 eV for wurtzite MgZnO alloys containing 33% and 36% Mg, respectively. The second-phase formation at higher Mg contents could be suppressed only at low growth temperatures at the expense of inferior material

quality: 55% Mg incorporation to ZnO in wurtzite phase and a corresponding absorption edge of 4.55 eV have been achieved by Du *et al.*[6] using plasma assisted molecular beam epitaxy (P-MBE) at a substrate temperature of 250 °C. It has been also possible to achieve metastable cubic phase MgZnO with even higher Mg content by mainly reducing the growth temperature.[7] A caveat in this case, however, is the loss of semiconductor functionally (the cubic material is an insulator rather than a semiconductor). It should also be noted that supersaturated solid solutions are unstable against exposure to elevated temperatures during thermal treatments or device operation, which can trigger the second-phase formation and limit their practical use.

The alternative BeZnO ternary alloy has been proposed[8] to be more advantageous compared to MgZnO as it is expected to maintain the wurtzite structure for the whole compositional range, and therefore, provide a wide range of bandgap tuning, potentially up to that of BeO (10.6 eV). However, despite the initial optimistic report of bandgap modulation up to 5.4 eV in BeZnO,[8] recent studies[9,10] indicate that $Be_xZn_{1-x}O$ solid solutions with intermediate Be composition are unstable and segregate into low- and high-Be content phases due to the large lattice mismatch of the binary constituents and large covalent radii difference between Zn and Be (1.22 Å for Zn, 0.96 Å for Be[11]), making it difficult to incorporate intermediate concentrations of Be to the ZnO lattice. The phase segregation has been observed for Be contents as low as 10%.[9,12,13]

To overcome the abovementioned limitations of the MgZnO and BeZnO ternaries and suppress phase segregation, the quaternary BeMgZnO alloy can be used with achievable bandgaps above 5 eV.[12,14–17] The advantage of this quaternary system is that Mg has a much larger covalent radius (1.41 Å)[11] than Be and can compensate for the large lattice mismatch between ZnO and BeO. Therefore, it is expected that by tuning the compositions of both BeO and MgO in ZnO (i.e. Be/Mg ratio) one can achieve lattice matching to ZnO, prevent phase separation driven by the radii

3

difference, and achieve wider bandgaps. Up until now, the growth of single crystal quaternary BeMgZnO has been limited to growths on c-plane sapphire,[15,16,18–22] quartz,[23,24] silicon[23] and GaN;[25] and the explored growth techniques are MBE,[15,19,21,22] PLD,[16,18,20,23] sputtering[24,25] and sol-gel synthesis[26].

One of the attractive applications of the quaternary BeMgZnO alloy is the HFETs. In order to achieve efficient ZnO based HFETs the following conditions must be satisfied:

- high quality of ZnO layer that will serve as a medium for 2DEG layer and high quality barrier layer that will provide proper spontaneous and piezoelectric polarization for the formation of 2DEG;

- optimized growth conditions to achieve a heterostructure with 2DEG;

- low specific contact resistivity ohmic contacts for Source and Drain electrodes;

- large barrier height and low leakage current Schottky contact for Gate electrode.

		Theory				Experiment			
		a, Å	c, Å	u	E_g, eV	a, Å	c, Å	u	E_g, eV
ZnO (wz)	This work	3.30 3.166[a]	5.285 5.070[a]	0.378 0.380[a]	3.43 HSE06-0.375 2.48[b] HSE06-0.25 2.12-3.2[c] GW 0.74[d] GGA	3.252 3.2475 - 3.2501[e]	5.203 5.2042 - 5.241[e]	- 0.3817 - 0.3856[e] 0.3817[f]	3.26 3.43 (LT)
MgO (wz)	This work	3.32 3.221[a]	5.056 5.040[a]	0.386 0.386[a]	5.87 HSE06-0.375 5.21[b] HSE06-0.25 7.16[g] GW 3.78[h] LDA	3.283[i]	5.095[i]	0.388[i]	5.88[j]
MgO (rock-salt)	This work	4.17 0.421[k]	N/A	N/A	7.72 HSE06-0.375 6.67[b] HSE06-0.25 8.2-9.16[l] GW 4.34[m] GGA	- 4.207[n] 4.211[o]	N/A	N/A	- 7.77[p] 7.7[q]
BeO (wz)	This work	2.72 2.738[r]	4.393 4.449[r]	0.378 0.377[s]	10.20 HSE06-0.375 10.09[t] HSE06-0.25 10.8[u] GW 8.49[v] GGA	- 2.698[w]	- 4.3776[w]	- 0.378[x]	- 10.63[y]

[a] LDA+U to DFT with ultrasoft pseudopotentials [Ref. 27]
[b] Untuned HSE06 with fraction of exact exchange equal 0.25 [Ref. 28]
[c] Various GWs. [Ref. 29]
[d] GGA [Ref. 30]
[e] XRD and energy-dispersive X-ray spectroscopy (EDX) [Ref. 31]
[f] Powder neutron diffraction. [Ref. 32]
[g] G0W0 [Ref. 28]
[h] LDA to DFT [Ref. 33]
[i] Extrapolation of the experimental data [Ref. 27]
[j] Extrapolation of the experimental data [Ref. 34]
[k] GGA(PAW) to DFT[Ref. 35]
[l] Various GWs [Ref. 36]
[m] GGA(PBE) to DFT [Ref. 37]
[n] XRD [Ref. 38]
[o] XRD [Ref.39]
[p] Reflectance [Ref. 40]
[q] Reflectance [Ref. 41]
[r] GGA(PBE) to DFT [Ref. 42]
[s] DFT in the framework of the periodic linear combination of atomic orbitals (LCAO) approximation [Ref. 43]
[t] Untuned HSE06 with fraction of exact exchange equal 0.25 [Ref. 44]
[u] GW [Ref. 45]
[v] GGA(PBE) to DFT [Ref. 44]
[w] XRD [Ref. 46]
[x] Neutron and γ-ray diffraction [Ref. 47]
[y] Reflectance [Ref. 48]

1.2. Polarization Effects in (Be,Mg)ZnO/ZnO Heterostructures

II-Oxide group heterostructures containing MgZnO and CdZnO ternaries have been widely investigated for optical and electronic applications.[1,2] A very high low-temperature 2DEG mobility of $7 \times 10^5 \text{cm}^2/\text{Vs}$ has been reported for a low Mg content $Zn_{0.99}Mg_{0.01}O$/ZnO heterostructure grown on bulk ZnO, although at a low electron sheet density of 1.4×10^{11} cm^{-2}.[49] This progress allowed the observation of the fractional Hall effect in ZnO-based heterostructures.[50] However, the practical 2DEG densities at MgZnO/ZnO interfaces are found to be limited to $\leq 1 \times 10^{13}$ cm^{-2},[51] which may fall short for high power RF applications.

The spontaneous polarization arises from an intrinsic asymmetry of the bonding in the equilibrium wurtzite crystal structure (Figure 2). In an infinitely large bulk wurtzite material with no interfaces, the net spontaneous polarization will be zero. However, when an interface is introduced, it would result in the non-zero spontaneous polarization; free electrons would try to screen the field and 2DEG may be formed on the interface.
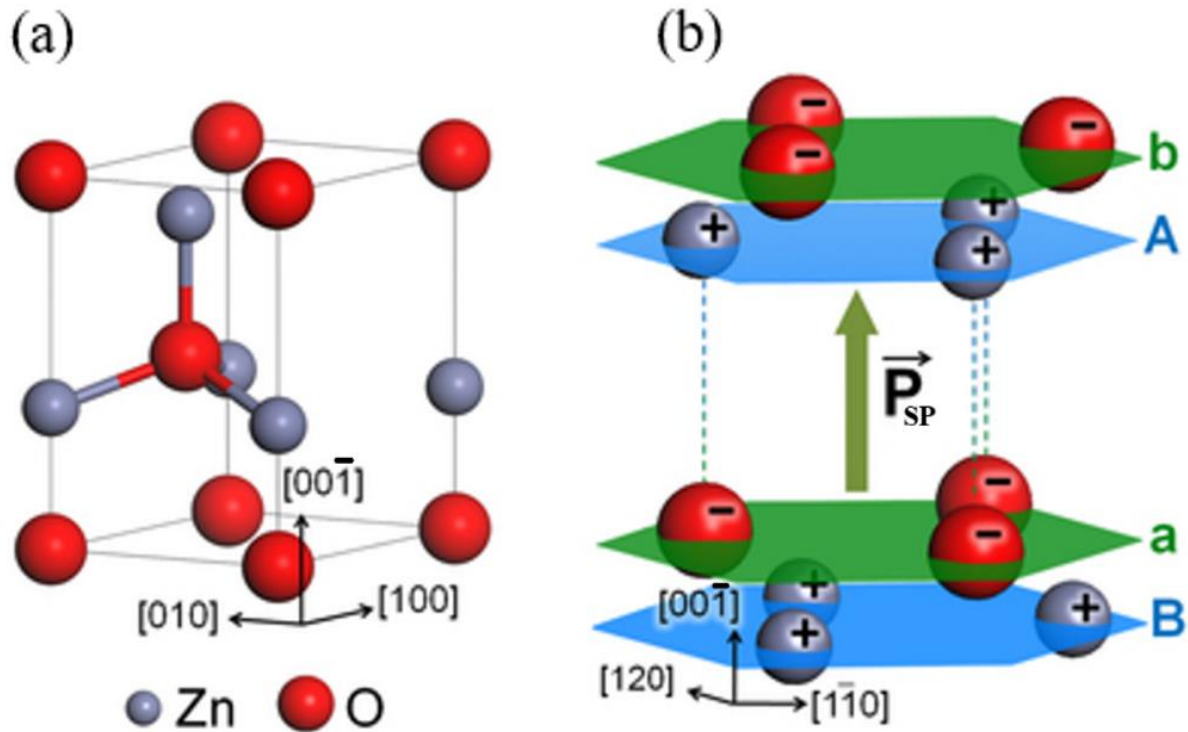
Figure 2. (a) ZnO unit cell, including the tetrahedral-coordination between Zn and its neighboring O. (b) ZnO has a noncentrosymmetric crystal structure that is made up of alternate layers of positive and negative ions, leading to spontaneous polarization P_{SP} (adopted from Ref. 52)

In addition to the spontaneous polarization, P_{SP}, in wurtzite crystals, mechanical strain also results in polarization, which is called piezoelectric polarization P_{PZ} (P_{SP} does not depend on strain). Figure 3 shows the origin of P_{PZ} in strained Zn-polar ZnO. When the [0001] direction is assumed to be the positive direction, P_{PZ} is negative for tensile and positive for compressive strained layers. Therefore, the spontaneous and piezoelectric polarizations are co-directional in case of tensile strain and anti-directional in case of compressive strain.
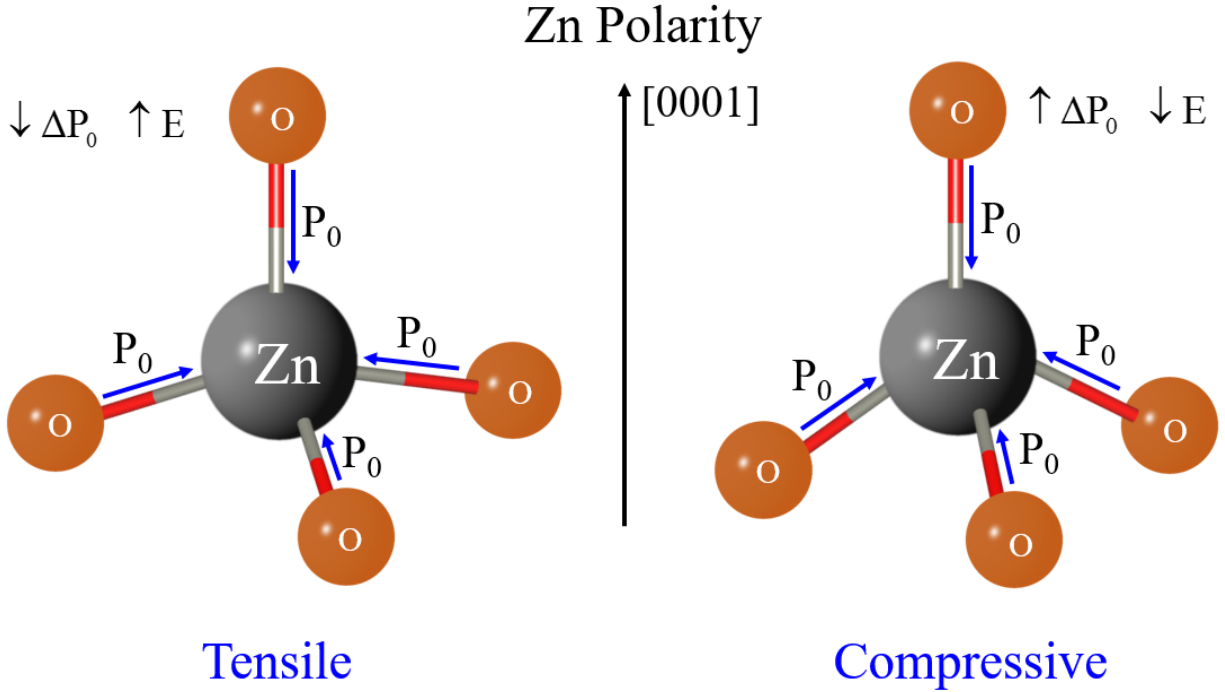
Figure 3. The ball-and-stick configuration of a ZnO tetrahedron for with a homogenoeous in-plane tensile (left) and compressive (right) strain showing a net polarization in the $[000\bar{1}]$ and $[0001]$ directions, respectively.

For the BeMgZnO system, as a first approximation it is assumed that MgO has the largest spontaneous polarization and BeO has similar P_{SP} to that of ZnO. The limiting factor for MgZnO/ZnO HFETs is the counteractive piezoelectric polarization originating from the compressive strain (Figure 4(a)). In order to overcome this limitation and achieve high 2DEG carrier density, the use of BeMgZnO barrier was proposed. The quaternary alloy allows smaller a lattice parameter than that of ZnO and thus provides tensile strain and piezoelectric polarization that supports the 2DEG on the BeMgZnO/ZnO interface (Figure 4(b)). Despite its great potential, there have been only a limited number of theoretical and experimental investigations of the quaternary BeMgZnO alloy. In this work we focus on properties of ternary BeZnO and quaternary BeMgZnO and their potential application for heterostructures with 2DEG.

8
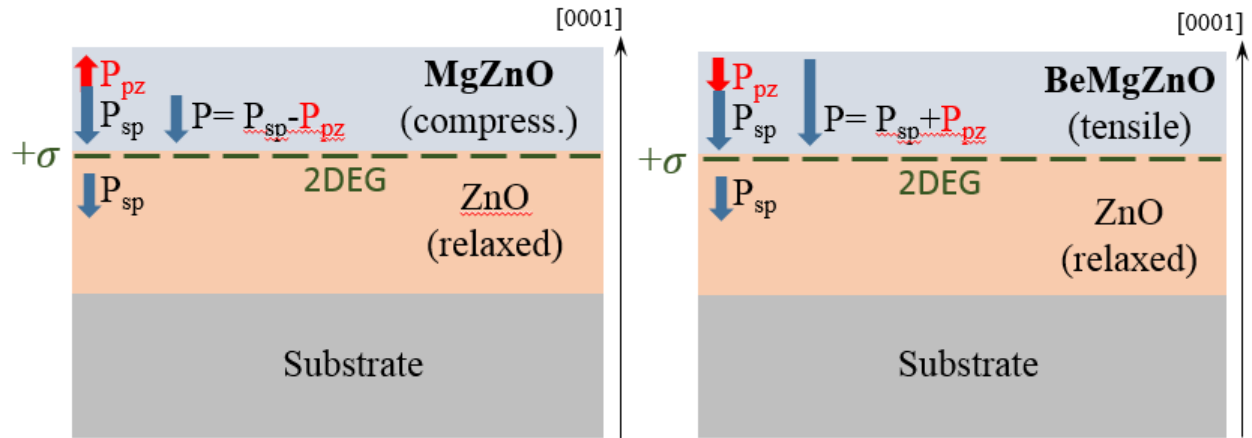
Figure 4. The schematics of Zn-polar MgyZn1-yO/ZnO and BexMgyZn1-x-yO/ZnO heterostructure.

1.3. Organization of the Thesis

This thesis focuses on P-MBE growth and comprehensive investigation of (Be,Mg)ZnO alloys and (Be,Mg)ZnO/ZnO heterostructures. Introduction is dedicated to the discussion of ZnO family of materials and origin of the polarization effects in polar materials, such as wurtzite ZnO, and detailed discussion of the strengths and limitations of (Be,Mg)ZnO/ZnO heterostructures.

In Chapter 2, the composition, bandgaps, lattice parameters, morphology and electrical conductivity of O-polar BeMgZnO quaternary alloy grown on c-sapphire are investigated using various measurement techniques. Ion beam analysis using Rutherford backscattering spectrometry with He$^+$ analyzing ion beam and non-Rutherford elastic backscattering experiments with high energy protons were used for the composition measurements; X-ray diffractometry (XRD) was used for the investigation of lattice parameters and crystal quality; transmission/absorption measurements were used for the bandgap determination; atomic force microscopy (AFM) was used for the investigation of surface morphology; and reflection high-energy electron diffractometry (RHEED) was for the investigation of the growth mode and surface morphology.

9

Chapter 3 reports on the detailed investigation of optical characteristics of BeMgZnO alloy using steady state and time-resolved photoluminescence (PL) techniques. This includes determination of the effect of Mg/Be ratio on carrier dynamics, localization, and Stokes shift in BeMgZnO thin films.

Chapter 4 discusses metal semiconductor structures and fabrication methods used for ZnO-based devices. The effects of various surface preparation on Schottky barrier height were investigated. Where, additionally, the effects of annealing conditions and carrier concentration were investigated for ohmic contacts. The necessary steps to achieve ohmic contacts with low specific contact resistivity and Schottky contacts with high Schottky barrier height and low leakage current are specified.

In Chapter 5, experimental results on O-polar MgZnO/ZnO heterostructures are discussed with the emphasis on temperature depended Hall and noise measurements. Where Section 5.2 provides theoretical investigation of (Be,Mg)ZnO/ZnO heterostructures with 2DEG. All results are summarized and overall outlook and future work is discussed in Chapter 8.

Chapter 2. Growth and Characterization of BeMgZnO Thin Films

There are many techniques as mentioned above for the growth of ternary and quaternary (Be,Mg)ZnO alloys. The structures presented in this thesis are growth using plasma assisted molecular beam epitaxy (P-MBE) which allows the formation of high-quality (low-defect, highly uniform) semiconductor thin films in a precisely controlled way.

Figure 5 shows the cross-sectional schematics of the O-polar and Zn-polar BeMgZnO samples investigated in this work. BeMgZnO thin films were grown by P-MBE with an RF oxygen plasma source and Knudsen cells for Zn, Be, and Mg and on epitaxial carbon compensated high resistivity GaN(0001)/Al_2O_3(0001) templates. Pyrolytic boron nitride (PBN) crucibles were used for Zn and Mg sources and a BeO crucible for the Be source. The GaN templates were cleaned *ex situ* with aqua Regia to remove possible metal contamination and followed by immersion in a HCl : H_2O = 1 : 1 solution to remove any gallium oxide (Ga_2O_3) from the surface. After loading the substrate to the growth chamber, GaN surface was thermally cleaned at 625 °C for 15 min. Templates were exposed to Zn flux prior to ZnO growth to terminate the GaN surface with Zn adatom and prevent the formation of Ga oxide. [53] By varying the VI/II ratio during low temperature ZnO growth, the polarity of the growth layer could be controlled.[54] First, a ~15 nm-thick low temperature ZnO buffer layer was grown at 300 °C followed by annealing at 730 °C to achieve an atomically flat surface. Then, a 120 nm thick high temperature ZnO layer was grown at 680 °C. BeMgZnO films were deposited at ~1.3 x 10^{-5} Torr oxygen pressure with thicknesses 130 nm and 100 nm for Zn-polar and O-polar films grown on GaN/sapphire temples. The average growth rate of Zn-polar samples was 170 nm/h and that of O-polar was 75 nm/h.

For the growth of O-polar layers on sapphire, a 2 nm-thick MgO buffer layer was deposited at 750 °C to ensure 2D nucleation followed by a 10-15 nm thick low temperature (300 °C) ZnO

buffer layer. Then BeMgZnO films were deposited at ~8 x 10^{-6} Torr oxygen pressure using 400 W RF plasma power and 400 °C substrate temperature, which as a set of conditions was found to be optimal for the best crystal quality.[55] The average growth rate of the quaternary material was ~100 nm/h, and the film thicknesses were ~170 nm.

BeMgZnO (0001)	130 nm
HT ZnO (0001)	120 nm
Buffer ZnO (0001)	15 nm
High resistivity GaN (0001)	2.5 μm
Buffer AlN (0001)	350 nm
Sapphire (0001)	

(a)

BeMgZnO (000$\bar{1}$)	100 nm
HT ZnO (000$\bar{1}$)	120 nm
Buffer ZnO (000$\bar{1}$)	15 nm
High resistivity GaN (0001)	2.5 μm
Buffer AlN (0001)	350 nm
Sapphire (0001)	

(b)

BeMgZnO (000$\bar{1}$)	170 nm
Buffer ZnO (000$\bar{1}$)	15 nm
MgO	2 nm
Sapphire (0001)	

(c)

Figure 5. The cross-sectional schematics of (a) Zn-polar and (b) O-polar BeMgZnO on GaN/sapphire and c) O-polar BeMgZnO on sapphire templates.

2.1. Composition Measurements

The composition of Be and Mg directly influence the properties of the quaternary BeMgZnO alloy. Quantitative measurements of chemical profiles of light elements, such as C or Be, in matrices composed of heavy atoms are challenging for nondestructive methods. Analytical techniques like SIMS or XPS, which leads to sputtering and sample damage effects, require sample standards, and suffers from difficulties in the detection of the light Be element, we apply ion beam analysis as nondestructive characterization tool. To determine Be content and its depth distribution in ternary BeZnO and quaternary BeMgZnO, we employed ion beam analysis (IBA), which is a powerful and nondestructive characterization tool. IBA allows accurate measurements of concentrations of constituents and the stoichiometry of thin films as a function of depth. Although

12

conventional Rutherford Backscattering Spectrometry (RBS), the simplest IBA method, can provide an absolute accuracy of 1%, the detection of light elements in the presence of heavier ones is challenging. To overcome this limitation, we employed resonances which appear in the elastic backscattering cross section at characteristic energies of the analyzing He^+ or H^+ ions, which make feasible a quantitative chemical IBA of light elements in binary, ternary, or quaternary compounds. The atomic composition with less than 1-2 atom % uncertainty was measured in ternary BeZnO and quaternary BeMgZnO alloys using a combination of nondestructive Rutherford backscattering spectrometry with 1 MeV He^+ analyzing ion beam and non-Rutherford elastic backscattering experiments with 2.53 MeV energy protons (Figure 6). An enhancement factor of 60 in the cross-section of Be for protons has been achieved to monitor Be atomic concentrations. The applied ion beam technique applied in our work supported with the detailed simulation of ion stopping, backscattering, and detection processes allows for quantitative depth profiling and compositional analysis of wurtzite BeZnO/ZnO/sapphire and BeMgZnO/ZnO/sapphire layer structures with low uncertainty for both Be and Mg. In addition, the IBA data were correlated with excitonic bandgaps of the layers deduced from optical transmittance measurements. To augment the measured compositions and bandgaps of BeO and MgO co-alloyed ZnO layers, hybrid density functional bandgap calculations were performed by varying the Be and Mg contents. The theoretical vs. experimental bandgaps show linear correlation in the entire bandgap range studied from 3.26 eV to 4.62 eV. The analytical method employed should help facilitate bandgap engineering for potential applications, such as 2DEG electron channels, solar blind UV photodetectors, and heterostructures for UV emitters and intersubband devices.
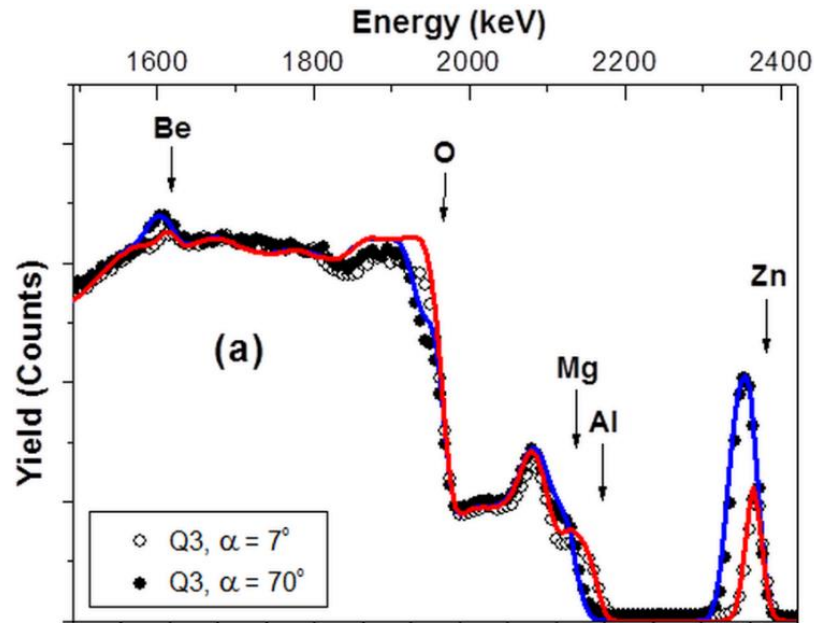
Figure 6. 2.53 MeV non-Rutherford proton elastic backscattering spectra of (a) $Be_{0.11}Mg_{0.33}Zn_{0.56}O$ (Q3) layers measured at sample tilt angles of $\alpha = 7^{\circ}$ and $\alpha = 70^{\circ}$. Surface peaks for Be, Mg, and Zn, and spectrum edges for O and buried Al (in sapphire), as well as the depth scale for Zn are indicated. The symbols represent measured data. Simulated spectra are also shown by red and blue lines.

2.2. Lattice Parameters and Bandgaps

The c- and a-lattice parameters were deduced from X-Ray Diffraction (XRD) measurements for the symmetric (0002) and skew-symmetric (10-13) reflections, respectively, using the line focus mode. The optical absorption measurements to determine the optical bandgaps were performed using a Deuterium lamp and a SPEX 500M scanning spectrometer equipped with a photomultiplier tube. Figure 7 shows symmetric XRD 2theta-Omega scans for the (0002) reflections for selected O-polar BeMgZnO samples. With increased Be and Mg content the crystal quality slightly degrades, as evident from lower intensity of XRD peaks.

14
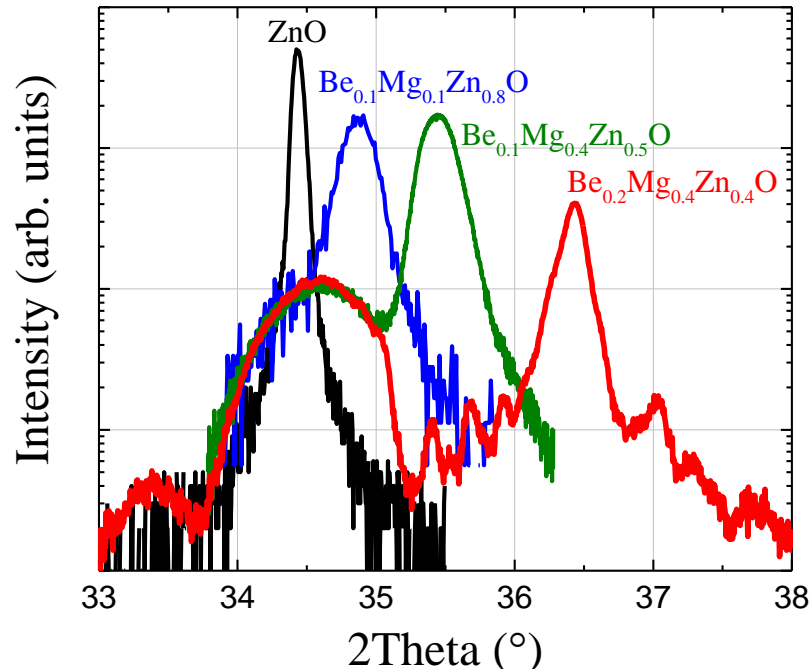
Figure 7. Symmetric XRD 2theta-Omega scans for the (0002) reflection of selected BeMgZnO.

The optical bandgap energy (E_g) was estimated from the ($\alpha_{opt}hv$)^2 vs. hv Tauc plots (Figure 8) where α_{opt}, the absorption coefficient which was deduced from the transmission measurements and the measured thickness values and found to be in the order of is 2×10^5 cm^{-1} above the absorption edge. Widening of the bandgap with increasing Be and Mg content is clearly observed in Figure 8.
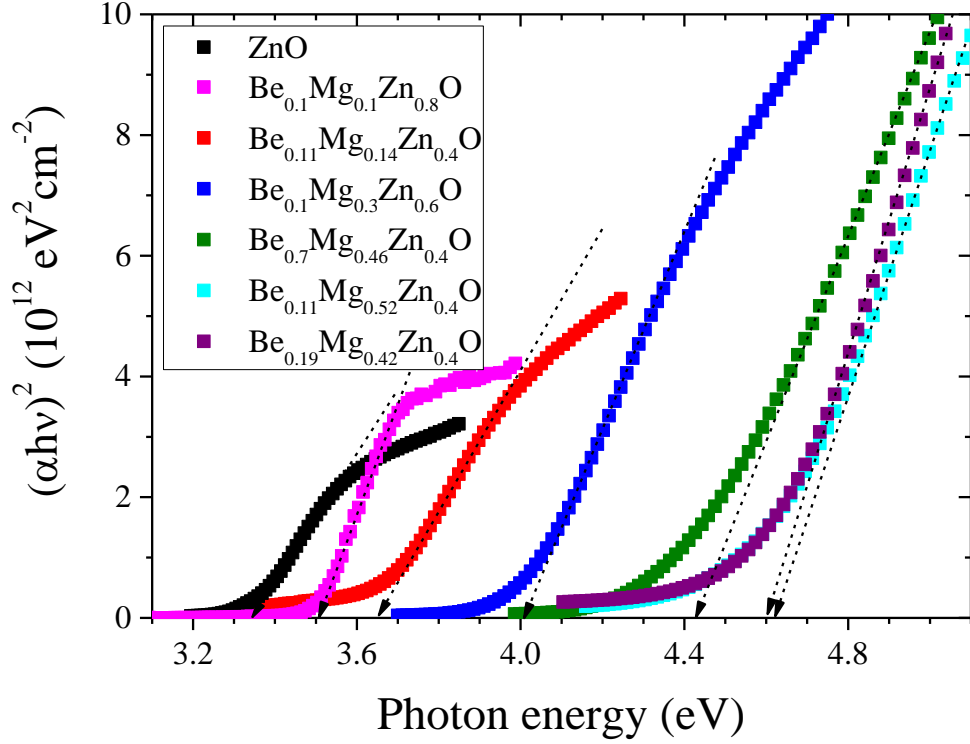
Figure 8. Tauc plots for the determination of absorption edges using transmittance measurements for selected BeMgZnO samples. The absorption coefficient is in the order of 2×10^5 cm^{-1} above the bandgap.

We used first principles calculations to analyze structure, and electronic properties of quaternary BeMgZnO alloys. The structural properties were calculated using Perdew-Burke-Ernzerhof (PBE)[16] parameterization of the generalized gradient approximation (GGA)[17] to the density functional theory (DFT). Although in most cases PBE approximation is known to slightly overestimate the lattice constants, it was found to be adequate in this study as marginal improvements were obtained using a more accurate Heyd-Scuseria-Ernzerhof (HSE06) hybrid functional,[18] which comes with a significantly increased computational cost.

The electronic bandgaps computed by PBE, on the other hand, are significantly underestimated for the ZnO family of binaries: the PBE gaps obtained here are 4.99 eV for rock-

salt MgO, 0.74 eV for ZnO, and 7.87 eV for BeO, showing mean error of 2.72 eV in comparison with the experimental values discussed below. Therefore, analysis of quaternary oxides using (semi)local approximations to the DFT is problematic. In contrast, standard HSE06 hybrid functional yields a drastically lower mean absolute error for the semiconductor bandgaps of only 0.26 eV.[19] Furthermore, in HSE06, the exchange-correlation energy contains exact Fock-type exchange part that is mixed with the (semi)local part in a ratio (standard fraction of exact exchange is 0.25) that can be adjusted to fit the experimental bandgap of a specific material. The fraction of exact exchange (0.375) adjusted to yield the experimental low temperature bandgap of 3.43 eV for ZnO,[20] yields the bandgap of 10.2 eV for BeO, which is close to the experimental value of 10.6 eV,[21] and 7.72 eV for the stable rock-salt phase of MgO, close to the measured bandgap of 7.7 eV.[22] Based on the good agreement of calculated bulk binary bandgaps with experiment a common value of 0.375 was adopted in this work for the exact exchange[23] fraction with the expectation that reasonable bandgaps will be obtained at intermediate concentrations of Mg and Be in BeMgZnO.

All calculations were performed using supercells with 72 atoms and using Γ–point eigenvalues only, and projector augmented wave (PAW) pseudopotentials. Wurtzite lattice was used throughout the work for all alloy compositions, which leads to an additional error at high concentrations of Mg, where rock-salt crystal structure would prevail. However, in quaternary BeMgZnO alloys, the rock salt phase becomes energetically favorable for fractions of Mg exceeding 75% for alloy containing 3% of Be, and 83% for alloy with 17% of Be.[13] These high concentrations of Mg are not accessible in experiment, and therefore, present purely theoretical interest at the moment. Therefore, for all data related to experimentally grown BeMgZnO alloy, and even at higher Mg and Be concentrations, the wurtzite structure is appropriate. All atomic structures were relaxed within PBE with respect to the lattice parameters a and c, c/a ratio, as well

as all internal degrees of freedom, to yield forces of 0.01 eV/Å or less. The plane wave basis sets with 500 eV energy cutoff were used in PBE calculations. This allowed accurate calculations of the BeMgZnO crystal structure. The electronic properties were computed for relaxed crystal structures using HSE06 hybrid functional with 0.375 fraction of exact exchange and 400 eV energy cutoff. The exchange range separation parameter in HSE06 was kept at 0.2 Å^{-1}.

Figure 9(a) displays the in-plane lattice parameters for $Be_xMg_yZn_{1-x-y}O$ solid solution calculated using PBE approximation to DFT for the full range of compositions. The directly computed data (solid spheres for select compositions) exhibit bowing and can be represented by the polynomial form[56]

$$a_{BeMgZnO}(x,y) = xa_{BeO} + ya_{MgO} + (1-x-y)a_{ZnO} - b_{BeZnO}x(1-x) - b_{MgZnO}y(1-y) - b_{xy}xy \quad (1)$$

where b_{BeZnO}, b_{MgZnO}, and $b_{xy} = b_{BeZnO} - b_{MgZnO} - b_{BeMgO}$ are the bowing parameters that are independent of the composition.[57] The surface plot in Figure 9(a) is the fit using Equation (1). As will be discussed below, computed c lattice parameters and the bandgaps can also be represented by Equation (1) with a replaced by the corresponding parameter. Additionally, since our calculations cover the entire range of compositions, this interpolation formula for quaternary $Be_xMg_yZn_{1-x-y}O$ also yields the bowing parameters for ternary compounds that can be used to explain the properties of the corresponding ternary alloys. Note that there are different methods used across the literature with varying bowing equations, different definitions of bowing parameters, and their dependence on the composition of the quaternary alloy making it often difficult to compare the bowing parameters reported.

Table 2. Bowing parameters for the quaternary BeMgZnO alloy calculated in this work and reported in literature.

		a (Å)	c (Å)	Bandgap (eV)
b_{BeZnO}	This work	- 0.043 ± 0.0209	- 0.043 ± 0.042	6.94 ± 0.428
		Linear[a]	Linear[a]	5.6[a]
		-	-	4.5 [b]
b_{MgZnO}	This work	0.061 ± 0.0209	- 0.172 ± 0.0421	0.237 ± 0.438
		0.04167[c]	- 0.1333[c]	-
b_{xy}	This work	- 0.140 ± 0.0384	0.427 ± 0.0773	- 2.79 ± 0.800

[a] GGA(PBE) to DFT [Ref. 42]
[b] Absorption measurements on RF magnetron sputtered BeZnO [Ref. 58]
[c] GGA(PAW) to DFT [Ref. 35]

The bowing parameters obtained from the fits using Equation (1) are provided in Table 2. For convenience, Figure 9(b) displays the dependence of a lattice parameter on Mg content for various fixed Be contents in BeMgZnO alloys. As also shown in Table 1, the a parameter of wurtzite MgO is very close to that of ZnO due to relatively small difference in covalent radii (1.22 Å for Zn, 1.41 Å for Mg).[11] On the other hand, due to the smaller covalent radius of Be (0.96 Å)[11] compared to Zn, the in-plane lattice parameter of BeO is substantially smaller than that of ZnO. The bowing of the surface in Figure 9(a) is relatively small despite the wide range of the lattice parameter variation in BeMgZnO. By choosing proper Be and Mg content it is possible to achieve in-plane lattice parameter larger (by a small amount) or smaller than that of ZnO. The latter one is very important in achieving tensile strain in the barrier layer of Zn-polar BeMgZnO/ZnO heterostructure, which yields to the proper sign of piezoelectric polarization and results in high two-dimensional electron gas (2DEG) density near the interface. For Zn-polar $Be_xMg_{0.2}Zn_{0.8-x}O$/ZnO heterostructures even 5% of Be should provide sufficient piezoelectric polarization to generate 2DEG sheet density above 10^{13} cm^{-2}. The tensile strain required in the barrier layer for 2DEG generation cannot be achieved with Zn-polar MgZnO/ZnO heterostructure.
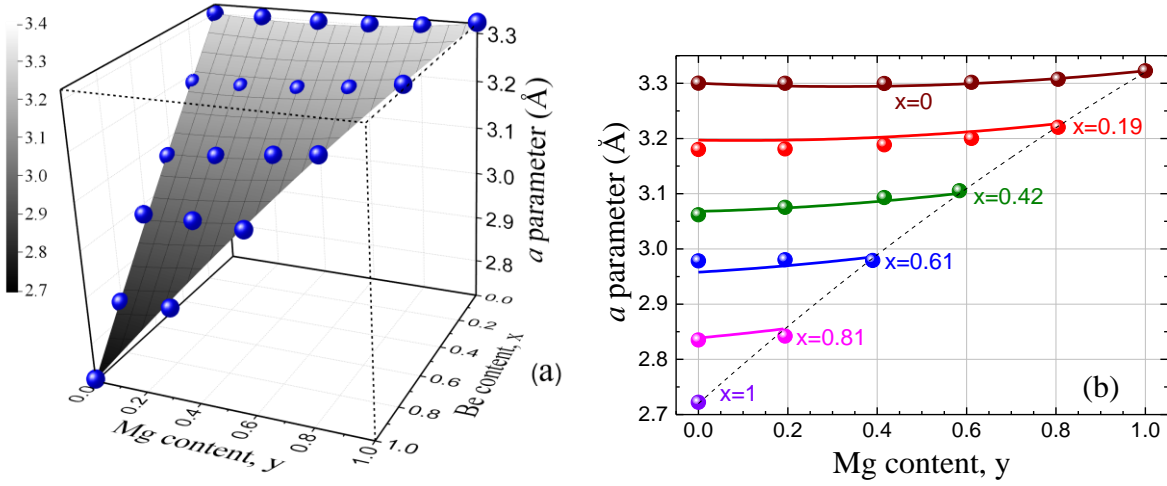
Figure 9. (a) Calculated a lattice parameters of $Be_xMg_yZn_{1-x-y}O$ as a function of Be and Mg content. Solid circles represent calculated values using PBE-DFT, and the surface is a fit using equation (1), which provided the bowing parameters listed in Table 2. (b) Computed a lattice parameter values as a function of Mg content for different Be compositions. The solid lines are the corresponding sections from the surface fit in (a). The dashed line corresponds to $Be_{1-y}Mg_yO$ ternary alloy.

Figure 10 shows the calculated out-of-plane c lattice parameters of BeMgZnO (solid spheres) and the fit (surface) obtained using equation (1). Bowing of the c lattice parameter is observed to be significantly larger than that of the a parameter due to the fact that the incorporations of Mg and Be have opposite effects on the in-plane lattice parameter (reducing with Be, increasing with Mg), while the out-of-plane lattice parameter of BeMgZnO reduces with increasing both Be and Mg content.

20
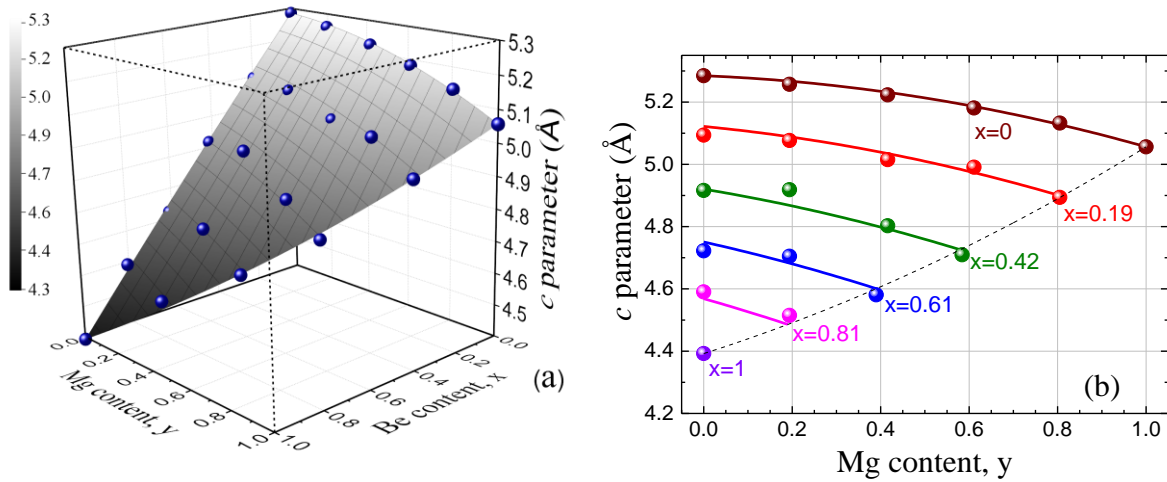
Figure 10. (a) Calculated c lattice parameters of BexMgyZn1-x-yO as a function of Be and Mg contents. Solid circles represent calculated values using PBE-DFT, and the surface is a fit using equation (1) which provided the bowing parameters listed in Table 2. (b) Computed c lattice parameter values as a function of Mg content for different Be compositions. The solid lines are the corresponding sections from the surface fit in (a). The dashed line corresponds to $Be_{1-y}Mg_yO$ ternary alloy.

Figure 11 (a) presents the theoretically calculated bandgap values using tuned HSE06 hybrid functional with the fraction of exact exchange 0.375 (solid spheres) and the fit using equation (1) (the surface fit) for the entire range of BeMgZnO compositions. Figure 11 (b) shows the computed bandgaps as a function of Mg content for different Be contents. The bandgap bowing for ternary MgZnO compound is relatively small, while that for BeZnO is clearly noticeable in Figure 11 (a).
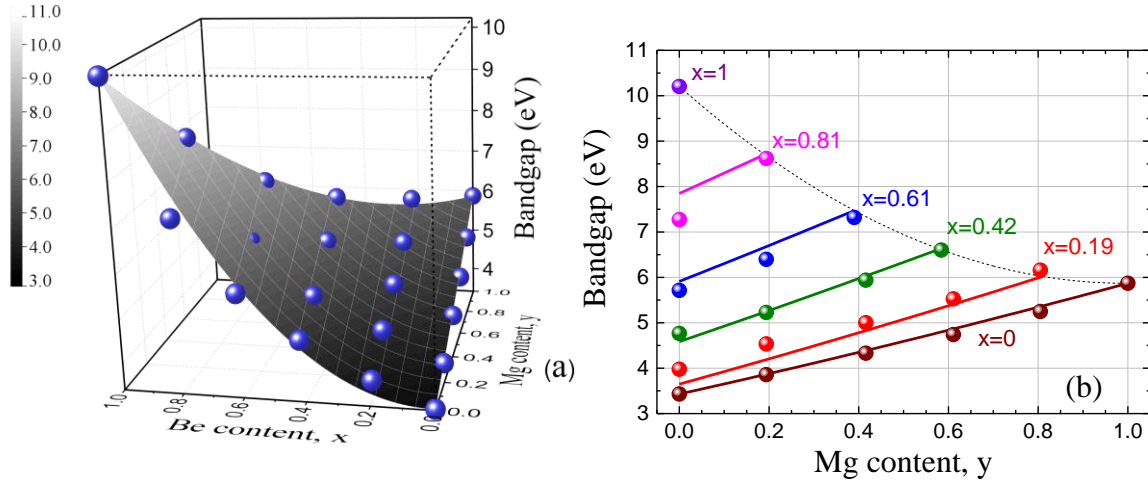
Figure 11. (a) Calculated bandgaps of $Be_xMg_yZn_{1-x-y}O$ as a function of Be and Mg contents. Solid circles represent calculated values using the exchange tuned HSE06 hybrid functional, and the surface is a fit using equation (1), which provided the bowing parameters listed in Table 2. (b) Computed bandgaps as a function of Mg content for different Be compositions. The solid lines are the corresponding sections from the surface fit in (a). The dashed line corresponds to $Be_{1-y}Mg_yO$ ternary alloy.

The theoretical methods used here were validated by comparing the calculated lattice parameters and bandgaps with those measured for MBE-grown quaternary layers. Figure 12 (a) and Figure 12 (b) compare the calculated a and c lattice parameters, respectively, of BeMgZnO quaternary solid solutions with experimental values. It is worth noting that incorporation of Be, which has small covalent radius on the Zn lattice sites, partially compensates the lattice expansion caused by Mg and permits attainment of BeMgZnO layers containing up to approximately 50% Mg.[12] As GGA to DFT in most cases is known to overestimate the lattice parameters by 1-2%, as expected, the calculated values are larger than the measured ones by about 0.04 Å and 0.08 Å for a and c parameters, respectively. This discrepancy also partially originates from slight variations in the actual Be and Mg atomic contents from the plotted 9% and 39%, respectively, as well as the error in measurement of the lattice parameters (see Table 3) and the compositions.[59]

Table 3. The lattice parameters and bandgaps of MBE grown quaternary BeMgZnO layers with corresponding measurement errors. The compositional values are within ±1-2 atomic % of Be for all samples and within ±1 atomic % of Mg for Set I (near 9% Be content, varying Mg content) and within ±4 atomic % of Mg for Set II (near 39% Mg content, varying Be content).

Sample	a parameter, Å	c parameter, Å	Bandgap, eV
Set I: Be content near ~9%			
$Be_{0.08}Zn_{0.92}O$	3.236 ± 0.020	5.123 ± 0.001	3.34 ± 0.05
$Be_{0.11}Mg_{0.14}Zn_{0.75}O$	3.208 ± 0.007	5.099 ± 0.001	3.64 ± 0.05
$Be_{0.07}Mg_{0.33}Zn_{0.60}O$	3.220 ± 0.010	5.049 ± 0.001	4.06 ± 0.05
$Be_{0.07}Mg_{0.46}Zn_{0.47}O$	3.229 ± 0.006	5.026 ± 0.001	4.44 ± 0.05
$Be_{0.12}Mg_{0.52}Zn_{0.36}O$	3.210 ± 0.006	4.979 ± 0.001	4.58 ± 0.05
Set II: Mg content near ~39%			
$Mg_{0.39}Zn_{0.61}O$	3.269 ± 0.010	5.193 ± 0.001	3.60 ± 0.05
$Be_{0.05}Mg_{0.37}Zn_{0.58}O$	3.250 ± 0.006	5.104 ± 0.001	3.75 ± 0.05
$Be_{0.07}Mg_{0.37}Zn_{0.56}O^{*}$	3.245 ± 0.006	5.079 ± 0.001	3.95 ± 0.05
$Be_{0.08}Mg_{0.39}Zn_{0.53}O^{*}$	3.232 ± 0.006	5.044 ± 0.001	4.19 ± 0.05
$Be_{0.19}Mg_{0.42}Zn_{0.39}O$	3.160 ± 0.006	4.939 ± 0.001	4.62 ± 0.10

[*] considered also as part of the set of samples with near 9% Be content.

The error bars shown in Figure 12 represent the corresponding overall confidence limits. The measurement error results partially from alloy XRD peak broadening and use of the relatively weak and broad low-temperature ZnO XRD peak as the reference position for asymmetric XRD scans. It is observed in Figure 12(a) that $Be_{0.09}Mg_yZn_{0.91-y}O$ samples (blue circles) exhibit larger scatter in the measured in-plane lattice parameter around the expected trend compared to the $Be_xMg_{0.4}Zn_{0.6-y}O$ samples (red stars). The main source of error in this case is the deviation of the actual Be content from the plotted 9% as a small change in the Be molar content results in a significant change in the in-plane lattice parameter. Nevertheless, despite the rigid shift due to slight overestimation of the predicted lattice parameters, the theoretical model satisfactorily predicts the lattice parameters of the quaternary alloy.

23
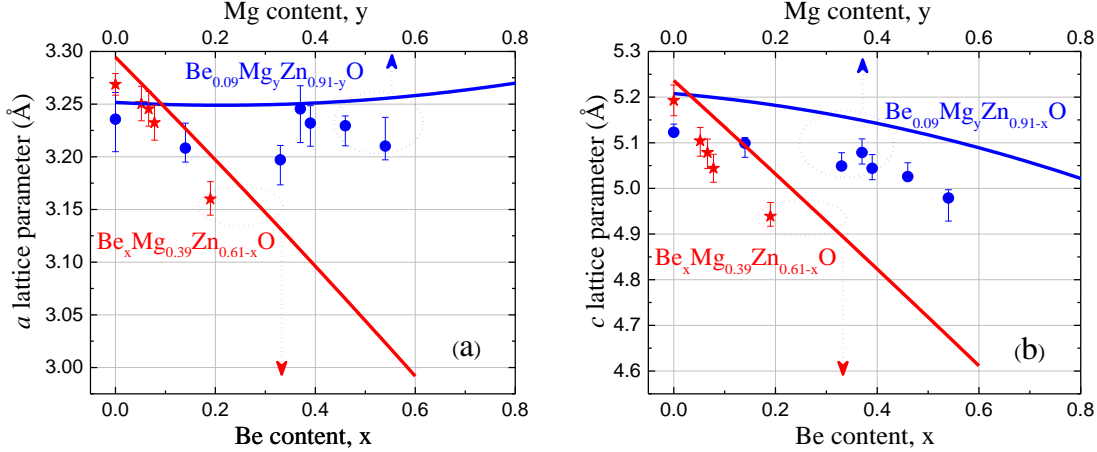
Figure 12. (a) In-plane and (b) out-of-plane lattice parameters of $Be_xMg_{0.39}Zn_{0.61-x}O$ (red curve for theory and red stars for experiment) and $Be_{0.09}Mg_yZn_{0.91-y}O$ (blue curve for theory and blue circles for experiment) as functions of Be and Mg content, respectively. The error bars indicate the confidence limits originating from slight variations in the actual Be and Mg atomic contents from the plotted 9% and 39%, respectively, as well as the error in measurement of the lattice parameters (see Table 3) and the compositions.

Figure 13 compares the calculated and measured bandgaps for $Be_{0.09}Mg_yZn_{0.91-y}O$ solid solutions. The difference between theoretically predicted electronic bandgaps and experimentally determined optical bandgaps is 0.14-0.32 eV for Set I (samples with near 9% Be but varying Mg content) and higher for Set II (samples with near 39% Mg but varying Be content). The large deviation for Set II when Be content is 8% or lower may be attributed to possible segregation of the Mg-rich phase, which is characteristic to high Mg content MgZnO. Phase segregation would also take place in the quaternary alloy with Be concentration insufficient to compensate the tensile strain caused by large Mg content.[17] As a result, effectively lower Mg content remains in the wurtzite lattice, which would be revealed as lower optical bandgap. It should be noted that XRD measurements are not sensitive enough to reveal any secondary phase. Moreover, as the effect of Mg incorporation on the lattice parameters is smaller than that of Be, the effect of phase segregation may not be noticeable, particularly also due to broad XRD peaks.[12]

The discrepancy between calculated and measured bandgaps shown in Figure 13 is also associated with neglecting temperature expansion of the lattice, temperature dependence of electron-phonon coupling, and excitonic effects in *ab initio* calculations. The hybrid functional method of calculations was tuned to yield the bandgap that matches the measured low-temperature ZnO bandgap of 3.43 eV (obtained from the 3.37 eV low temperature emission of A-exciton plus the exciton binding energy E_B^X of 60 meV), higher than the excitonic bandgap measured at room temperature (3.26eV). Similarly, for MgO and BeO, increasing temperature from 77K to 300K results in bandgap shrinkage of about 0.2 eV [40] and 0.1 eV,[48] respectively. Thus, the combined effects of lattice expansion and temperature dependence of electron-phonon coupling on the bandgap of BeMgZnO alloy can account for variations in the range of 0.1 eV to 0.2 eV. The decrease in bandgap due to the excitonic effect only is 80meV in rocksalt MgO,[40] and the reported excitonic binding energy of wurtzite MgZnO does not vary from that of ZnO by more than 10meV for Mg content up to 29%.[60,61] The excitonic binding energy measured for BeO, on the other hand, is significantly higher (0.17eV). Therefore, for ternary BeZnO and quaternary BeMgZnO alloys, the exciton binding energy is expected to fall within the range determined by ZnO and BeO exciton binding energies, *i.e.* 0.06–0.17 eV. These estimates suggest that the systematic difference between the calculated and measured bandgaps in BeMgZnO alloys is mainly due to excitonic effects and temperature dependent renormalization of the bandgap, unaccounted for in the theoretical method. When all these effects are considered, the satisfactory prediction of $Be_{0.09}Mg_yZn_{0.91-y}O$ bandgap by the theory suggests that the use of the HSE hybrid functional in our calculations yields the correct bandgaps for both constituent binaries and their solid solutions. Thus, the bowing parameters provided in Table 2 are expected to be well representative. It should be noted, however, that although the solubility limits in the BeO-MgO-ZnO system have not yet been explored in

detail, growing single-phase material with large Mg and Be content while maintaining the material quality may be extremely challenging or even impossible because of strong tendency for phase segregation observed for MgZnO and BeZnO ternaries.
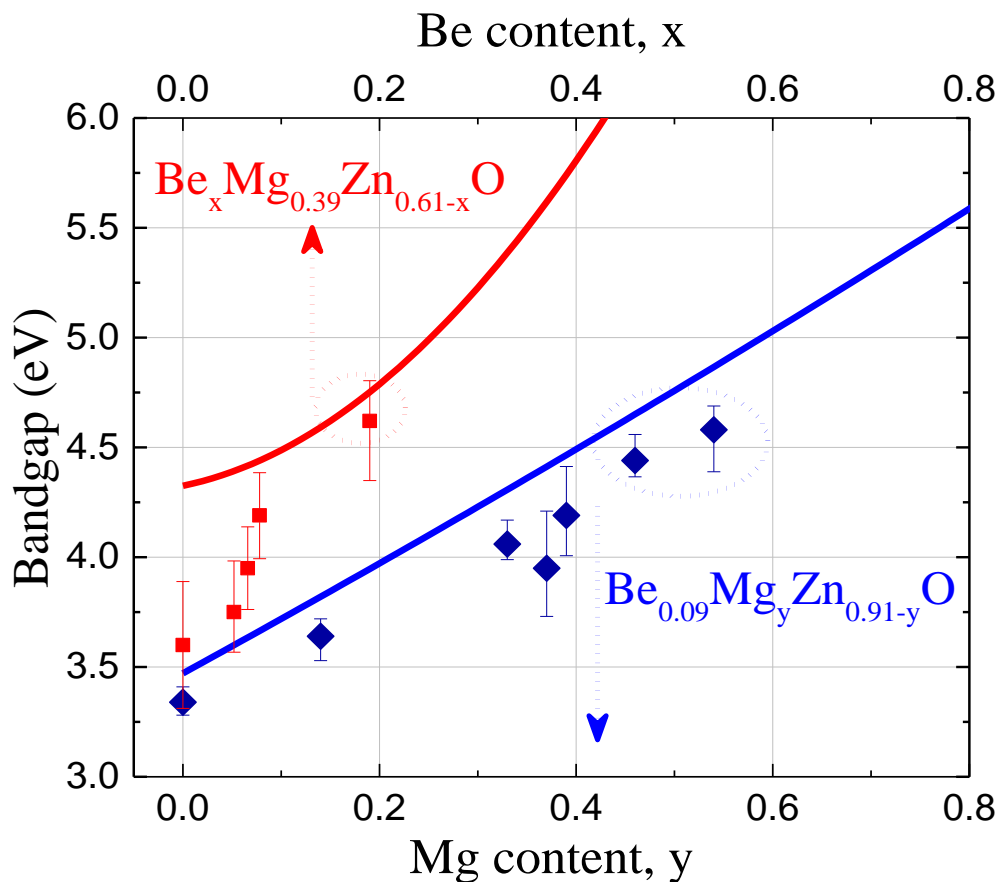
Figure 13. Bandgaps of $Be_{0.09}Mg_yZn_{0.91-y}O$ and $Be_xMg_{0.39}Zn_{0.61-x}O$ solid solutions calculated using tuned HSE06 (solid lines) compared to experiment (symbols). The large deviation between experimental and theoretical values for $Be_xMg_{0.39}Zn_{0.61-x}O$ for Be content below 10% is attributed to possible segregation of Mg-rich phase. On the other hand, for samples with relatively high Be content, Be can suppress phase segregation of Mg-rich phase and thus increase incorporation of Mg to the wurtzite lattice of BeMgZnO alloy due to compensation of the tensile strain resulting from large Mg content. The compositions of all $Be_xMg_{0.39}Zn_{0.61-x}O$ samples are estimated based on flux measurements and thus show accumulative amount of Be and Mg in the quaternary layers.

Table 2 compares the bowing parameters computed here for the quaternary BeMgZnO system, with those of the ternary alloy subsystems, BeZnO and MgZnO, from literature. We obtain negative and relatively small values for BeZnO bowing of -0.043 Å for both a and c lattice parameters. The in-plane lattice bowing parameter for MgZnO is 0.061 Å and out-of-plane lattice bowing is negative but larger in the absolute value, -0.172 Å. Among the ternaries involved, MgZnO have been explored extensively both experimentally and theoretically, whereas BeZnO has received limited attention, and BeMgO almost no consideration at all due to difficulty of growth. Shimada et al.[35] calculated structural properties of MgZnO alloy using GGA to DFT with projector augmented wave (PAW) pseudopotentials and reported lattice bowing parameters similar to ours. The observed nonlinearity of the lattice parameters was attributed to difference in the chemical bonding between rocksalt MgO and wurtzite ZnO. In regard to the effect of Be incorporation, the calculations predict relatively small bowing parameters for the compositional dependences of the lattice parameters in BeZnO, as shown in Table 2. Using GGA, X. Su et al.[62] performed DFT calculations of lattice parameters of wurtzite BeMgZnO for selected compositions; however, no bowing was reported. The bowing parameters b_{a_BeZnO} and b_{c_BeZnO} determined here are relatively small and have not been reported to date; in part due to the complications associated with precise determination of the Be content,[63] with the measurement error being higher than the effect of bowing itself. In addition, experimental studies of BeZnO for a wide range of compositions is challenging because of phase segregation observed for the solid solutions with both low (more than ~10% Be) and high Be (less than ~75% Be) content.[9]

In regard to bandgap bowing, we obtain relatively large BeZnO bowing of 6.94 eV and relatively small MgZnO bowing of 0.237 eV, which shows that the bowing parameters increase with the size difference of the constituents. Shi and Duan[56] calculated bandgaps of zinc blende

BeMgZnO using local density approximation (LDA) to DFT and reported large and composition dependent bandgap bowing parameters. However, the composition dependence does not allow comparison with the results presented here. Ding *et al.*[42] reported theoretical investigation of the bandgap of ternary BeZnO with a bowing parameter of 5.6 eV. The bandgap bowing parameter b_{Eg_BeZnO} has also been reported experimentally (4.5 eV in Ref. [58]) but is lower than the theoretically predicted value most likely due to low range of available Be compositions and low crystal quality. It should also be noted that, in our case, the calculated bowing parameters are independent of composition, indicating that the symmetry of the wave functions do not change significantly due to incorporation of Mg and Be to the lattice of ZnO to form the quaternary BeMgZnO alloy.
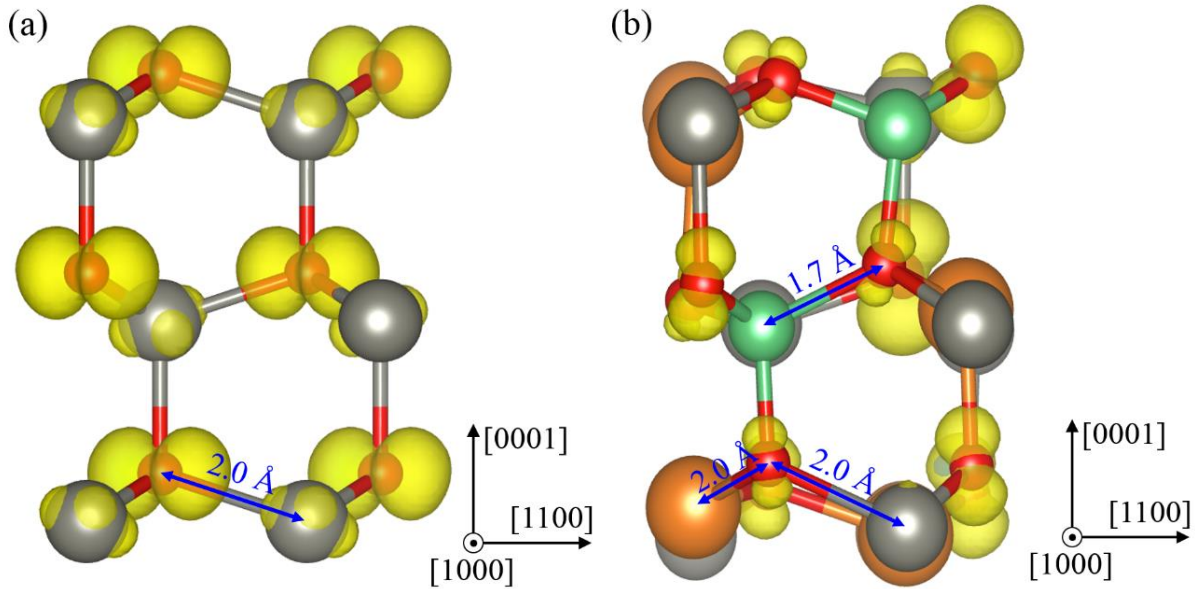
Figure 14. HSE06 calculated band-decomposed charge densities for valence band maximum (VBM) for (a) bulk ZnO and (b) $Be_{0.19}Mg_{0.42}Zn_{0.39}O$. The isosurfaces (yellow) are set at 6% of the maximum value. In each case a small fragment of the super cell is shown for clarity, with vertical direction corresponding to wurtzite (0001) axis. Zn, Mg, Be, and O atoms are represented by large gray, large orange, medium green, and small red spheres.

In order to understand the evolution of the lattice and the bandgap of the BeMgZnO alloys with the increasing Be and Mg contents, Figure 14 shows the crystal structures along with the isosurfaces of the electron density corresponding to the valence band maxima (VBM) for bulk ZnO [Figure 14(a)] and BeMgZnO alloy with 19% of Be and 42% of Mg [Figure 14(b)]. Significant structural distortions due to lattice relaxation are observed in the BeMgZnO alloy. Bond lengths between Mg and O atoms and Zn and O atoms are similar and on average about ~2 Å, while Be-O bonds are significantly shorter, on average ~1.7 Å. Due to a large BeO formation enthalpy ($\Delta_f H^0$=-6.316 eV),[64] Be-O bonding is significantly stronger than that of Zn-O ($\Delta_f H^0$=-3.632 eV),[64] which is another reason for the decrease in the lattice constant when admixing Be to ZnO. At the same time, MgO has formation enthalpy ($\Delta_f H^0$=-6.235 eV)[64] similar to BeO; however, larger atom size leads to Mg-O bond length being similar to that of ZnO.

As shown in Figure 14 electron densities are localized on oxygen atoms away from the formal bond centers. This shift is quite pronounced in HSE06 due to partial correction of the self-interaction error for the oxygen 2p-derived states, which make up most of the upper part of the valence band in both ZnO and BeMgZnO. Electron densities show stronger localization in BeMgZnO alloy compared to bulk ZnO. Particularly the VBM orbitals localized on oxygen coordinated by Mg atoms tend to be more localized, compared to those coordinated by zinc [Figure 14(b)]. These changes in the wavefunction with increasing concentration of Mg and Be are related to the bandgap bowing discussed above. Larger bowing is usually accompanied by a stronger wavefunction localization. For example, in Al$_x$Ga$_{1-x}$N alloys the similarity between Ga and Al atoms leads to small bowing and weak wavefunction localization.[65] On the other hand in In$_x$Ga$_{1-x}$N, the stronger wavefunction localization also leads to larger bandgap bowing.[66] In the case of BeMgZnO alloys, the wavefunction localization as a result of alloying is significant, which

explains the observed bandgap bowing. At the same time, the compensating effect of substituting Be and Mg on Zn sites leads to relatively small average changes in metal-oxygen bond lengths, leading to small bowing in lattice parameters.

In order to quantify the overall wavefunction localization in BeMgZnO, we calculate participation ratio (PR) for conduction band minima (CBM) and VBM wavefunctions $V \int |\psi(\mathbf{r})|^4 \, d\mathbf{r}$.[65] The PR is equal to 1 for a constant function, and has larger value for any spatially varying function, with larger values for stronger localization. Compared to GGA the wavefunctions computed with HSE06 are usually more localized, resulting in larger bandgap bowing. Table 4 presents computed PR values normalized to the most delocalized state in our calculations, which is bulk ZnO CBM state. In all alloy configurations both CBM and VBM wavefunctions are more localized, compared to bulk ZnO. Admixing Be atoms into the alloy shows stronger localization effect, where 19% of Be produces similar wavefunction PR values as 42% of Mg atoms in the alloy. Since the PRs for VBM increase by a factor of 1.5 from ZnO to $Be_{0.19}Mg_{0.42}Zn_{0.39}O$ alloy, indicating significant changes in the band edge wavefunctions, the calculated values of bandgap bowing are significant as well. Enhanced localization also usually indicates stronger interatomic bonding, which also leads to increased bandgap bowing.

Table 4. Participation ratios for the CBM and VBM wavefunctions in bulk ZnO and $Be_xMg_yZn_{1-y}O$ alloys, normalized to the bulk ZnO CBM. Larger values correspond to stronger localization of the wavefunction.

	CBM	VBM
Bulk ZnO	1.0	5.92
$Mg_{0.42}Zn_{0.58}O$	1.13	7.22
$Be_{0.19}Zn_{0.81}O$	1.35	7.62
$Be_{0.19}Mg_{0.42}Zn_{0.39}O$	1.36	9.00

In conclusion, we performed a systematic experimental and theoretical study of lattice parameters and bandgaps of quaternary BeMgZnO alloy for the whole range of compositions. The calculations using exchange tuned HSE06 hybrid functional (exchange fraction of 0.375) are in good agreement with the experimental data for MBE grown samples containing up to about 19% Be and 52% Mg in quaternary BeMgZnO alloy. The a and c lattice parameters were calculated within 1-2% accuracy in comparison with experimentally observed values. The effect of BeO content on the a lattice parameter is much stronger than that of MgO due to larger difference of lattice parameter of the former with ZnO. Further offset of 0.14-0.32 eV for $Be_{0.09}Mg_yZn_{0.91-y}O$ and higher for $Be_xMg_{0.39}Zn_{0.61-x}O$ (due to possible phase segregation) between theoretically predicted and measured bandgaps (in the available compositional range) is attributed to the temperature expansion of the lattice, temperature dependence of electron-phonon coupling, and excitonic effects. Composition independent bowing parameters were determined for ternary BeZnO and MgZnO alloys: $b_{Eg\_BeZnO}=6.94$ eV and $b_{Eg\_MgZnO}=0.237$ eV for bandgaps, and $b_{a\_BeZnO}=-0.043$ Å, $b_{a\_MgZnO}=-0.172$ Å and $b_{c\_BeZnO}=-0.043$ Å, $b_{c\_MgZnO}=0.061$ Å for a-lattice and c-lattice parameters, respectively. The large bandgap bowing b_{Eg_BeZnO} correlates with strong localization

of both CBM and VBM wavefunctions in BeMgZnO alloy, compared to bulk ZnO. Finally, it is important to note that, by using BeMgZnO alloy as a top barrier layer on Zn-polar ZnO, it is possible to achieve both tensile and compressive strain, where former cannot be achieved with MgZnO. This is advantageous to generate high density 2DEG by utilizing piezoelectric polarization for future generation (Be,Mg)ZnO/ZnO heterostructure field effect transistors.

2.3. Effect of Oxygen-to-Metal Ratio on Incorporation of Metal Species into Quaternary BeMgZnO Alloy Grown by P-MBE on c-Sapphire

Advanced ZnO based heterostructure and quantum well devices require precise control over composition, bandgap and lattice parameters of barrier layer during thin-film growth. Kinetics of chemical reactions on the growing surface play a critical role in MBE growth of compound materials in general, and BeO-MgO-ZnO quaternary solid solutions in particular. One can expect that the ratio of reactive-oxygen flux to metal flux would have a significant effect on composition of the BeMgZnO quaternary alloys and thus on many of material properties including bandgap, lattice parameters, dielectric constant, thermal stability etc. For the growth of BeMgZnO layers under metal-rich conditions (oxygen limited), a competition between different metal species to form a bond with oxygen is expected on the growing surface. If the surface mobility of adatoms is sufficiently high (at sufficiently high substrate temperature, T_S), one can expect the minimization of formation energy to be the mechanism governing the formation of BeMgZnO. In other words, we expect oxygen to form the most favorable bonds with available metal adatoms. This assumption applies only to layers with moderate Be and Mg content, when the phase segregation is suppressed. To the best of our knowledge, the solubility limits of Be and Mg for the $Be_xMg_yZn_{1-x-y}O$ alloy have not yet been established. However, for the samples grown at the same substrate temperature

and similar oxygen flux, as employed in this work, we were able to achieve quaternary single crystal alloys with compositions of $Be_{0.19}Mg_{0.42}Zn_{0.39}O$ and $Be_{0.12}Mg_{0.52}Zn_{0.36}O$ by varying metal fluxes.[67] Therefore, compositions below Be and Mg content of 0.19 and 0.52, respectively, should be below the phase segregation limit.

To confirm this hypothesis and develop a phenomenological model describing the formation process of BeMgZnO alloy, we have investigated metal incorporation rates during MBE growth of quaternary BeMgZnO layers as a function of reactive oxygen flux. Plasma density was evaluated from measurements of intensity of the oxygen *O radical line at 777.5 nm using Ocean Optics SD2000 fiber optic spectrometer to determine the relative amount of oxygen radicals flow for different settings of the mass flow controller. Linear relationship of the amount of *O radicals on O_2 flow was found for the discussed range of the gas flow. To obtain a first-hand insight into the formation process of BeMgZnO alloy, we performed *ab initio* calculations of formation energies H_f of the binary compounds and ternary alloy for the whole range of BeMgZnO compositions.

Thermodynamic stability of an alloy as a function of the constituent concentrations at zero temperature can be described by the formation energy. For all alloys compositions, when performing first principles were calculations of formation energies, equilibrium lattice constants, and relaxed atomic positions using Perdew-Burke-Ernzerhof (PBE)[68] parameterization of the GGA.[69] The electronic properties were calculated using exchange tuned HSE hybrid functional. The functional was tuned to reproduce the low temperature bandgap of ZnO which also results in bandgaps of wurtzite BeO and MgO within 3% error with the experiment. The structure model was based on a 72-atom supercell. The computational methods have been described in Ref. [67]. For

the given concentrations of Be and Mg, the formation energy of $Be_xMg_yZn_{1-x-y}O$ alloy can be found from the total energy calculated as

$$E_f(x, y) = E_{total}^{Be_xMg_yZn_{1-x-y}O} - xE_{total}^{BeO} - yE_{total}^{MgO} - (1-x-y)E_{total}^{ZnO}$$

(2)

where terms E_{total} are the total energies of the quaternary compound and the corresponding binaries normalized per atom. The accuracy of this approach can be evaluated from the computed formation enthalpies of the binary compounds involved in the formation of alloys. For example, the enthalpy of formation of ZnO is $\Delta H = E_{tot}(ZnO) - \mu_O - \mu_{Zn}$, where the chemical potentials μ of oxygen and zinc are taken from the calculated energies of an oxygen molecule and a Zn metal. Table 5 shows that for bulk wurtzite ZnO, HSE calculations yield -3.35 eV, compared to the measured value of -3.632 eV.[64] In the case of wurtzite BeO, the HSE calculation result is -6.04 eV, while the experimental value is -6.316 eV.[64] MgO is stable in rock salt structure, with computed formation enthalpy of -5.91 eV, while the measured value is -6.235 eV. [64] The formation enthalpy of the non-existent wurtzite phase of MgO is -5.68 eV. First, all formation energies are underestimated by 4-8%, indicating that the accuracy of equilibrium formation energy is a few percent. Second, formation enthalpies of the wurtzite and rock salt MgO differ by ~0.2 eV, therefore using the total energy of wurtzite MgO will also lead to ~0.2 eV error in the alloy formation energies.

Table 5. Heat of formation H_f for the binary components of the quaternary BeMgZnO

Compound	Crystal structure	Heat of formation, eV (experiment)	Heat of formation, eV (theory)	Error, % (theory vs. exp.)
BeO	Wurtzite	-6.316[64]	-6.042	-4.3%
MgO	Rocksalt	-6.235[64]	-5.906	5.3%
	Wurtzite	Unavailable	-5.678	-
ZnO	Wurtzite	-3.632[64]	-3.354	7.7%

The BeMgZnO alloy formation energies for the full range of Mg, Be, and Zn concentrations are shown in Figure 15. Positive values of formation energy indicate the trend towards phase separation. Almost parabolic positive formation energies for the BeZnO ternary indicate difficulties in the equilibrium formation of this alloy. On the other hand, MgZnO exhibits negative formation energies, indicating favorable conditions for the formation of this alloy. The competition between the two trends results in the lowest energy path on the BeMgZnO formation energy surface, for the fraction of Mg around 15% (for fraction of Be from 10 to 20%), with a saddle point at 61% of Be and 12% of Mg. Favorable concentrations of Mg are around 12-15%. Realistically, this corresponds to the experimentally observed increase in Be solubility with the addition of Mg to the incident flux. As discussed in Section 2.2, we reported a wurtzite single crystal $Be_{0.19}Mg_{0.42}Zn_{0.39}O$ with Be content beyond that achievable with ternary BeZnO. On the other hand Su *et al.*[15] reported stabilization of wurtzite MgZnO up to 57% of Mg by the addition of 1-2% of Be. Aforementioned results suggest a positive co-effect of both Be and Mg species on each other's solubility in the lattice of ZnO (at least for the samples with Be content up to 19% and Mg content up to 57%). It is important to note that, in order to reproduce the alloy formation in the wurtzite ZnO lattice, in the calculations of the alloy formation energy, the total energy of MgO in the wurtzite phase was used. As described above, this phase is unstable, which leads to an underestimated formation energy of MgZnO alloy by ~0.2 eV. Experimentally, maximum Mg content achieved in MgZnO lattice is 55%, at a substrate temperature 250°C[70] (in contrast to BeZnO, where the phase segregation accrues above 10-15%). At higher temperatures, phase segregation is often observed with MgO formed in rock-salt phase. Thus, overall energetic trend of Mg being better soluble in ZnO in comparison with Be is correctly reproduced by calculations, although negative formation energies of MgZnO are most likely unrealistic.
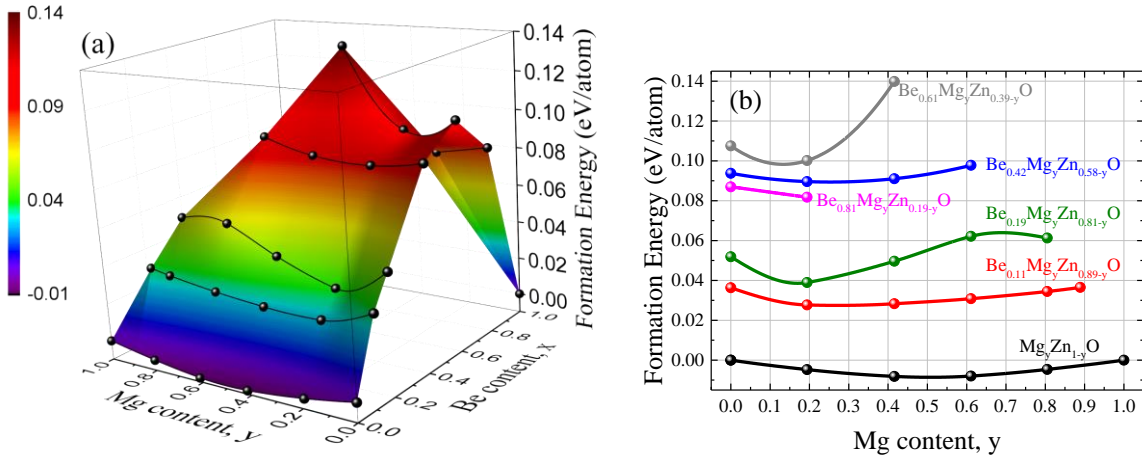
Figure 15. (a) The formation energy as a function of Be (x) and Mg (y) atomic fractions for $Be_xMg_yZn_{1-x-y}O$ alloy. The color surface represents the fit with the quadratic equation (Equation 2) to calculated points, which are indicated with solid spheres. (b) Directly calculated values in two dimensional presentation with spline fits.

Figure 16 shows bandgap, c lattice parameter, and growth rate of quaternary BeMgZnO alloy as functions of the O_2 flow. For the sample grown with the oxygen mass flow of 1.00 sccm the total metal flux has been adjusted to provide near-stoichiometric growth conditions, while three other samples were grown under metal-rich conditions, as determined from the metal flux measurements and test growths of ZnO at a substrate temperature of 400°C. As seen from Figure 16 (a), the c lattice parameter of the quaternary BeMgZnO alloy systematically decreases and bandgap increases with decreasing O_2 flow rate. These findings are consistent with the increase in Be and/or Mg content of the alloy with decreasing O_2 flow. Additionally, the reduction in lattice parameter and the increase in bandgap correlate with the observed systematic decrease in the growth rate with reducing O_2 flow (Figure 16 (b)].
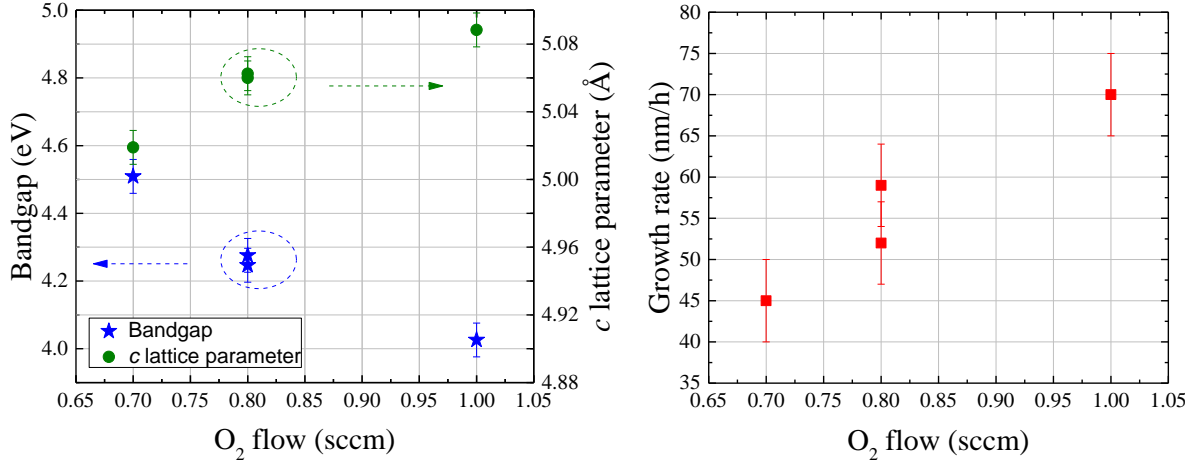
Figure 16. (a) The *c* lattice parameter, bandgap and (b) growth rate dependence on the O_2 flow. For the sample grown with the oxygen mass flow of 1.00 sccm the total metal flux has been adjusted to provide near-stoichiometric growth conditions, while three other samples were grown under metal-rich conditions. For all discussed samples the metal fluxes were kept constant.

The composition of quaternary $Be_xMg_yZn_{1-x-y}O$ alloy can be fully described with two parameters *x* and *y*, for Be and Mg contents, respectively, as discussed in Section 2.1. Using the *c* lattice parameter and bandgap values of quaternary alloy it is possible to determine Be and Mg contents of the BeMgZnO alloy. Tuning the theoretical calculations to match the experimentally observed optical bandgap of ZnO, $E_g^{ZnO} = 3.26 eV$, and *c* lattice parameter, $c^{ZnO} = 5.2042$ Å, allowed accurate prediction of the experimentally observed bandgap and *c* lattice parameter of quaternary BeMgZnO for the whole range of compositions. A generic fitting equation is used instead to provide a better fit to the calculated values: [67]

$$E_g(x, y) = 3.26 + 1.33x + 5.29x^2 + 3.23y - 0.65y^2 \ [eV] \tag{3}$$

$$c(x, y) = 5.204 - 1.052x + 0.138x^2 - 0.239y - 0.024y^2 \ [Å] \tag{4}$$

Using the experimental bandgap and *c* lattice parameter, simultaneously solving equations (3) and (4) allows determination of compositions of $Be_xMg_yZn_{1-x-y}O$ samples Table 6 shows the

37

compositions and the change in the Be and Mg contents with the change in the oxygen flow. Sample B and C are grown under the same growth condition in order to confirm the reproducibility in the experiment. As expected, Be and Mg contents increase with decreasing oxygen flow. The increase in the growth rate with increasing reactive-oxygen flow indicates that the total incorporation of metal species increases. By using the known Be and Mg contents in the samples under consideration, we can find the effective growth rates of the binaries composing the quaternary BeMgZnO alloy. The effective growth rates of binaries for sample A grown under near stoichiometry condition were found to be 4 nm/h, 15 nm/h and 51 nm/h for BeO, MgO and ZnO, respectively.

. In order to quantify the effect of the oxygen flow on the effective growth rates of binaries (BeO, MgO, ZnO) and thus incorporation coefficients of corresponding metals (Be, Mg, Zn), the calculated compositions and measured growth rates were used by solving systems of equations for each binary of the form:

$$
\begin{cases}
\dfrac{r_{BeO}^{BeMgZnO}}{r_{BeO}^{BeMgZnO} + r_{MgO}^{BeMgZnO} + r_{ZnO}^{BeMgZnO}} = 0.06 & \left(\text{Be conent for A is } 0.06 \right) \\[4mm]
\dfrac{r_{Be}^{*}}{r_{BeO}^{BeMgZnO} + r_{MgO}^{BeMgZnO} + \left(r_{ZnO}^{BeMgZnO} - (r_A - r_B) \right)} = 0.08 & \left(\text{Be conent for B is } 0.08 \right)
\end{cases}
\tag{5}
$$

where $r_{BeO}^{BeMgZnO}$, $r_{MgO}^{BeMgZnO}$, $r_{ZnO}^{BeMgZnO}$ are the effective binary growth rates of BeO, MgO, ZnO, respectively; and r_A, r_B are the measured BeMgZnO growth rates for films A and B, respectively.

It was found that incorporation rates of Be and Mg into the growing film are virtually constant and equal to unity due to low metal vapor pressure and high melting point, i.e. $\alpha_{Mg} \approx \alpha_{Be} \approx 1$,

while the Zn incorporation varies. The excess amount of Zn atoms re-evaporates from the sample surface which is possible due to much higher equilibrium vapor pressure of Zn compared to those of Mg and Be at the growth temperature of 400°C.

Table 6. The composition, O_2 flow, VI/II ratio, the growth rate and the incorporation coefficient α_{Zn} of the samples discussed in Section 2.3.

Sample	Composition	O_2 flow, sccm	VI/II ratio	Growth rate[*], nm/h	α_{Zn}
Z	$ZnO^{\dagger}$	1.2	1	80	0.3
A	$Be_{0.06}Mg_{0.22}Zn_{0.72}O$	1.0	0.9	70	0.24
B C	$Be_{0.08}Mg_{0.28}Zn_{0.64}O$	0.8	0.7	56	0.17
D	$Be_{0.10}Mg_{0.34}Zn_{0.56}O$	0.7	0.6	45	0.12

[*]The growth rate shown for samples B and C corresponds to an average value

[†]ZnO sample has ~10% higher Zn flux than BeMgZnO samples.

The absolute value of the Zn incorporation coefficient, α_{Zn}, is defined as $\alpha_{Zn} = r_{ZnO}^{BeMgZnO} / r_{ZnO}^{max}$, where r_{ZnO}^{max} is the maximum possible ZnO growth rate for the particular Zn flux, i.e. for $\alpha_{Zn} = 1$, the growth rate corresponds to 100% incorporation of arriving Zn atoms into ZnO. The r_{ZnO}^{max} value calculated using Zn flux measurements with the quartz thickness monitor and Zn/ZnO molar-mass and density ratios was found to be $r_{ZnO}^{max} = 215$ nm/h for $T_{Zn}=315°C$. However, the actual ZnO growth rate depends on the surface polarity (being about a factor of 2 higher for Zn-polar material compared to that of O-polar[54,71]) and substrate limiting the Zn sticking coefficient. The growth rate of 65nm/h for the O-polar ZnO at $T_S = 400°C$, corresponds to $\alpha_{Zn}=0.3$, which is in agreement with the value reported by Ivanov et al.[72] The α_{Zn} values for different samples are shown in Table 4. As seen from the table, when Be and Mg fluxes are present (growth of BeMgZnO), Zn incorporation

decreases with reducing oxygen to metal ratio. Under metal-rich conditions, α_{Zn} varied from 0.3 to 0.12 for the change in the oxygen flow from 1.0 sccm to 0.7 sccm.

Under thermal equilibrium, ZnO heat of formation is much less negative than those of BeO and wz-MgO, which are very close to each other. Additionally, the calculated H_f for BeMgZnO varies only by 0.15 eV/atom for the whole range of compositions, and y 0.05 eV/atom for the compositional range in samples A-D (Mg below 25% and 10% for Mg and Be, respectively). Thus, linear interpolation is a reasonable approximation to estimate the H_f of discussed BeMgZnO samples. If the surface mobility during growth is sufficient for adsorbed metal species to find and form the most favorable bonds, the composition of the quaternary alloy should be governed by the formation energies of corresponding binaries to minimize the total H_f of BeMgZnO alloy. Since for a BeMgZnO alloy the formation of Zn-O bond has the lowest probability, the metal-rich (or oxygen-deficient) growth conditions would lead to higher incorporation of Be and Mg, while the Zn species that are not able to form chemical bonds with oxygen, re-evaporate from the surface owing to high Zn vapor pressure. This would result in the relative increase of Be and Mg content in the BeMgZnO lattice, and corresponding changes in electronic and structural properties should be observed. It should be noted that MBE growth conditions are away from thermodynamic equilibrium; therefore, the theory can explain only a general trend rather than providing quantitative predictions.

In conclusion, the dramatic effect of flux of reactive oxygen on the composition of BeMgZnO alloy grown by MBE with constant metal fluxes is observed. Relative fraction of Mg and Be in the alloy systematically increases with reducing the ratio of reactive oxygen flux to the total metal flux (Be+Mg+Zn). With the same metal fluxes used, $Be_{0.06}Mg_{0.22}Zn_{0.72}O$ (E_g=4 eV) forms under near stoichiometric conditions (VI/II = 0.9), whereas $Be_{0.10}Mg_{0.34}Zn_{0.56}O$ (E_g=4.5 eV)

grows under highly metal-rich conditions (VI/II = 0.6). The corresponding change in the ZnO

incorporation coefficient α_{Zn} during BeMgZnO growth is α_{Zn} = 0.24 for VI/II = 0.9 and α_{Zn} = 0.12

for VI/II = 0.6, where α_{Zn} for binary ZnO growth under similar conditions is 0.3. These findings

are qualitatively explained by the difference in heat of formation H_f of binary compounds and the

quaternary alloy. As revealed by theoretical HSE06 calculations, formation energy -3.354 eV of

ZnO is less negative compared to those of BeO (-6.042 eV) and wz-MgO (-5.678 eV) that gives

rise to lower probability of Zn incorporation into BeMgZnO lattice compared to Mg and Be under

metal-rich conditions. Substrate temperature of 400ºC is sufficient to re-evaporate unbounded Zn

species from the surface. For the case when substrate temperature is low, we should expect similar

changes in the incorporation rates of all Be, Mg and Zn, i.e. composition would not change with

varying oxygen flow.

2.4. Effect of Oxygen-to-Metal Ratio on Surface Roughness, RHEED and Electrical Conductivity of O-polar BeMgZnO on c-Sapphire

The fabrication of high quality heterostructures require low interface surface roughness.

Figure 17 shows the dependence of Root-Mean-Square (RMS) surface roughness on metal

(Zn+Mg+Be) to oxygen ratio (II/VI ratio). It was found, that samples grown under slightly oxygen

rich conditions (II/VI=0.8-0.9) exhibit the minimum surface roughness (~1 nm); where samples

grown under both oxygen rich or metal rich conditions show increased surface roughness. The

inserts to Figure 17 shows corresponding RHEED images that were taken at the end of each growth

that support the trends in surface roughness. BeMgZnO samples growth under metal or oxygen

rich conditions show 3D growth mode. This island growth mode results in high RMS roughness

that is observed with AFM. The sample growth under slightly oxygen rich conditions shows nearly

2D growth mode.
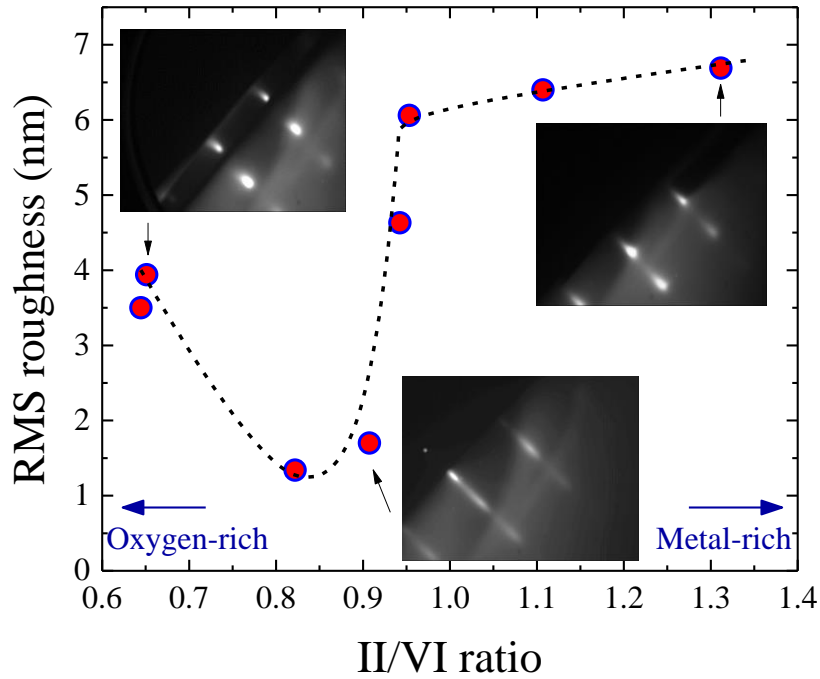
Figure 17. Dependance of RMS surface roghness on II/VI ratio during BeMgZnO growth on c-sapphire. Insters are RHEED images taken at the end of each growth with errors indicating corresponding growth condition

Figure 18 shows an AFM 2.5 x 2.5 μm scan of $Be_{0.1}Mg_{0.4}ZnO$ with RMS surface roughness

below 0.5 nm. Further reduction in surface roughness shown in Figure 17 may be explained with

higher compensation effect between Mg and Be species in the quaternary layer.
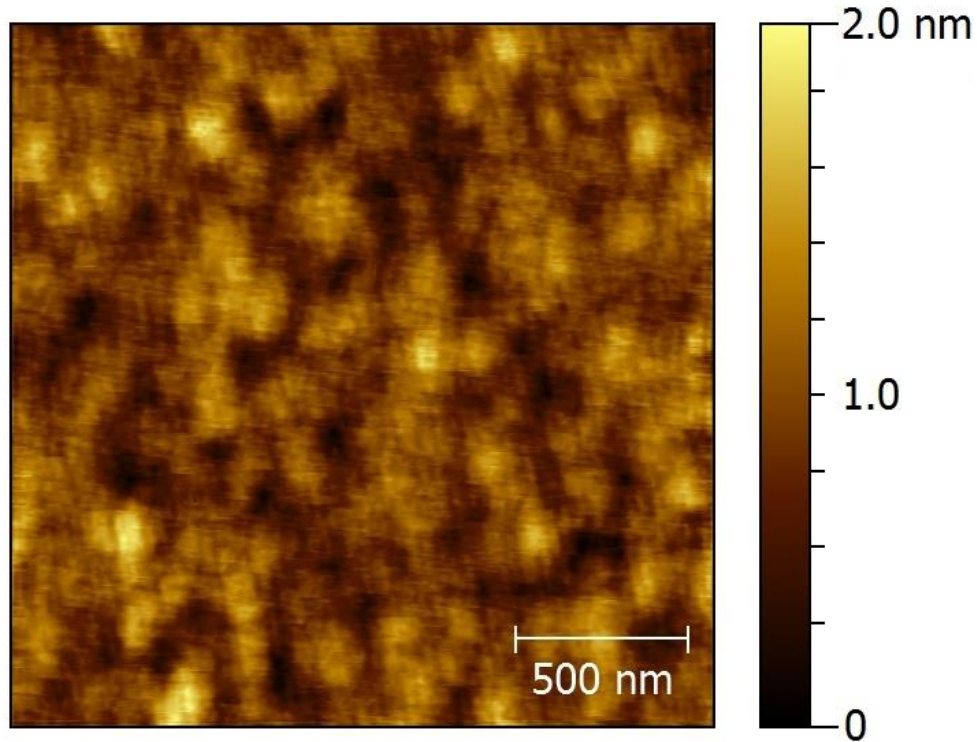
Figure 18. AFM image of Be0.1Mg0.4ZnO. RMS surface roughness < 0.5 nm.

With regard to the effect of metal to oxygen ratio on electrical conductivity, in the preliminary study it was found that BeMgZnO films grown under oxygen rich conditions are semi-insulating ($>10^5$ $\Omega \cdot$cm), while the films grown under metal rich conditions are more conductive ($\sim 10^2$ $\Omega \cdot$cm). We have also found that the films grown under O-rich conditions remain insulating despite Ga doping ($\sim 1 \cdot 10^{18}$ cm^{-3} of Ga donors) which suggest high degree of compensation in such material. The ability to dope quaternary BeMgZnO may be essential for fabrication of wide bandgap transparent conductive oxide (TCO) films[24] or modulated-doping field effect transistors (MODFET) with BeMgZnO barriers.

In conclusion, the appropriate growth conditions must be chosen for the specific needs. The optimum metal-to-oxygen ratio for the O-polar BeMgZnO growth on c-sapphire, for the minimum

surface roughness, lays in the vicinity of 0.9. Additionally, samples grown under oxygen rich

conditions are semi-insulating where those grown under metal rich conditions are semiconducting.

Chapter 3. Optical quality, localization, and carrier dynamics in BeMgZnO

The bandgap value is an extremely important parameter that is typically deducted from an absorption edge, as was done for previously discussed BeMgZnO films growth on c-sapphire. However, for films grown on lower bandgap material such as GaN, the absorption measurement cannot reveal the bandgap and thus other methods must be used. The photoluminescence (PL) peak position with the knowledge of Stokes shift can provide a fair estimate of the bandgap value of the quaternary alloy. Moreover, the performance of heterostructure devices is highly sensitive to the material quality, which in turn is governed by the number and type of defects. On the other hand, carrier dynamics is extremely sensitive to the type and quality of defects and therefore can be used as a powerful measure of material characteristics. Additionally, the carrier lifetimes are strongly affected by carrier localization, which is well pronounced in wide-bandgap semiconductor alloys such as (Be,Mg)ZnO, (Al,In)GaN due to large differences in metal covalent radii and the lattice constants of the binaries. These differences result in strain-driven compositional variations within the film and consequently large potential fluctuations, in addition to that possibly caused by defects. To investigate the potential effects of localization in Zn-polar BeMgZnO quaternary alloys, temperature-dependent carrier dynamics were investigated by time resolved photoluminescence (TRPL).

Figure 5 shows the cross-sectional schematics of the O-polar and Zn-polar BeMgZnO samples investigated in this work. The quaternary thin films were grown on epitaxial carbon compensated high resistivity GaN(0001)/Al$_2$O$_3$(0001) templates. Pyrolytic boron nitride (PBN) crucibles were used for Zn and Mg sources and a BeO crucible for the Be source. The GaN templates were cleaned ex situ with aqua Regia to remove possible metal contamination and

followed by immersion in a HCl : H_2O = 1 : 1 solution to remove any gallium oxide (Ga_2O_3) from the surface. After loading the substrate to the growth chamber, GaN surface is thermally cleaned at 625 °C for 15 min. Templates were exposed to Zn flux prior to ZnO growth to terminate the GaN surface with Zn adatom and prevent the formation of Ga oxide. [53] By varying VI/II ratio during low temperature ZnO growth we could control polarity of the growth layer.[54] First, a ~15 nm-thick low temperature ZnO buffer layer was grown at 300 °C followed by annealing at 730 °C to achieve an atomically flat surface. Then, a 120 nm thick high temperature ZnO layer was grown at 680 °C. BeMgZnO films were deposited at ~1.3 x 10^{-5} Torr oxygen pressure with thicknesses of 130 nm and 100 nm for Zn-polar and O-polar films, respectively. The average growth rate of Zn-polar samples was 170 nm/h and that of O-polar was 75 nm/h.

PL and TRPL measurements were performed using frequency-tripled Ti:Sapphire laser excitation (4.68 eV) with 150 fs pulse width and 80 MHz repetition rate. PL was analyzed by a liquid nitrogen cooled charge couple device (CCD) camera connected to a 30 cm focal length monochromator. TRPL was analyzed by a spectrometer attached to a 30 ps resolution Hamamatsu streak camera. The photo excited carrier densities were estimated as 8x10^{15} cm^{-3} and 8x10^{17} cm^{-3} for PL and TRPL measurements, respectively. The excitation spot size on the sample surface was 100 μm in diameter.

The compositions of quaternary $Be_xMg_yZn_{1-x-y}O$ alloys studied here were deduced by comparing the measured *c* lattice parameters (from X-ray diffraction) and bandgaps (from absorption edge) with previously determined values for the full range of compositions.[59,73] The lattice parameters, low temperature PL peak positions and Mg/Be ratios are shown in Table 7.

Figure 19 shows low temperature (LT) and room temperature (RT) steady state PL spectra of BeMgZnO samples grown on GaN measured at 15 K with 4.68 eV excitation. From LT spectra,

samples I and IV with the highest Mg/Be ratio, $r_{Mg/BE}$, and lowest PL energy peak position, E_{PL}, exhibited the highest PL intensity. Sample II has ~0.1 eV higher E_{PL} than that of sample I. At LT, the PL intensity, I_{LT}, is inversely proportional to $r_{Mg/Be}$. Sample III, despite its higher PL peak position, featured a higher I_{LT} than that of sample II due to mutual compensation effects between Be and Mg (higher $r_{Mg/Be}$ then that of sample II). On the other hand, at RT sample III with $r_{Mg/Be}=2.5$ shows highest RT PL intensity, I_{RT}. The reason is discussed later in the text. Additionally, subbandgap BL2 GaN transitions are clearly observed. Demchenko *et al.*[74] attributed BL2 transitions to a hydrogen-carbon defect complex, either $C_N O_N$-H_i or C_N-H_i. Weak band-to-band GaN luminescence is absorbed in the ZnO layer and masked with the BeMgZnO luminescent shoulder. The Zn-polar sample IV has stronger LT PL intensity and similar bandgap in comparison to sample I, which may be due to better crystal quality of the quaternary layer provided by lower film thickness (100nm for IV and 130nm for I, II, III), which in turn may provide better crystal quality of the quaternary layer. The absorption depth at 265nm excitation is ~50nm for our samples.
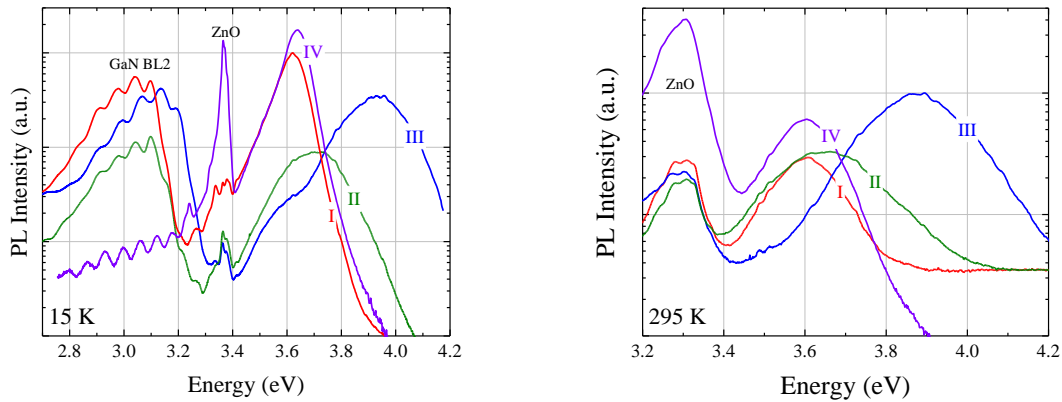
Figure 19. Low temperature photoluminescence of O-polar BeMgZnO samples grown on GaN. Sample I is $Be_{0.04}Mg_{0.17}Zn_{0.79}O$, sample II is $Be_{0.11}Mg_{0.15}Zn_{0.74}O$, sample III is $Be_{0.10}Mg_{0.25}Zn_{0.65}O$ and sample IV is $Be_{0.03}Mg_{0.18}Zn_{0.79}O$.

To evaluate the carrier dynamics in the BeMgZnO layers, time-resolved PL measurements were performed at 15 K. The PL transients were fitted using single exponential decays for samples I, II, III and double exponentials for sample IV. Figure 20 shows PL decay dependence on the emission energy. The time-integrated spectra exhibit two peaks that correspond to buffer ZnO (3.39eV) and quaternary BeMgZnO (3.62 – 3.90 eV) with dramatically different decay time values. All decay times for BeMgZnO layers monotonically decrease with increasing emission energy. Such behavior is characteristic for localized excitons. It is important to note that the measured buffer ZnO decay times are not representative as they are very close to the system response time.

The observed decay times can be expressed as

$$\tau(E) = \frac{\tau_0}{1 + \exp\left(\dfrac{E - E_0}{\Delta_0}\right)} \tag{6}$$

where τ_0 is the exciton recombination time in the absence of the energy transfer, Δ_0 is the degree of the localization depth in the band tail state, and E_0 is the characteristic energy where recombination rate equals the delocalization rate. It is assumed that above the characteristic energy ($E>E_0$) localized excitons will transfer out of localized states and eventually undergo nonradiative recombination; below the characteristic energy ($E<E_0$) localized excitons do not have sufficient energy and undergo radiative recombination. Longer decay times of Zn-polar sample IV were used for the fitting.
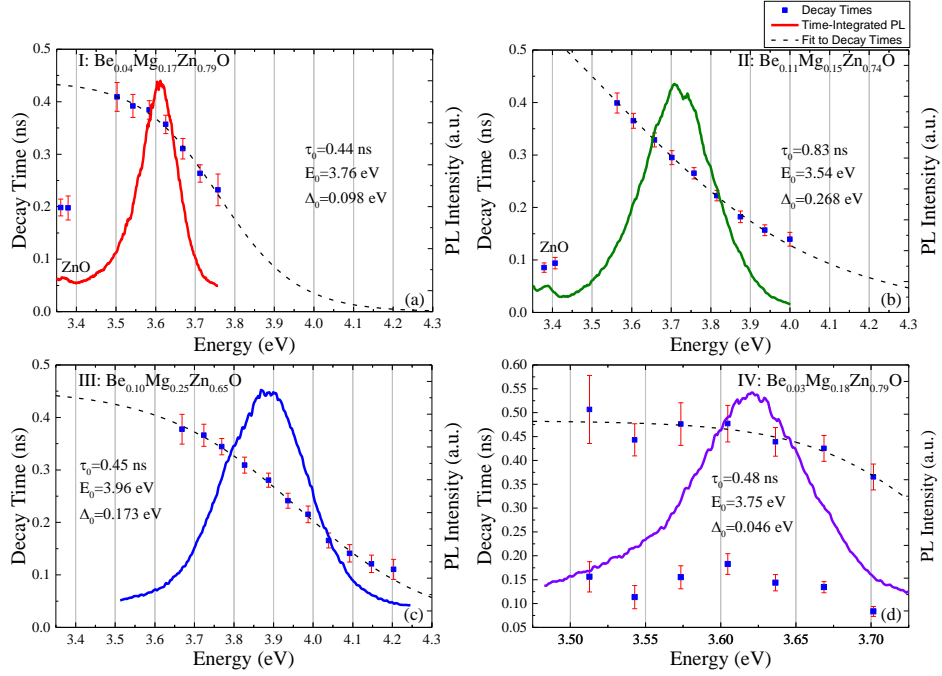
Figure 20. PL decay time dependence on the emission energy at 15 K and time integrated PL for a) sample I: $Be_{0.04}Mg_{0.17}Zn_{0.79}O$; b) sample II: $Be_{0.11}Mg_{0.15}Zn_{0.74}O$; c) sample III: $Be_{0.10}Mg_{0.25}Zn_{0.65}O$; d) sample IV: $Be_{0.03}Mg_{0.18}Zn_{0.79}O$. The spectral sampling width is 1 nm. The localization parameters are determined from the fit with Equation (6).

Table 7 summarized the localization parameters obtained by fitting experimental decay times with Equation (6). Sample IV with the smallest E_{PL} and the highest $r_{Mg/Be}$ shows the smallest localization depth Δ_0. Sample II with the lowest $r_{Mg/Be}$ shows the highest localization depth Δ_0. On the other hand, sample III that has the highest PL peak energy and intermediate Mg/Be ratio shows significantly smaller Δ_0 in comparison with sample II. Despite the increase in PL peak position, the higher $r_{Mg/Be}$ supports smaller localization depth by allowing Be and Mg to mutually compensate each other's effects on the lattice of ZnO by reducing formation energy and strain. Sample II has almost twice higher decay time τ_0 in comparison to other two samples, which possibly originates from high degree of localization or potential fluctuations. All O-polar samples show single exponential decays and Zn-polar samples shows double exponential decay with

shorter decay time related to nonradiative recombination. The longer decay time of sample IV that is related to radiative processes is significantly longer suggesting enhanced optical quality in comparison to that of O-polar samples. No TRPL investigation was reported for BeMgZnO or BeZnO. Thus, only values for MgZnO and CdZnO are presented for comparison. Chernikov *et al.*[75] reported longer decay time ($\tau_0 = 1$ ns) and smaller localization depth ($\Delta_0 = 0.06$ eV) and a characteristic energy of $E_0 = 3.90$ eV for $Mg_{0.21}Zn_{0.79}O$ with low temperature bandgap of 3.75 eV.

Table 7. Composition, Mg to Be content ratio ($r_{Mg/Be}$), out-of-plane lattice parameter (c), PL peak position (E_{PL}), characteristic energy (E_0), the exciton recombination time in the absence of the energy transfer (τ_0), PL transients (τ), degree of localization depth determined from the fit with Equation (6) to the spectral dependence of the decay time (Δ_0), and ΔE_t is the observed temporal redshift of the PL peak position.

	Sample	$r_{Mg/Be}$	c, Å	E_{PL}, eV	E_0, eV	τ_0, ns	τ, ns	Δ_0, meV	ΔE_t, meV
I	$Be_{0.04}Mg_{0.17}Zn_{0.79}O$	4.3	5.143	3.62	3.76	0.44	0.294	98	8
II	$Be_{0.11}Mg_{0.15}Zn_{0.74}O$	1.4	5.124	3.69	3.54	0.83	0.300	268	55
III	$Be_{0.10}Mg_{0.25}Zn_{0.65}O$	2.5	5.117	3.93	3.96	0.45	0.294	173	42
IV	$Be_{0.03}Mg_{0.18}Zn_{0.79}O$	6		3.64	3.75	0.48	0.485 (τ_1) 0.169 ($\tau 2$)	46	10
[75]	$Mg_{0.21}Zn_{0.79}O$	N/A	-	3.75	3.90	1		60	-
[76]	$ZnO/Mg_{0.27}Zn_{0.73}O$ MQW	N/A	-	3.44	3.64	0.19		13.6	-
[77]	$Zn_{0.91}Cd_{0.09}O$	N/A	-	2.65	2.96	0.065		70	-
	$(Zn_{0.84}Cd_{0.16}O)$	N/A	-	(3.00)	(2.76)	(0.023)		(55)	-

The temporal dependence of the PL peak position for BeMgZnO samples grown on GaN is shown in Figure 21. As evident from Figure 20, decay rates at high emission energies are higher. This results in the redshift of the PL spectra with time. The observed redshifts ΔE_t are 10 meV, 8 meV, 55meV, and 42 meV for samples IV, I, II, and III, respectively, under the same excitation density. Samples with higher Δ_0 also show higher ΔE_t.
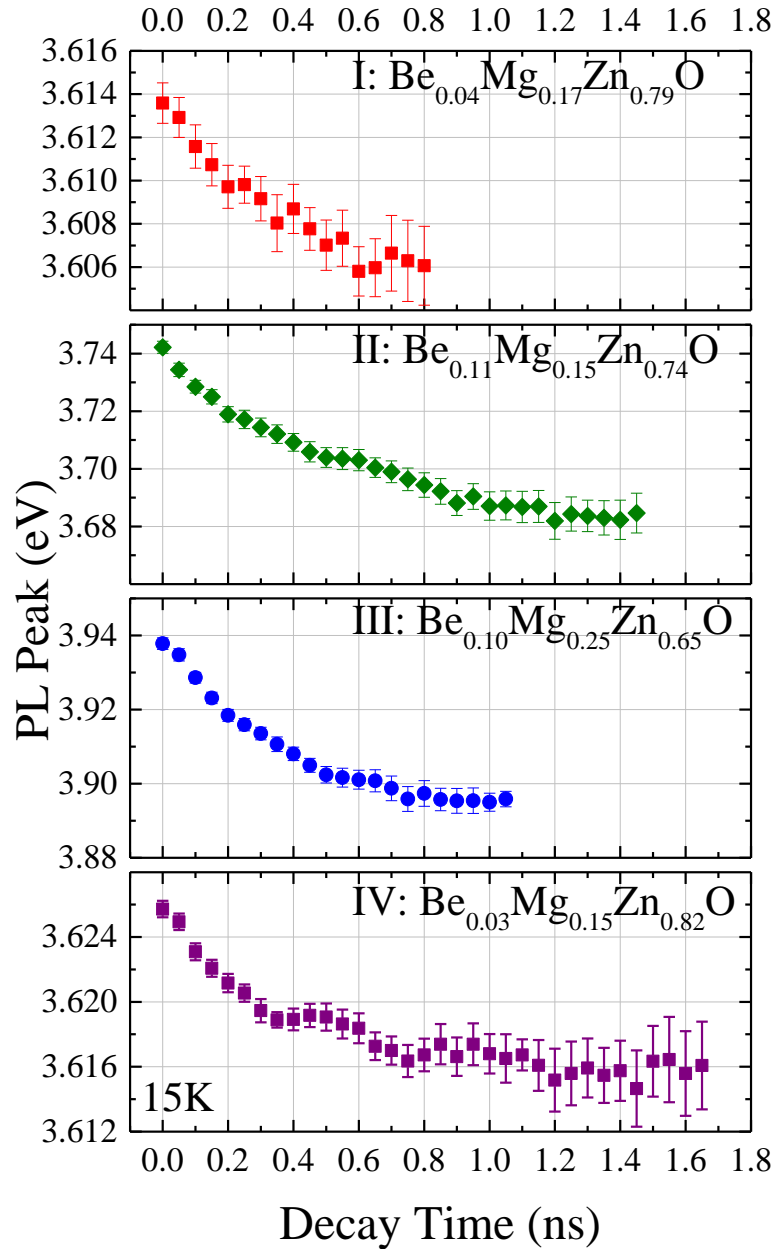
Figure 21. Temporal dependence of PL peak position of O-polar BeMgZnO samples grown on GaN at 15 K. Delay time equal to zero corresponds to the moment of pulse excitation. Note, vertical scales are different.

There are two potential possibilities explaining large shift in the peak position. The first one is potential fluctuations that originate from an inhomogeneous distribution of charged defects.[78]

The diagonal tunnel transitions with reduced energy take a longer time to recombine than direct fast transitions and, therefore, redshift is expected as time progresses. Another possibility is band filling of the localized states that would result in carriers occupying higher energy non-localized states; with time, localized states will become available and remaining de-localized carriers would fall-in to the localized states which would result in the observed temporal redshift in the PL spectra. Both of these processes may exist simultaneously. However, no change in FWHM of PL peak position was observed with change of excitation intensity or temporal PL evolution (see Figure 22 for the excitation dependent PL of sample IV).
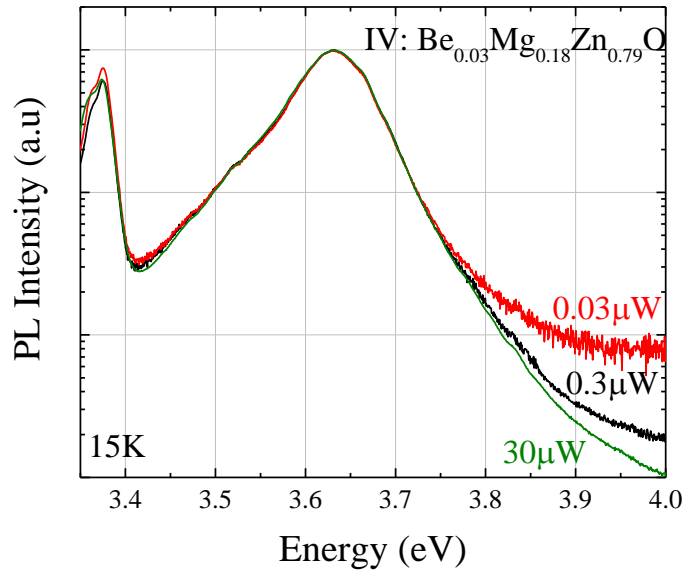
Figure 22. Excitation dependence of steady state PL of sample IV $Be_{0.03}Mg_{0.18}Zn_{0.79}O$ at 15K.

Figure 23 shows that both the dependence of degree of localization depth Δ_0 and the temporal redshift of the PL peak ΔE_t are decreasing with increasing the Mg/Be content ratio. Such dependence may be explained by mutual compensation of ZnO lattice distortion and minimization

52

of formation energy due to incorporation of Mg and Be.[15,55,79] A lower Mg/Be ratio would result in stronger internal strain and thus strain-driven potential fluctuations and localizations. The authors do not imply that the carrier localization is a direct measure of material quality. Localized carriers have higher probability to recombine radiatively in the localized state, unless there are non-radiative centers in close proximity to the potential minima. However, if the localization is driven by a strong internal strain which also generate high density of defects acting as nonradiative recombination channels, localizations centers may be located near non-radiative center and confine carriers for non-radiative transitions.
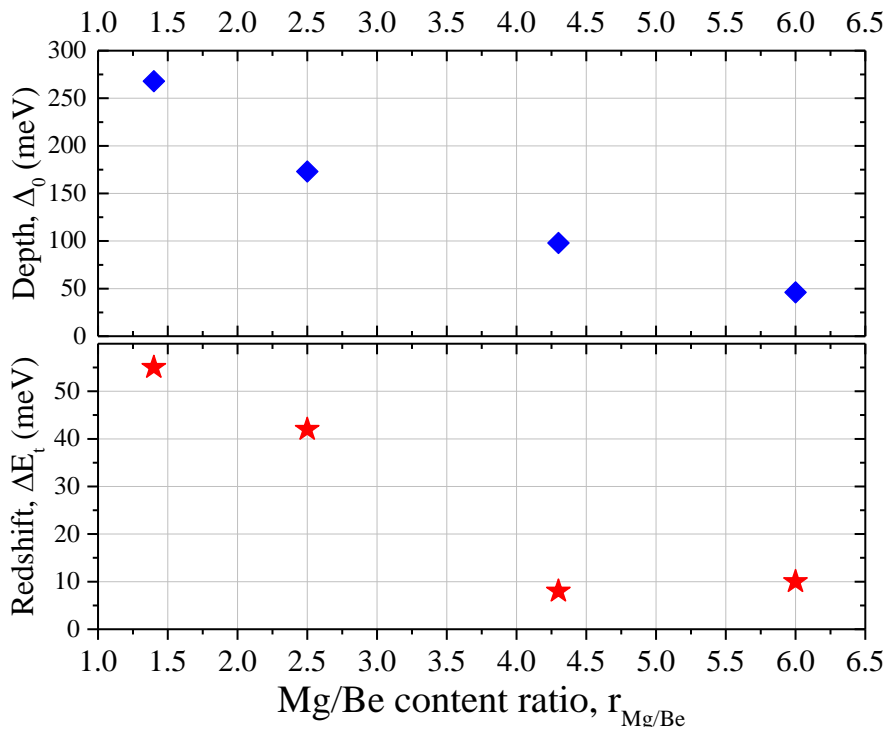
Figure 23. The dependence of the degree of localization depth Δ_0 (top) and the temporal redshift of the PL peak ΔE_t (bottom) on $r_{Mg/Be}$ content ratio.

The presence of local potential minima is often verified with temperature dependence of the PL peak position. To confirm the presence of localized states that were observed with TRPL, temperature dependent PL measurements were performed for sample I and sample II with the lowest and the highest Δ_0, respectively, and the results are shown in Figure 27. The S-shape behavior of PL peak position, which is an evidence of the presence of localized states, was observed for sample I (see Figure 27(a)). At very low temperatures, photo-excited carriers are localized and recombine radiatively at localized states with various depths and do not have sufficient energy to overcome the local barrier and migrate to the deepest localized state. With a rise of the temperature up to 180 K, excitons will gradually gain thermal energy sufficient to overcome local barriers and reach the deepest localized states that results in the redshift. Additionally, thermal lattice expansion and temperature dependence of electron-phonon coupling will also result in redshift with increasing temperature. With a further increase in temperature, above 180 K, the localized excitons gain sufficient thermal energy to delocalize, and as a result the blue shift is observed. At higher temperatures, the reduction in bandgap again governs the temperature dependence of PL peak position. The degree of the localization effect can be estimated by fitting the temperature dependence of PL peak position with modified Varshni equation:[80,81]

$$E_g(T) = E_g(0) - \frac{\alpha T^2}{(\beta + T)} - \frac{\sigma^2}{k_B T}$$
(7)

where $E_g(0)$ is the energy gap at T=0, α and β are empirical Varshni coefficients, and σ indicates the degree of localization effect; k_B is the Boltzmann constant. For sample I, $Be_{0.04}Mg_{0.17}Zn_{0.79}O$, with high Mg/Be ratio $\sigma = 22$ meV. The fitted Varshni coefficients α and β for sample I are not representative due to carrier redistribution and delocalization effects and therefore are not shown here. For sample II, $Be_{0.11}Mg_{0.15}Zn_{0.74}O$, no S-shaped behavior was

54

observed (see Figure 27(b)) due to high degree of localization – excitons are localized even at room temperature. The emission peak energy in this case is most commonly fitted with the Varshni's equation, $E_g(T) = E_g(0) - \alpha T^2(\beta + T)$, i.e. Equation (7) without $\sigma^2/k_B T$ term. The calculated fitted parameters for $Be_{0.07}Mg_{0.10}Zn_{0.83}O$ are $E_g(0) = 3.70$ eV, $\alpha = 1.2 \cdot 10^{-4}$ eV/K and $\beta = 37$ K. Ko et al.[82] reported $\alpha = 7.2 \cdot 10^{-4}$ eV/K and $\beta = 1077$ K for ZnO and such coefficients result in higher PL redshift with increasing temperature. We may only speculate that in Sample II showing the highest Δ_0, excitons localized in the deepest state would gradually redistribute with increasing temperature between slightly shallower states and thus smaller redshift is observed.
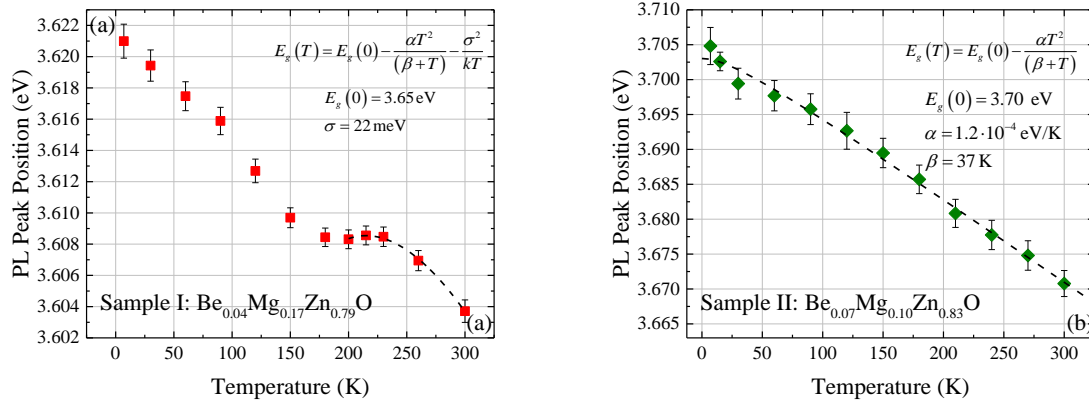
Figure 24. Temperature dependence of PL peak position for (a) $Be_{0.04}Mg_{0.17}Zn_{0.79}O$ and (b) $Be_{0.11}Mg_{0.15}Zn_{0.83}O$.

Both Equation (6) and Equation (7) are empirical and provide means to estimate the degree of localization using TRPL and temperature dependent PL, respectively. For sample I, $Be_{0.04}Mg_{0.17}Zn_{0.79}O$, the degree of localization Δ_0, determined from TRPL, is about five times higher than σ determined from temperature dependent PL. Additionally, for sample I with $\Delta_0 = 98$ meV, we observe the valley around 180 K. On the other hand, for sample II with $\Delta_0 = 268$

55

meV, no S-shape behavior was observed. We suspect that in order to observe the valley in the PL peak position due to delocalization of carriers it is necessary to reach temperatures higher than 300K. The exact relationship between Δ_0 and σ requires further investigation.

Figure 25 shows the dependence of the RT to LT ratio, $r_{RT/LT}$, on the Mg/Be ratio, $r_{Mg/Be}$, and localization depth, Δ_0. $r_{RT/LT}$ increases with increasing $r_{Mg/Be}$ and decreasing Δ_0. This is also a result of inverse proportionality between $r_{Mg/Be}$ and $r_{RT/LT}$. The reason for this dependence may be the following: for samples with a higher Mg/Be ratio (sample I and IV), which is closer to ZnO matched composition ($r_{Mg/Be}\sim13$),[73] and minimization of formation energy ($r_{Mg/Be}\sim10$),[79] LT PL is higher and localization depth Δ_0 is lower. With reducing $r_{Mg/Be}$, the compensation effects between Mg and Be weaken which increases both the number of defects as well as strain induced localization Δ_0. On the other hand, higher localization depth provides higher carrier confinement which supports radiative transitions at elevated temperatures. Therefore, for RT PL there exists ideal $r_{Mg/Be}$. In our case this ratio is close to that ratio of sample III, which is $r_{Mg/Be}=2.5$. The possible reason for sample IV having better efficiency at RT in comparison to sample I may be due to the thinner barrier layer and thus possible better crystal quality. Nevertheless, the Mg/Be ratio is a dominant factor influencing RT efficiency.
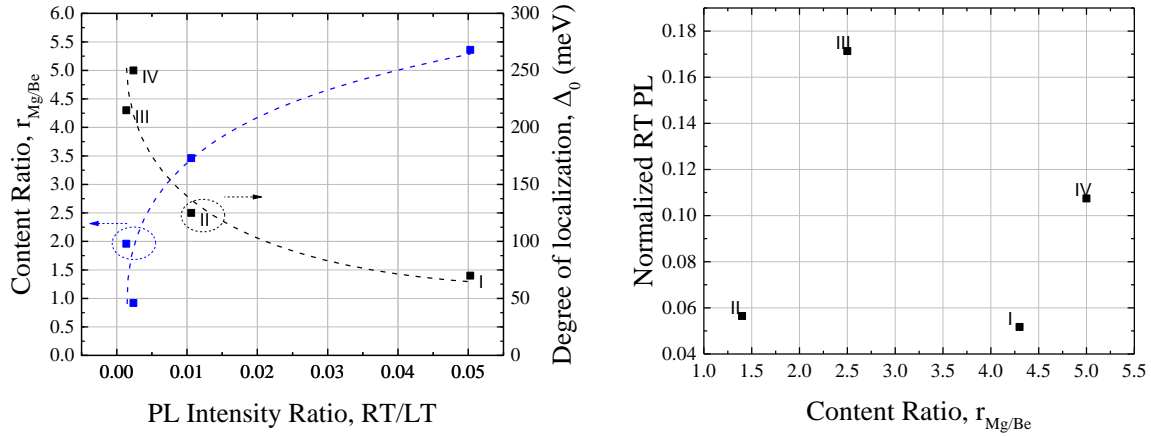
Figure 25. (a) The relation between content ratio, $r_{Mg/Be}$, and degree of localization, Δ_0, with RT to LT PL intensity ratio, $r_{RT/LT}$; b) RT PL normalized by the highest LT PL value (for sample IV)

To further explore potential fluctuations in BeMgZnO samples, the absorption and PL measurements were performed on the samples grown sapphire with different bandgaps. Direct growth of O-polar samples on sapphire allows measurement of absorption impossible for the samples grown on lower bandgap and thick GaN templates. Figure 26 shows the comparison between room temperature PL peaks and absorption edges of O-polar BeMgZnO samples, the difference between which is defined as the Stokes shift. The shift increases with increasing bandgap, which suggests the increase in the band tail states introduced by potential fluctuations and alloying. Additionally, the comparison between BeMgZnO and MgZnO grown by Liu et al.[83] (see Figure 26(b)) reveals that the quaternary alloy exhibit stronger Stokes shift than that of the ternary MgZnO alloy. The possible reason for it may be insufficient Mg/Be ratio to compensate the internal strain that results in stronger localization and potential fluctuations. As regarding to BeMgZnO samples grown on GaN, we expect higher structural quality of this material and thus smaller potential fluctuations and localization compared to those grown on sapphire due to smaller lattice mismatch at the ZnO/GaN interface than that at ZnO/MgO/c-sapphire interfaces.
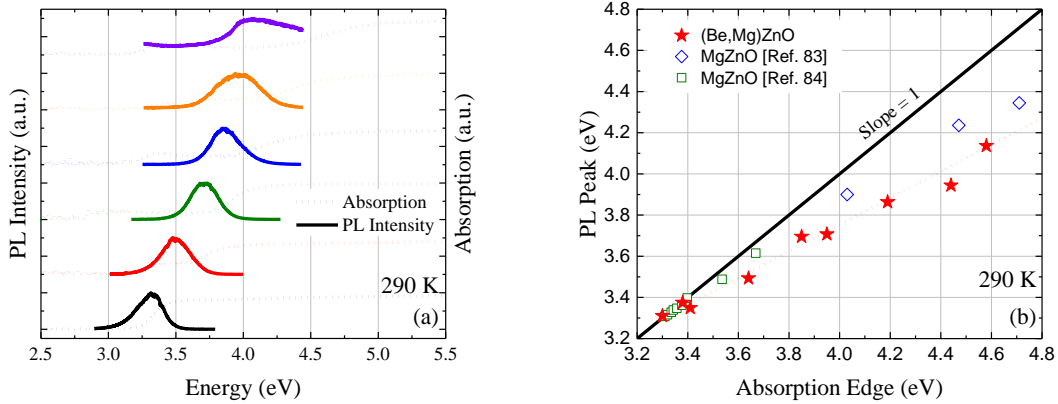
Figure 26. (a) Room temperature photoluminescence and absorption spectra and (b) comparison between PL peak position and absorption edge for O-polar BeMgZnO samples. MgZnO literature data is from Ref. 83,84.

To get deeper understanding of radiative and nonradiative processes in BeMgZnO samples, the dependence of the time-integrated PL intensity and PL decay time on temperature is investigated and are shown in Figure 27. The changes in PL intensity are concurrent with change in PL spectrum and blue shift of the PL peak position (see Figure 27b).
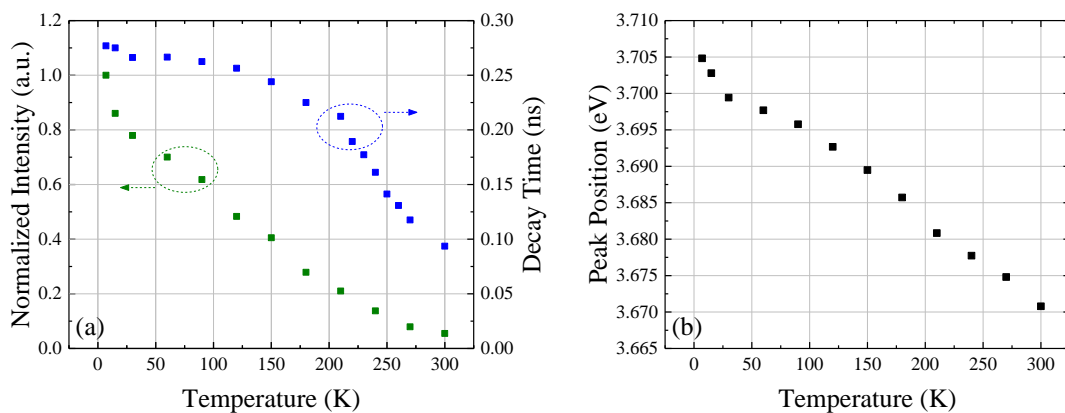
Figure 27. Temperature dependence of (a) the time-integrated PL intensity and (b) PL decay time and quaternary energy peak position of sample II.

To extract the radiative and nonradiative decay times, the measurement of external quantum efficiency was performed on sample II at 15K using the calibration sample with the known external quantum efficiency. On the other hand, efficiency can be expressed as the ratio of the radiative recombination rate to the total recombination rate.

$$\frac{I(T)}{I(15K)\cdot 100} = \frac{1/\tau_r}{1/\tau_{PL}} = \frac{1}{1+\tau_r/\tau_{nr}}$$

(8)

where τ_r and τ_{nr} are the temperature dependent radiative and nonradiative decay times, respectively. The PL decay time, τ_{PL}, obtained from TRPL can be expressed in terms of radiative and nonradiative decay times as

$$\frac{1}{\tau_{PL}} = \frac{1}{\tau_r} + \frac{1}{\tau_{nr}}$$

(9)

Equations (8) and (9) can be solved for τ_r and τ_{nr} and the result of such calculation is shown in Figure 28. The use of different values of quantum efficiency would change τ_{nr} and only vertically shift τ_r on the logarithmic plot without changing its shape. Based on our assumption of 1% quantum efficiency at low temperature, the nonradiative recombination channels dominate at all temperatures.
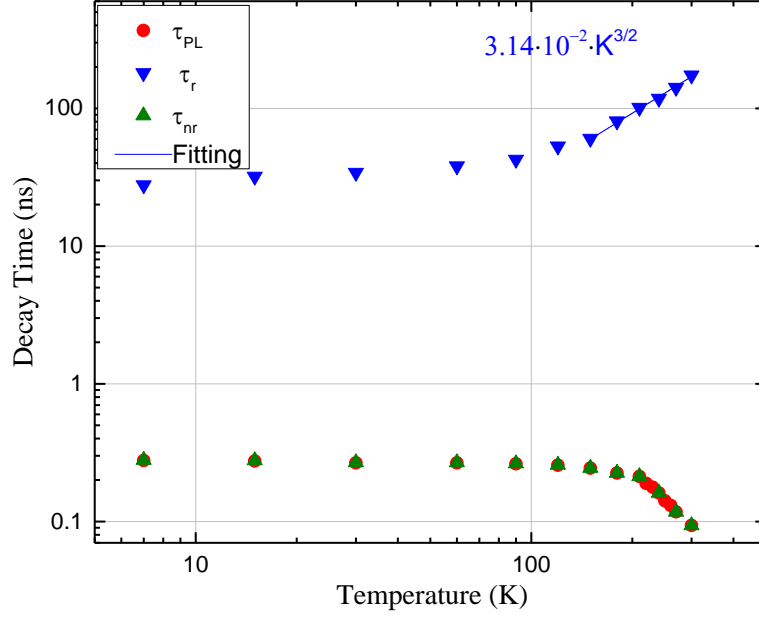
Figure 28. PL (τ_{PL}), radiative (τ_r) and nonradiative (τ_{nr}) decay times of sample II.

Rosales et al.[85] have shown that temperature dependence of radiative lifetime can be expressed as

$$\tau_r = \tau_0 T^{N/2} \tag{10}$$

where τ_0 is a characteristic constant. and N is the dimensionality of the material, which is N=3 for bulk. The obtained fitting parameters are τ_0=0.33±0.1 ps and N/2=1.50±0.05 which confirms that the BeMgZnO thin films are bulk-like. The effect of excitation intensity on the measured dimensionality and degree of localization require further investigation. Additionally, the study will be extended to a variety of BeMgZnO think films with different Be and Mg content and growth conditions.

The carrier localization and potential fluctuations in the barrier BeMgZnO may play a vital role on the performance of BeMgZnO/ZnO heterostructures. Such investigations have not yet been performed. As was mentioned in equation (10) the radiative decay time can be expressed as

$\tau_r = \tau_0 T^{N/2}$. We used an assumption of 1% quantum efficiency at low temperature. However, with the exact value of internal quantum efficiency and PL decay time it is possible to deconvolute the PL decay time and determine effects of radiative and nonradiative components. To extract the exact value of the nonradiative component we will compare PL intensity of the barrier layer with a sample with known quantum efficiency. After that, the temperature dependence of the nonradiative decay time can be fitted by[85]

$$\tau_{nr} = \tau_1 \exp\left(\frac{E_a}{k_B T}\right) = \tau_1 \exp\left(\frac{T_a}{T}\right) \tag{11}$$

where E_a (T_a) is the activation energy (temperature).

The knowledge of the fitting parameters such as τ_1, τ_0 and T_a and the dependence of photoluminescence intensity with temperature can be fitted by[85]

$$I(T) \propto \frac{1}{1 + \dfrac{\tau_0}{\tau_1} T^{N/2} \exp\left(-\dfrac{T_a}{T}\right)} \tag{12}$$

Figure 29 shows the behavior of time integrated PL with temperature as well as the fit obtained Equation (12). The higher the activation energy, the more stable PL intensity is with temperature. Sample B shows high activation energy and stable PL intensity up to 200K. High E_a is well correlated with high Δ_0 (268 meV for sample II).

$$I(T) \propto \frac{B_1}{1 + B_2 T^{3/2} \exp\left(-\dfrac{T_a}{T}\right)}$$

$$B_1 = 0.89 \, \text{a.u.}$$

$$B_2 = 0.81 \, \text{K}^{-3/2}$$

$$T_a = 1696 \, \text{K} \quad \rightarrow \quad E_a = 0.14 \, \text{eV}$$
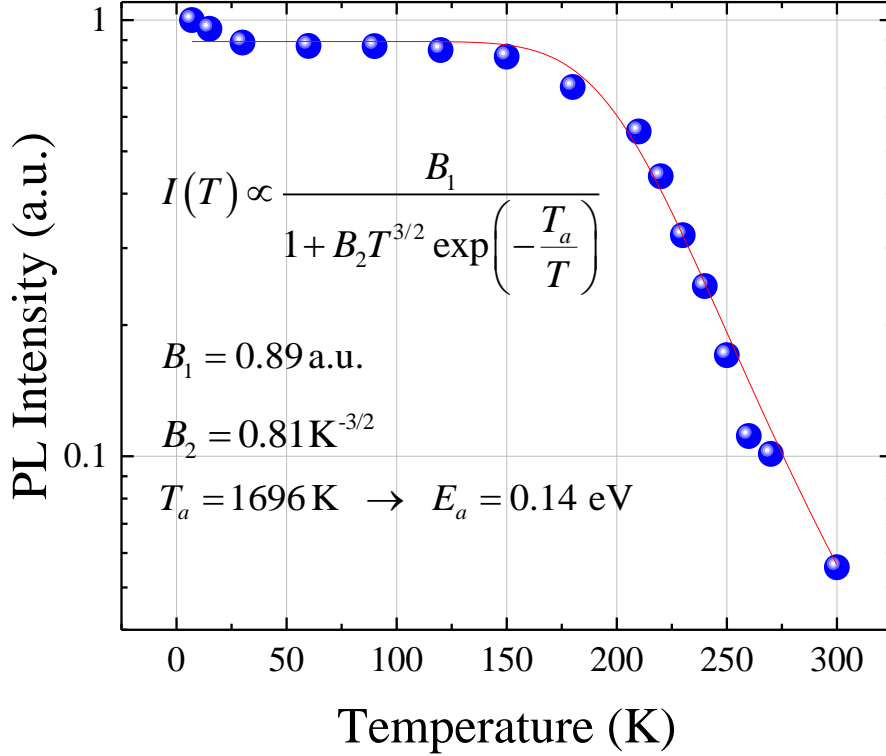
Figure 29. Time integrated PL intensity of sample II. Solid line and coefficients are obtained using the fit with Equation (12).

In conclusion, time-resolved PL measurements reveal an increase in the degree of localization depth and temporal redshift with the increase in $r_{Mg/Be}$ content ratio in BeMgZnO samples grown on GaN which are attributed to mutual compensation effects of Be and Mg to reduce formation energy and strain The localization depths (temporal redshift) are 46 meV (10 meV), 98 meV (8 meV), 173 meV (42 meV), and 268 meV (55 meV) for $Be_{0.03}Mg_{0.18}Zn_{0.79}O$, $Be_{0.04}Mg_{0.17}Zn_{0.79}O$, $Be_{0.10}Mg_{0.25}Zn_{0.65}O$ and $Be_{0.11}Mg_{0.15}Zn_{0.74}O$, respectively. PL transients indicate that emission at low temperature is dominated by recombination of localized excitons, which exhibit decay times as long as $\tau_1 = 0.485$ ns at PL peak position. The S-shaped behavior of PL peak with change in temperature was observed for the quaternary alloy $Be_{0.04}Mg_{0.17}Zn_{0.79}O$ with localization depth $\Delta_0 = 98$ meV and Mg/Be=4.3; the degree of localization σ was determined

to be 22 meV. The carriers were found to be localized even above room temperature in $Be_{0.11}Mg_{0.15}Zn_{0.74}O$ with Mg/Be =1.4. The Varshni's coefficients for the latter sample are $\alpha = 1.2 \cdot 10^{-4}$ eV/K and $\beta = 37\,K$. The inverse proportionality of low temperature PL intensity and $r_{Mg/Be}$ content ratio was observed. However, at room temperature this proportionality was broken. With reducing $r_{Mg/Be}$, the compensation effects between Mg and Be weaken, which increase both number of defects as well as strain induced localization Δ_0. For room temperature performance, higher degree of localization is necessary. Since localization depth and defect density are somewhat coupled, there exists an optimum $r_{Mg/Be}$ content ratio. At room temperature, the optimum $r_{Mg/Be}$ ratio lay around 2.5. The radiative lifetime exhibited temperature dependence of $\tau_r \propto T^{N/2}$ with dimensionality N = 3 corresponding to bulk-like behavior at 65 Wcm^{-2} excitation intensity.

Chapter 4. Metal-semiconductor contacts to ZnO and BeMgZnO

For the fabrication of BeMgZnO/ZnO HFET, it is necessary to achieve a large Schottky barrier height at the gate metal contact and low specific contact resistivity at source and drain ohmic contacts. Therefore, the formation of Schottky and ohmic contacts to ZnO were investigated. First, theoretical backgrounds of the formation of Schottky contact and effects of surface states will be discussed, then experimental results of the contacts will be presented.

4.1. Schottky Contacts

4.1.1. Theoretical Background

First, we will consider an ideal case for a metal-semiconductor contact (MSC) without surface states or interface insulator layer. Figure 30a shows the band diagram of a metal with work function φ_m and n-type semiconductor with work function φ_s and electron affinity χ. Figure 30b shows the ideal metal-semiconductor contact with no interface states and no interface insulator layer. The Fermi levels are aligned. Based on the energy conservation the barrier for electrons traveling from metal to semiconductor can be written as:

$$q\phi_{Bn0} = q\phi_m - q\chi \ (n-type)$$

(13)

64
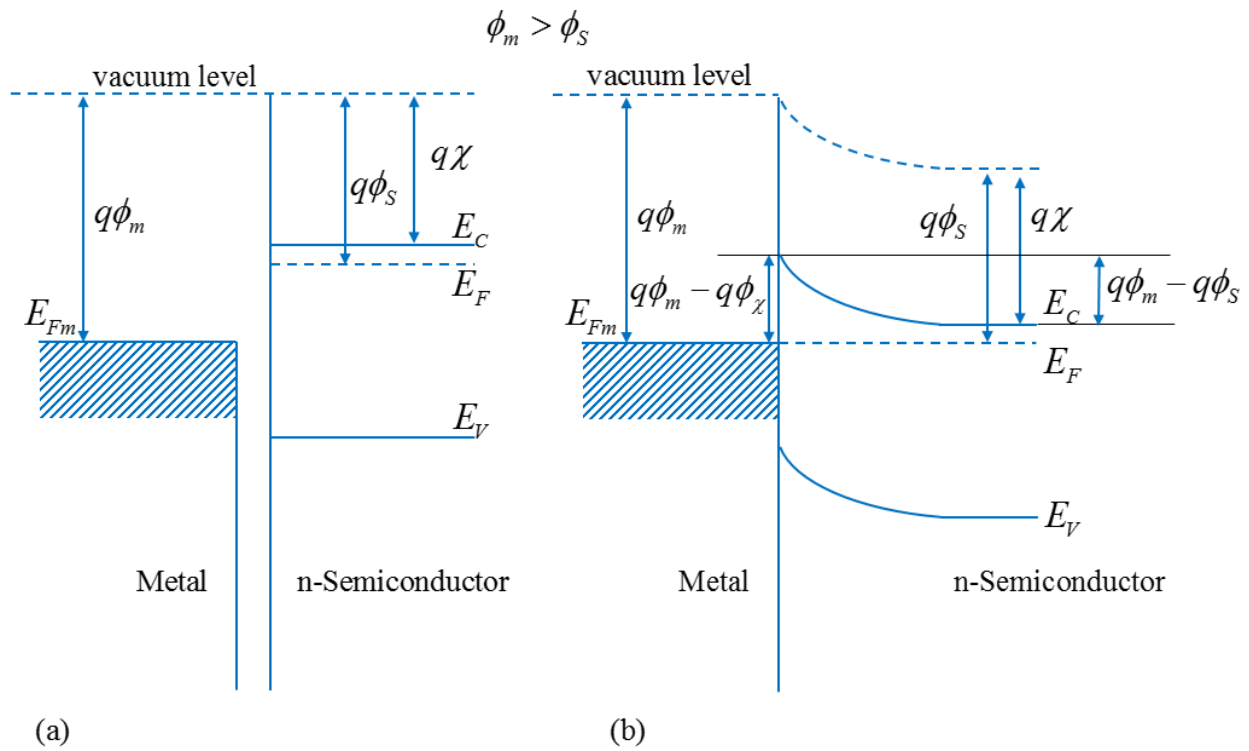
Figure 30. A metal n-type semiconductor pair before (a) and after (b) contact with no surface/interface states. The metal work function is greater than that for the semiconductor ($\varphi_m > \varphi_s$).

Based on equation (13), in order to achieve rectifying behavior with MSC, a metal with $\varphi_m > \varphi_s$ must be chosen and higher φ_m will result in higher Schottky barrier height $q\phi_B$. Figure 31 shows collection of metals with their free energy of formation per oxygen atom and work function.
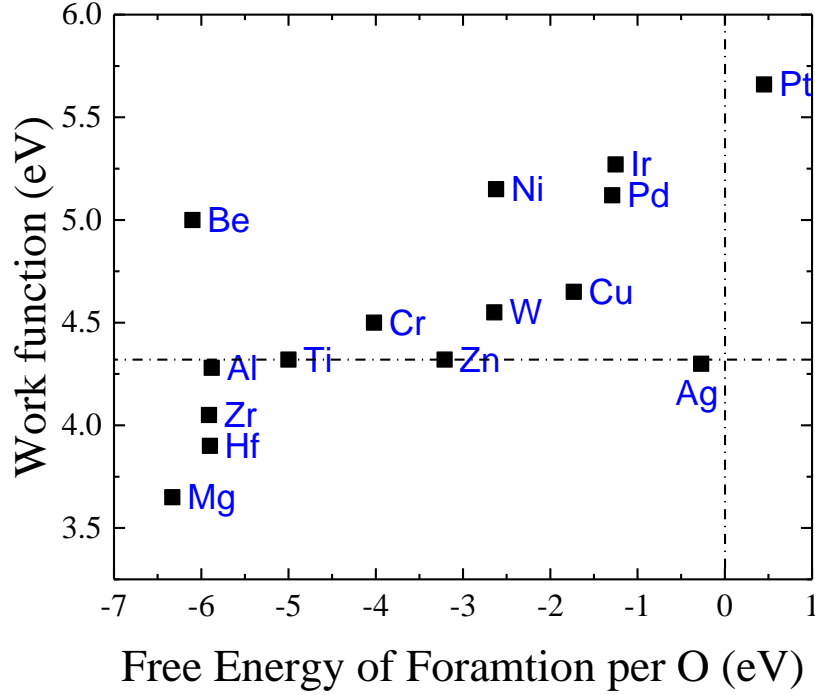
Figure 31. Free energy of formation per Oxygen atom for variety of metals as a function of metal workfunction.

However, in practice simple equation (13) is rarely realized due to presence of surface contamination and defects that introduce surface states and can potentially even pin the position of Fermi level to the level of the defect. The interface states are usually discussed on the basis of two assumptions: (1) interfacial layer of atomic thickness which will be transparent to electrons but can withstand potential across it, and (2) the interface states are the property of semiconductor and are independent of the metal. More detailed diagram is shown in Figure 32. We will consider a semiconductor with donor-like interface traps whose density is D_{it} states/cm²-eV. This is the case of ZnO surface which exhibits downward surface band banding due to presence of oxygen vacancies. The interface-trap charge density Q_{ss} is therefore positive and expressed as:

$$Q_{ss} = qD_{it}\left(E_g - q\phi_0 - q\phi_{Bn0}\right)$$

(14)
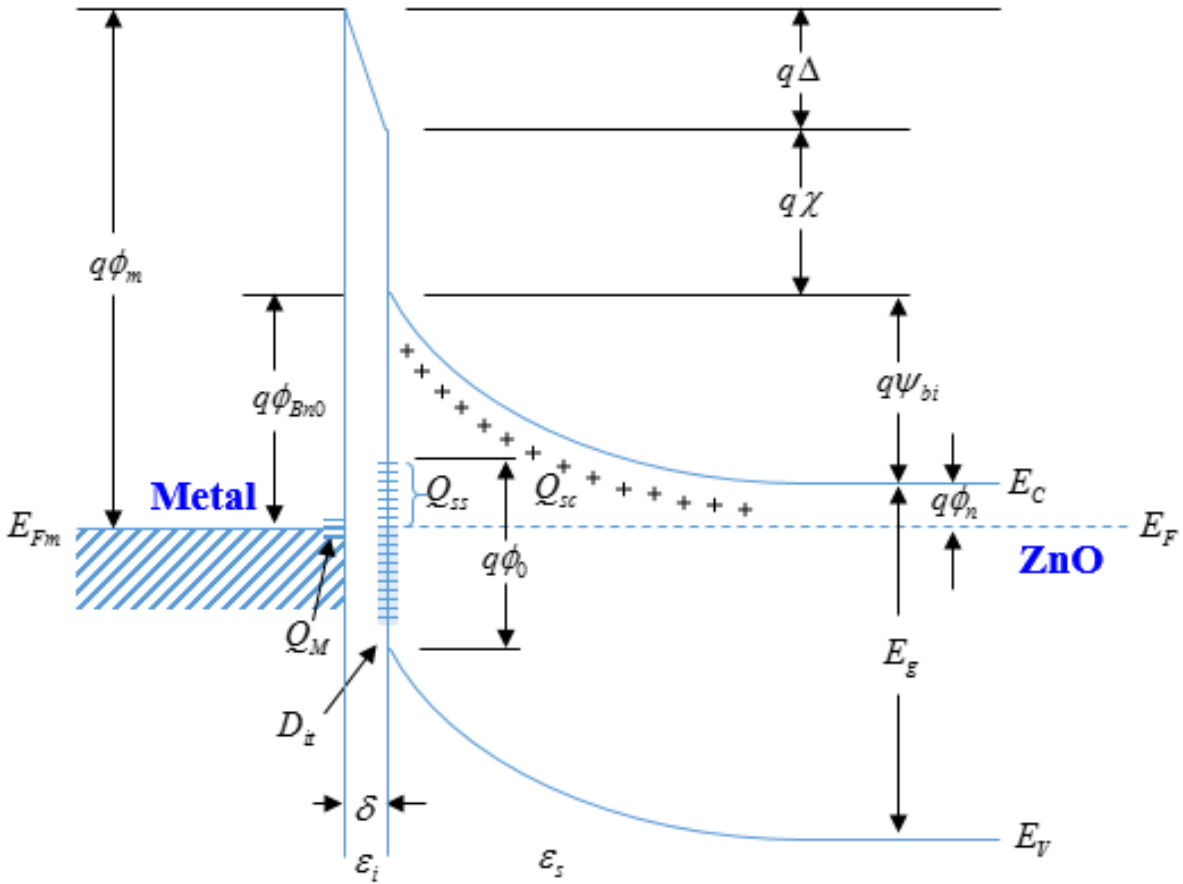
Figure 32. Detailed energy-band diagram of a metal-n-semiconductor contact with an interfacial layer (vacuum) of the order of atomic distance.

Additionally, the space charge Q_{sc} is formed and given as:

$$Q_{sc} = qN_DW_D = \sqrt{2q\varepsilon_s N_D \left(\phi_{Bn0} - \phi_n - \frac{kT}{q} \right)} \qquad (15)$$

where N_D is donor concentration, W_D is the depletion width. An equal and opposite to the total charge on the semiconductor surface will be formed on the metal surface.

$$Q_M = -\left(Q_{ss} + Q_{sc} \right) \qquad (16)$$

67

The potential Δ across the interfacial layer can be obtained by applying gauss's law.

$$\Delta = -\frac{\delta Q_M}{\varepsilon_i}$$

(17)

where Q_M is the charge on the metal side and ε_i is the permittivity of the interfacial layer and δ is its thickness. From the energy diagram, Δ can be seen as the correction factor to simple equation (13).

$$\Delta = \phi_m - \left(\chi + \phi_{Bn0} \right)$$

(18)

By combining equation (17) and equation (18) we obtain

$$\phi_m - \left(\chi + \phi_{Bn0} \right) = \sqrt{\frac{2q\varepsilon_s N_D \delta^2}{\varepsilon_i^2} \left(\phi_{Bn0} - \phi_n - \frac{kT}{q} \right)} - \frac{qD_{it}\delta}{\varepsilon_i} \left(E_g - q\phi_0 - q\phi_{Bn0} \right)$$

(19)

Equation (19) can be solved for ϕ_{Bn0}.

To simplify the equation, we can introduce quantities:

$$c_1 \equiv \frac{2q\varepsilon_s N_D \delta^2}{\varepsilon_i^2};$$

$$c_2 \equiv \frac{\varepsilon_i}{\varepsilon_i + q^2 \delta D_{it}}$$

(20)

Equation (19) reduces to:

$$\phi_{Bn0} = \left(\phi_m - \chi \right) - \sqrt{c_1 \left(\phi_{Bn0} - \phi_n - \frac{kT}{q} \right)} + \frac{qD_{it}\delta}{\varepsilon_i} \left(E_g - q\phi_0 - q\phi_{Bn0} \right) \rightarrow$$

$$\rightarrow \phi_{Bn0} + \frac{q^2 D_{it}\delta}{\varepsilon_i} \phi_{Bn0} = \left(\phi_m - \chi \right) - \sqrt{c_1 \left(\phi_{Bn0} - \phi_n - \frac{kT}{q} \right)} + \left(\frac{1}{c_2} - 1 \right) \left(\frac{E_g}{q} - \phi_0 \right) \rightarrow$$

(21)

$$\rightarrow \phi_{Bn0} = c_2 \left(\phi_m - \chi \right) - c_2 \sqrt{c_1 \left(\phi_{Bn0} - \phi_n - \frac{kT}{q} \right)} + \left(1 - c_2 \right) \left(\frac{E_g}{q} - \phi_0 \right)$$

Considering the ZnO case, we assume $\varepsilon_s(0) = 8\varepsilon_0$, $\varepsilon_i = \varepsilon_0$, and $N_D = 10^{18}\, cm^{-3}$, $\delta = 1 \cdot 10^{-8}\, cm$. The resulted $\sqrt{c_1} = 0.05\, V$ is small, and therefore we can neglect the square root term in equation (21).

$$\phi_{Bn0} = c_2\left(\phi_m - \chi\right) + \left(1 - c_2\right)\left(\frac{E_g}{q} - \phi_0\right) \equiv c_2\phi_m + c_3 \tag{22}$$

The interface properties can be expressed in terms of c2 and c3:

$$\phi_0 = \frac{E_g}{q} - \frac{c_2\chi + c_3}{1 - c_2} \tag{23}$$

$$D_{it} = \frac{(1 - c_2)\varepsilon_i}{c_2\delta q^2} \tag{24}$$

Two limiting cases are possible

1. When $D_{it} \to \infty$, then $c_2 \to 0$ and the Fermi level at the surface is pinned to the level of surface states. The barrier height is independent of the metal work function.

    $$q\phi_{Bn0} = E_g - q\phi_0 \tag{25}$$

2. When $D_{it} \to 0$, then $c_2 \to 1$ and the simplified equation (13) is true

    $$q\phi_{Bn0} = q\left(\phi_m - \chi\right) \tag{26}$$

Figure 33 shows the result for achieved Schottky barrier height to ZnO using different metal options. The line with slope = 1 indicates the expected barrier height based on the Schottky-Mott model, equation (13). The spread in the achieved results for each metal is high, and suggests that the surface of ZnO plays an important role in the formation of Schottky barrier height. Moreover, most results lay within 0.6-0.8 eV, which coincide with the level of oxygen vacancy $V_O^{(+2,0)}$ and result in $D_{it} \to 0$ for such samples.
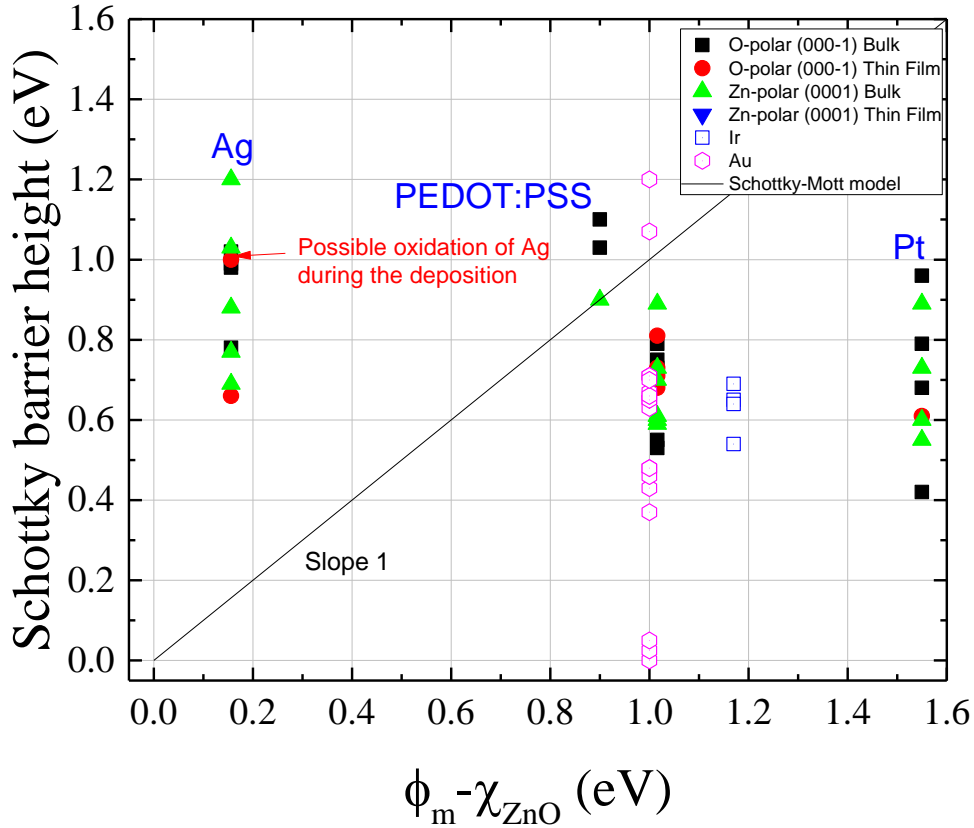
Figure 33. Schottky barrier height ϕ_B as a function of difference between metal work function ϕ_m and electron affinity χ_{ZnO} of ZnO measured based on I-V characteristics of the results available in literature.

4.1.2. Surface preparation

Strong downward surface band banding is observed for ZnO surface which results in increased surface carrier concentration. Heinhold et al. [86] reported surface bandbandign of -0.2 eV and -0.5 eV for O-polar and Zn-polar ZnO, respectively, deducted using synchrotron x-ray photoelectron spectroscopy on the polar surface of ZnO single crystal. For both surfaces the near surface carrier concentration differs by orders of magnitude from the bulk carrier concentration.[87]

There are variety of methods reported in the literature that are used to prepare the surface of ZnO for better Schottky contact fabrication, such as HCl etching (and other acids), Ar physical

etching, H_2O_2 treatment, UV Ozone and O-plasma (or mixture with He) exposure. The first two are only physical etching of the top layer; the peroxide may additionally eliminate oxygen vacancies that serve as donors on the surface of ZnO; UV Ozone and O-plasma are used only to decrease surface conductivity and do not etch ZnO.

For nonreactive (i.e. no active component like Oxygen is present) metal deposition technique it is necessary to reduce upward surface band banding by applying proper surface treatment prior to metal deposition. Hydrogen peroxide surface treatment is also well regarded method to improve Schottky diode performance. [88–90] Schifano et al.[91] reported fabrication of Schottky diode based on hydrothermally grown single crystal ZnO with Pd as the Schottky metal where samples are cleaned with H_2O_2 for 15 min; no rectifying behavior is observed for solvent cleaned sample. The reported H_2O_2 surface treatments usually include boiling in the non-diluted peroxide (majority of papers do not specify exact cleaning procedure). Such procedure will etch thin films with thickness in the range of microns and therefore, cannot be applied for heterostructure FET. The necessity of such strong cleaning is not discussed in the literature. Nevertheless, H_2O_2 treatment shows improved performance in comparison to HCl or H_3PO_4 etching prior metal deposition (0.7eV for H_2O_2 and Ohmic for HCl).[92]

There are few works showing results for plasma treated samples vs. not plasma treated samples. Mosbacker et al.[93] reported IV characteristics for bulk ZnO samples before and after plasma treatment using Pt and Pd metals. Without plasma treatment, contacts are Ohmic. Despite clear effect of the oxygen plasma, the achieved results of φ_b=0.5 eV are dramatically below the best reported values (see Figure 32).

Muller et al.[94] reported on fabricated Schottky contacts (SC) with or without presence of a reactive component (O or Ar/O_2 atmosphere) during the deposition process. It was found that

devices fabricated with deposition method containing reactive component (reactive E-PLD, reactive sputtering etc.) show rectifying behavior even without any surface treatment. On the other hand, devices fabricated with a deposition technique without a reactive component (thermal evaporation, e-beam evaporation etc.) shows no or small rectifying behavior and most of the reported result are in the vicinity of φ_b=0.5-0.9 eV (in many cases despite variety of different surface treatments). It is suggested that such devices exhibit Fermi level pinning to the surface states level of oxygen vacancy at 0.6-0.7 eV. Additionally, Schottky barrier height above 0.7eV is achievable even without any surface treatment with deposition containing reactive component.[94] Allen et al.[95] attributed this behavior to the partial oxidation of the Schottky contact metal made of Pd, Pt or Ir and the compensation of the surface V_O and reduction of the surface carrier concentration and thus surface band banding due to higher reduction potential of Zinc in comparison to the noble metals. Best reported values for Ag, Pd and Pt are achieved with reactively deposited contacts.

Usually Schottky contacts are achieved by depositing a high work function metal such as Pd, Pt, Ir etc. (see Figure 31). In contrast, Ag has low work function of 4.3 eV. Despite that, devices fabricated with Ag metal can show rectifying behavior. This is due to interface silver oxide layer that is formed from partial oxidation of Ag with Oxygen from ZnO matrix. The formed oxide layer is transparent for electrons and have higher work function in comparison to Ag. Raju et al.[96] reported ~5.55eV work function for PLD grown AgO which is 1.3 eV higher than of Ag (4.26 eV). Silver oxidation with oxygen from ZnO must create high concentration of oxygen vacancies and therefore donors on the interface. It may be the case that there is a competition between the increase in number of oxygen vacancies (expected to hurt the Schottky performance) and the formation of

silver oxide with higher work function than Ag (expected to benefit the Schottky performance) and overall the latter one wins. This consideration requires more detailed investigation.

Allen et al.[97] reported Schottky barrier height of 1.02 eV and 0.88 eV for Zn-polar and O-polar Melt grown ZnO, respectively (n=4E16 cm^{-3}, 230 cm^2/Vs) with ideality factor n=1.1-1.2 using thermally evaporated Ag metal with similar results for RF sputtered Ag$_2$O. (no serial resistance was reported to determine the conductivity of the sputtered oxide). Even higher barrier heights, ϕ_b=1.2eV were reported by Allen et al.[98] on Zn-polar bulk ZnO samples (n=4E16 cm^{-3}, 230 cm^2/Vs) with nearly ideal Schottky diodes, ideality factor n=1.03 with silver oxide Schottky contact deposited with Ag target in Ar/O$_2$ plasma. Martin Allen[99] commented that such silver oxide films were highly silver rich (90-96% silver by atomic composition) and had low lateral conductivity and required capping metal layer (30nm Pt was used). Nearly ideal behavior at room temperature and above and non-ideal behavior at low temperatures was observed.

4.1.3. Experimental Procedures

There is a discrepancy in the literature regarding optimum surface treatment that has to be addressed. The most promising candidates to achieve reproducible high Schottky barrier are silver due to high electron affinity of silver oxide that can be formed on the interface after the metal deposition and platinum due to its high metal work function. Zn-polar and O-polar MBE grown ZnO layers were used for investigation of SC. The photolithography process was used to define planar circular SCs with diameter of 140 μm. The metal was deposited using electron beam evaporating system.

The Schottky barrier heights are calculated using thermionic emission theory can be expressed as:

$$I = I_0 \exp\left(\frac{q(V - IR_s)}{n k_B T}\right) \tag{27}$$

where V is applied voltage, R_s is serial resistance and n is ideality factor.

The saturation current is given by:

$$I_0 = A A^{**} T^2 \exp\left(-\frac{q\phi_B}{k_B T}\right) \tag{28}$$

where A is area of the contact and A^{**} is the effective Richardson constant.

4.2. Results and Discussion

4.2.1. Platinum Schottky Diode

O-polar P1 and Zn-polar P2 ZnO samples were used for the first Pt deposition. Both samples were cleaned with acetone, methanol solvents in ultrasonic bath for 3 min followed by thorough rinsing in DI water and drying with N_2 gun. To remove any possible water residue, samples were additionally dried on a hot plate at 110ºC for 3 min. The photolithography was performed with PR thickness of 1 µm. After PR development, each sample was diced into four pieces and exposed to different surface treatments with O-plasma and hydrogen peroxide:

- "Reference" – no additional cleaning to initial solvent cleaning;

- "Reactive" – O-plasma exposure at the 1st shelf (the highest etching rate of PR). O_2 flow was 50 sccm and plasma power 200W, exposure time 3 min. Such treatment removes ~500nm of PR (half)

- "Ashing" - O-plasma exposure with insulating glass plate under the sample. O_2 flow was 50 sccm and plasma power 200W, exposure time 3 min. Such treatment removes below 100nm of PR.

- "H_2O_2" – hydrogen peroxide treatment with 30% H_2O_2 mixture and DI water in the proportion of 1:30 (H_2O_2:H_2O) for 90s. Such treatment resulted in ~5nm ZnO removal on the dummy sample.

Surface treatment was followed by Pt(30nm)/Au(40nm) metal stack deposition. Sample properties and achieved results for Pt metal deposition are summarized in Table 8.

Table 8. Schottky contact fabrication results with Pt. Plasma power 200W, time 3 min, pressure 0.35 Torr.

Surface prep.	Thin Film Prop.	Fabrication comments	ϕ_b, eV	n	R_s, Ohm
P1, O-polar					
Reference Reactive Ashing H_2O_2	$n=5.1 \cdot 10^{16}$ cm^{-3} $\mu=80$ cm^{2}V^{-1}s^{-1}	Ohmic contact: Reactive O-plasma after lithography Annealed 500ºC 10s RTA N_2	Ohmic 0.4 0.4 Ohmic	4.01 3.92	1219 1305
P2, Zn-polar					
Reference Reactive Ashing H_2O_2	$n=2.5 \cdot 10^{17}$ cm^{-3} $\mu=109$ cm^{2}V^{-1}s^{-1}	Ohmic contact: Reactive O-plasma after lithography Annealed at 450ºC 10s RTA N_2	Ohmic Ohmic Ohmic Ohmic		

All fabricated Zn-polar samples show Ohmic behavior. For O-polar sample, only those exposed to O-plasma show small rectifying behavior with small ϕ_b of 0.4 eV and very high ideality factor. However, Pt had high metal work function (see Figure 31) and based on Schottky-Mott model should provide ϕ_b above 1eV. The resulted pure or no rectifying behavior with Pt/Au metal stack must originate from insufficient or improper surface treatment prior to metal deposition and require further optimization

4.2.1.1. Silver Schottky Diode

O-polar S1 and Zn-polar S2 and S3 ZnO samples were used for the g(200nm)/Au(30nm) deposition. Prior to PR coating, the samples were boiled in acetone and methanol for 10 min, each

step followed by thorough rinsing in DI water and drying with N_2 gun and on a hot plate at 110ºC for 3 min. The photolithography was performed with PR thickness of 1 μm. After PR development, each sample was diced into four pieces and exposed to different surface treatments. For Pt based SC only those that were exposed to O-plasma showed any rectifying behavior. Therefore, only plasma treatments will be explored for SCs with Ag:

#1 – 35W, O_2=40 ccm, p=0.312 Torr, 1 hour – low power is used with intention to eliminate possible energetic radicals that may damage the surface or re-sputter PR.

#2 – 200W, O_2=50 ccm, p=0.351 Torr, 3 min – the fastest recipe we can make to etch ~500nm of PR.

#3 – 35W, O_2=40 ccm, Ar=40ccm, p=0.312 Torr, 1 hour - exploring conditions similar to previously reported on O_2/He mixture

#4 – "Reference" – no additional cleaning.

Figure 34 shows I-V characteristics of the best Ag-metal Schottky diodes. For the fabricated samples Ag suffers from bad adhesion to ZnO. Degree of the adhesion is marked in Table 9, however the trend is unclear to me for this fabrication. Practically all reference samples (only solvent cleaning prior PR spinning) have Ag/Au metal stack lifted-off. Only for sample S2, few devices are available which are exhibiting no rectifying behavior. Ohmic behavior were also observed for Pt deposition for only solvent cleaned samples.
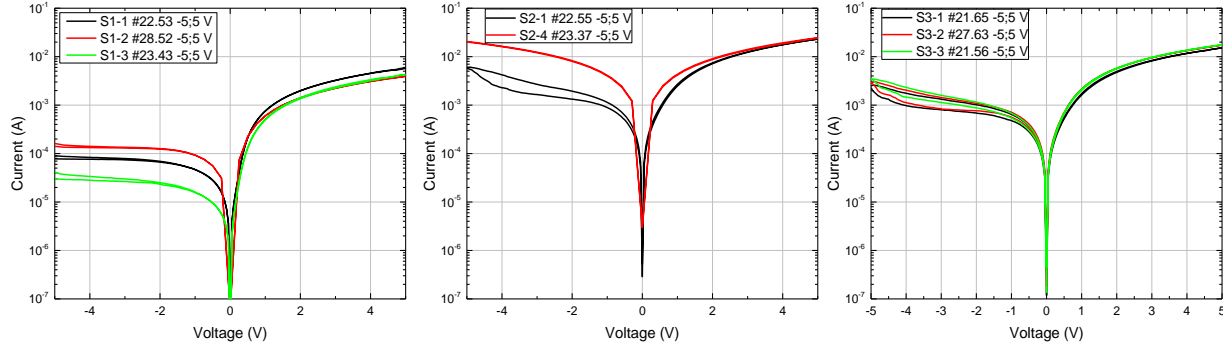
Figure 34. I-V characteristics of fabricated Schottky diodes. S1 is O-polar ZnO, S2 and S3 are Zn-polar

There exists variation across the sample. Figure 35 shows the variation in the I-V characteristics of O-polar S1-3 treated with 35W, O_2=40 ccm, Ar=40ccm, p=0.312 Torr, 1 h.

Table 9. Schottky contact fabrication results with Ag. All samples were boiled in Acetone and Methanol for 10 min prior PR spinning.

Surface preparation	Thin Films Prop.	ϕ_b, eV	n	Rs, Ohm
S1, O-polar				
#1 35W, O_2=40 ccm, p=0.312 Torr, 1 h		0.51	2.5	767
#2 200W, O_2=50 ccm, p=0.351 Torr, 3 min	n=$3\cdot10^{16}$ cm^{-3}	0.47	3.14	1163
#3 35W, O_2, Ar=40ccm, p=0.312 Torr, 1 h	μ=80 cm^{2}V^{-1}s^{-1}	0.54	3	1033
#4 Reference				
S2, Zn-polar				
#1 35W, O_2=40 ccm, p=0.312 Torr, 1 h		~0.37		
#2 200W, O_2=50 ccm, p=0.351 Torr, 3 min	n=$4\cdot10^{17}$ cm^{-3}	~0.37		
#3 35W, O_2, Ar=40ccm, p=0.312 Torr, 1 h	μ=70 cm^{2}V^{-1}s^{-1}	~0.37		
#4 Reference				
S3, Zn-polar				
#1 35W, O_2=40 ccm, p=0.312 Torr, 1 h		<0.36		
#2 200W, O_2=50 ccm, p=0.351 Torr, 3 min	n=$9.8\cdot1017$ cm-3	-		
#3 35W, O_2, Ar=40ccm, p=0.312 Torr, 1 h	μ=53 cm2V-1s	-		
#4 Reference		Ohmic		
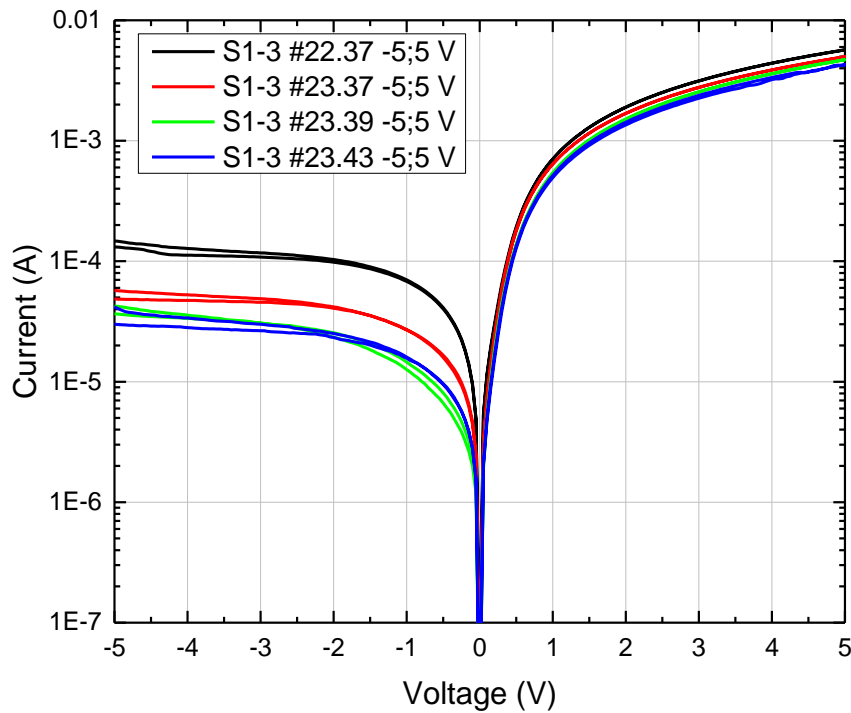
Figure 35. The variation in I-V characteristics for O-polar S1-3 treated with 35W, O_2=40 ccm, Ar=40ccm for 1 h. Devices are measured at different areas of the sample.

The best achieved on/off ratio for Ag metal Schottky diodes is ~10^2 for ±2V bias for S1-3 O-polar treated with 35W, O_2=40 ccm, Ar=40ccm, p=0.312 Torr, 1 h. No improvement of SCs was observed with aging (for our case 7 days) as was reported by Allen et al.[97] On the contrary, degradation of ϕ_b from 0.54 eV to 0.47eV and of n from 3 to 3.8 were observed.

Based on the literature review, both Ag and Pt metals can provide Schottky barrier height above 1eV under surface treatment. Improved rectifying behavior of Ag fabricated SCs in comparison to those fabricated with Pt may be attributed to introduction of solvent boiling prior to PR coating or smaller sensitivity of Ag metal to surface cleaning due to possible oxidation of Ag on the surface of ZnO.

Bad silver adhesion may be a result of a thick layer deposition (200nm). Further experiments with thinner metal layer (50nm) showed improvement in metal adhesion but didn't eliminate the problem completely. Pt provides much better adhesion to ZnO.

Our investigation shows that both Ag and Pt can produce ϕ_b>1 eV to ZnO with proper surface preparation. However, there are no reports of Schottky contacts using Pt metal based on ZnO thin films, which are expected to have higher density of defects in comparison to bulk layers. Ag, per say, should not provide rectifying behavior based on Schottky-Mott model. Due to lower formation energy of silver oxide in comparison to zinc oxide it is favorable for Ag to pull oxygen from zinc oxide. Silver oxide has 1.3 eV higher[96] work function then Ag which allows rectifying behavior. However, oxidation of Ag must generate oxygen vacancies on the interface and thus increase upward surface band bending which in turn will hurt rectifying characteristics. Furthermore, for non-reactive metal deposition, it is necessary to eliminate high upward surface band banding (high surface electron concentration)[94] by introducing H_2O_2 or O-plasma treatment that will lower concentration of high surface concentration of oxygen vacancies prior Schottky metal deposition. With proper surface treatment, it is expected to have higher Schottky barrier height with BeMgZnO in comparison to ZnO for the same metal. It is important to note that, despite seemingly better results for silver Schottky contacts, the surface preparation was different for silver and platinum depositions and thus two experiments and therefore results cannot be directly compared. Pt contacts can be improved with better surface preparation.

4.2.2. Schottky Contacts to BeMgZnO

The electron affinity of MgO and BeO is smaller than ZnO by about 1.5 eV and 2 eV, respectively (see Table 10). Based on the Schottky-Mott model that does not include the effect of surface states, i.e. $D_{it} \rightarrow 0$, it is expected to see an increase in ϕ_b in comparison to ZnO. Such improvement can only be expected for a defect free surface of quaternary BeMgZnO layer. Otherwise, the Fermi level can be pinned at the surface and Schottky barrier height would be independent of the metal work function. Mohonta et al.[92] reported ϕ_b=0.7 eV and n=3.37 with Pt metal to MOCVD grown c-plane $Mg_{0.1}ZnO$:N after hydrogen peroxide pre-treatment. IPA or HCl pre-treatment resulted in Ohmic behavior. Assuming the same electron affinity for wurtzite MgO as for rocksalt MgO and linear interpolation of MgO and ZnO values, we expect 0.2eV increase in ϕ_b for $Mg_{0.1}ZnO$ in comparison to ZnO. Lee et al.[100] reported 0.73 eV, 0.67 eV and 0.48 eV for Ag, Au and Pd, respectively, in case of PLD grown $Mg_{0.3}Zn_{0.7}O$ without any surface treatment; and Ohmic behavior to the reference ZnO layer for all three metals. Results from both reports suggest the presence of a high concentration of surface state and possible Fermi level pinning. Therefore, it is necessary to use proper surface cleaning or deposition technique to achieve high Schottky barrier to BeMgZnO predicted by Schottky-Mott model.

Table 10. Electron affinities of binary compounds of quaternary BeMgZnO

Material	Electron Affinity, eV
ZnO	4.5^{101}
	$4.2\text{-}4.35^{87}$
MgO (RS)	2.64^{102} (theory)
BeO	2.1^{102} (theory)

4.3. Ohmic Contacts

Ohmic contacts can be considered as contacts with zero or negligible Schottky barrier height and linear current-voltage characteristic. In order to achieve low voltage drop and thus low contact losses it is essential to use contacts with minimum specific contact resistivity. For the investigation of the specific contact resistivity, patterns used in transmission line method (TLM) were fabricated by conventional photolithography. The Ti(30nm)/Au(75nm) metal stack was evaporated followed by the lift-off process. Prior to lithography process different surface preparation conditions were investigated such as variations of solvent cleaning and exposure to O-plasma.

Figure 36 shows results for annealing experiments of O-polar ZnO that was treated with O-plasma after lithography process. It is important to note, that for data points prior annealing the spread originates from nonuniformity of the fabricated devices and includes all extreme points: edges and center of the sample. After this initial measurement the wafer was cut into smaller pieces to apply different annealing conditions. With increasing annealing temperature or time, we observe increase in sample conductivity (see Figure 36(b)). Black points correspond to the measurement done right after annealing (time=0) and time starts counting from the same annealing day. Based on right after annealing results one may judge that the best annealing conditions are 500ºC, 10s. However, these devices would show strong degradation with aging. Those that were not annealed at all or annealed at 450ºC for 10s are not Ohmic or Ohmic but highly resistive. Degradation decreases with increasing annealing temperature or time. The best annealing conditions with aging, in respect of lowest specific contact resistivity, are found to be in vicinity of 500ºC, 20s or 525ºC, 10s. This suggest that 500ºC, 10s does not provide sufficient metal alloying with ZnO and therefore shows degradation over time. On the other extreme annealing temperatures above 525ºC degrade the metal contact stack and provide lower specific contact resistivity but not degradation over time.
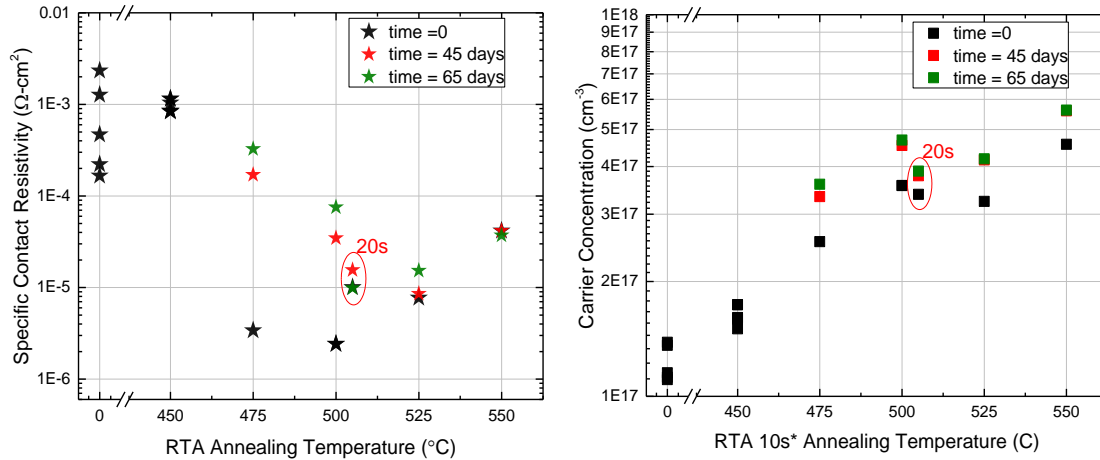
Figure 36. O-polar ZnO (reactive O-Plasma) annealed at different condition in RTA in N_2 environment. The devices that were measured at the time right after annealing and after aging are presented (for as grown sample Hall carrier concentration $1.3 \cdot 10^{17}$ cm^{-3} and mobility 62 cm^{2}V^{-1}s^{-1}).

O-polar sample cleaned in ultrasonic bath with solvents showed better performance in terms of achieved specific contact resistivity in comparison to those additionally cleaned with plasma. However, the spread in results should be eliminated. To do so, we investigated effect of boiling in solvents on the specific contact resistivity. All samples were subjected to boiling in Acetone, Methanol 10 min each step followed by thorough rinsing with deionized water and drying with N_2 gun. Subsequently samples were dried at 110ºC for 3min on a hot plate at atmospheric environment. Prior to boiling samples showed hydrophobicity while they became hydrophilic after boiling.

Figure 37 shows that most devices annealed at 525ºC for 5s have calculated carrier concentration that is slightly higher than of those annealed at 525ºC for 10s. I believe it is related to the degradation of the contacts. Further investigation of the degradation process is necessary as well as quantification of the measurement error. For the previous fabrication, we observed increase in the calculated carrier concentration with aging. From the fabrication with O-polar ZnO we found that devices annealed for 10s above 500C show small or no degradation with aging.

Therefore, the optimum annealing conditions were additionally investigated by annealing devices at 500ºC for 30 sec. and 525ºC for 5 sec. However, no improvement in specific contact resistivity was found in comparison to devices annealed at 500ºC 10s or 525ºC 5s.
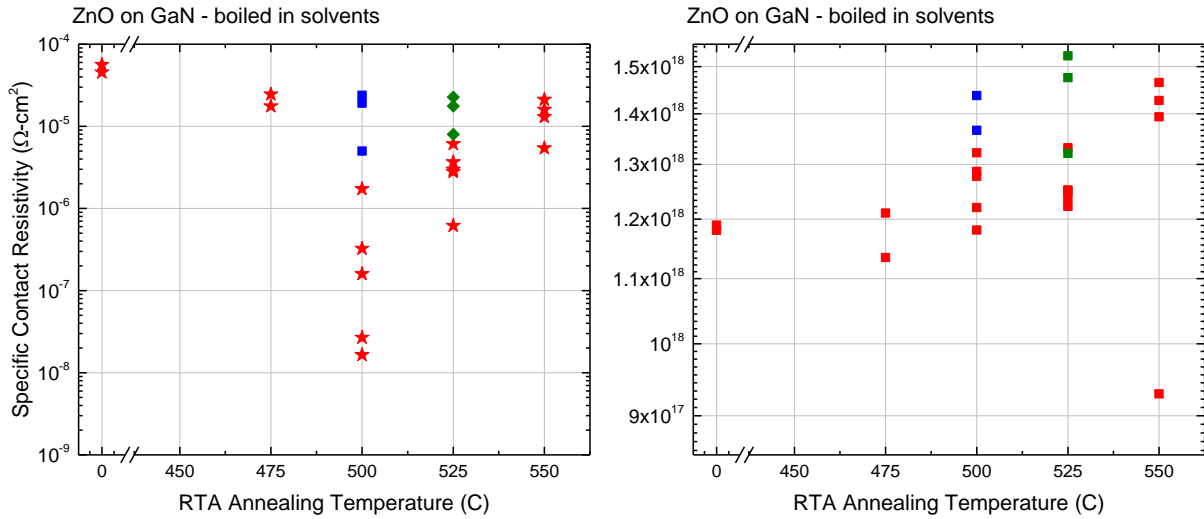
Figure 37. Zn-polar ZnO (solvent boiled) annealed at different condition in RTA in N_2 environment. Hall carrier concentration $1 \cdot 10^{18}$ cm^{-3} and mobility 53 cm^{2}V^{-1}s^{-1}

We observe that Zn-polar samples show strong dependence on the solvent cleaning procedure and require solvent boiling in order to achieve low specific contact resistivity. On the other hand, O-polar samples show weaker dependence on the variation of solvent cleaning. The best annealing conditions for O-polar and Zn-polar thin films with Ti/Au metal stack lay in vicinity of 500-525ºC annealed for 10s in RTA with N_2 environment. Figure 31. Free energy of formation per Oxygen atom for variety of metals as a function of metal workfunction. Figure 31 compares the achieved results to those available in literature.
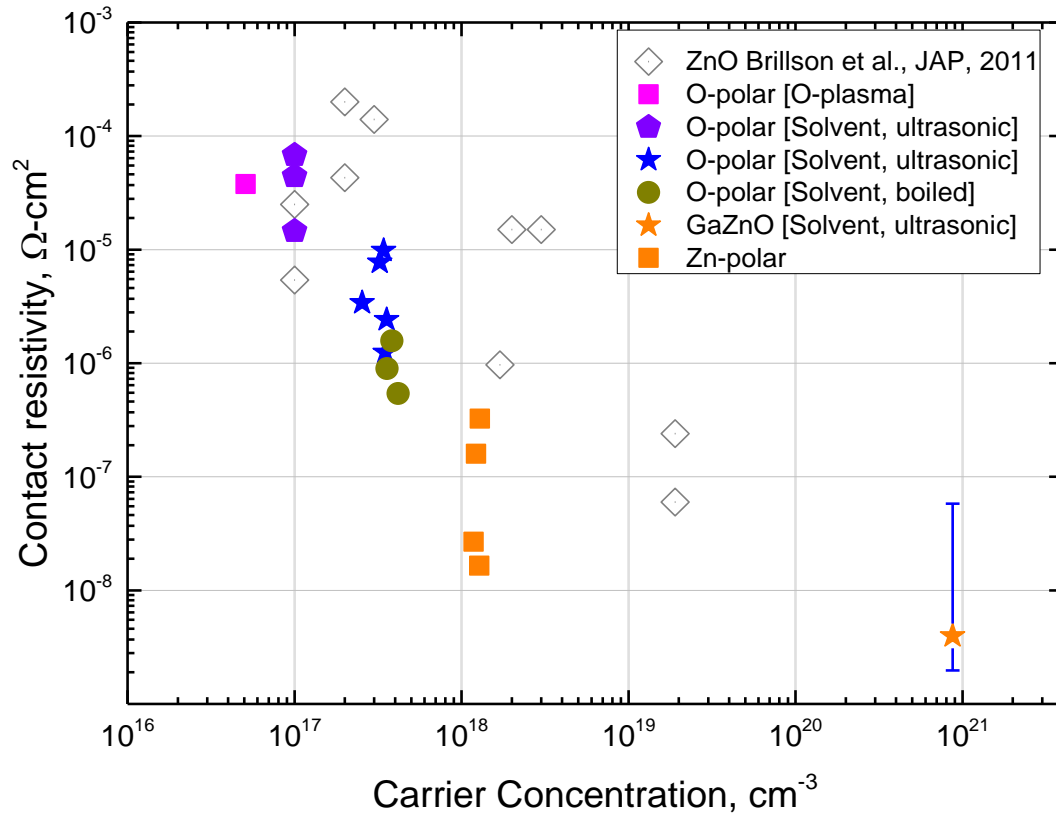
Figure 38. Specific contact resistivity dependence on the carrier concentration for discussed samples and samples available in the literature. The carrier concentration for annealed samples is calculated from TLM measurements using assumption that mobility does not change with annealing

Chapter 5. (Be,Mg)ZnO/ZnO Heterostructures with 2DEG

There is a considerable interest in the utilization of polarization field in polar oxide based heterostructure epitaxy. Remarkable mobilities have been reported for ZnMgO/ZnO heterostructures 2DEG. The highest reported low temperature 2DEG mobility for $Zn_{0.99}Mg_{0.01}O$/ZnO grown on bulk ZnO substrates is $7 \times 10^5 \, cm^2$/Vs, albeit at a low electron sheet density of $1.4 \times 10^{11} \, cm^{-2}$. However, for high power RF application carrier densities above $10^{13} \, cm^{-2}$ are necessary. It was shown in Section 2.2 that precise control over lattice parameters by tuning the quaternary composition would allow strain control in $Be_xMg_yZn_{1-x-y}O$/ZnO heterostructures with the possibility to achieve both compressive and tensile strain, where the latter supports formation of 2DEG at the interface with ZnO.

5.1. O-Polar ZnO/MgZnO Heterostructures with 2DEG

As an initial step to the fabrication of heterostructures with 2DEG using the BeMgZnO quaternary barrier, the use of the ternary MgZnO barrier was investigated. The O-polar ZnO/MgZnO/ZnO structures were grown on c-plane sapphire substrates by plasma-assisted molecular-beam epitaxy. First, a 2-nm thick MgO layer was deposited at a substrate temperature $T_S = 700$ºC followed by low-temperature ZnO deposited at $T_S = 300$ºC and annealed at 700ºC. Then a ZnO buffer layer and a MgZnO barrier were grown at 620ºC and 350ºC, respectively. The growth was finished by depositing a 40-to-50-nm thick ZnO channel layer at $T_S = 620$ºC. An oxygen plasma cell operating at 400 W served as a source of reactive oxygen while Zn and Mg were evaporated from K-cells. The oxygen pressure in the growth chamber was near 1.2×10^{-5} Torr. Mg fraction in the MgZnO barrier layers was varied by adjusting Zn and Mg cell temperatures.

Figure 39 shows the results of temperature dependent Hall measurement on ZnO/MgZnO/ZnO heterostructures and ZnO thin films. With the reduction in the sample

temperature the sheet carrier density reduces, indicating the presence of room temperature bulk conduction in the heterostructure samples. However, the results for ZnO thin film indicate that bulk carriers freeze out below 100K. This is consistent with saturation of hall carrier mobility below 100K (see Figure 39(b))
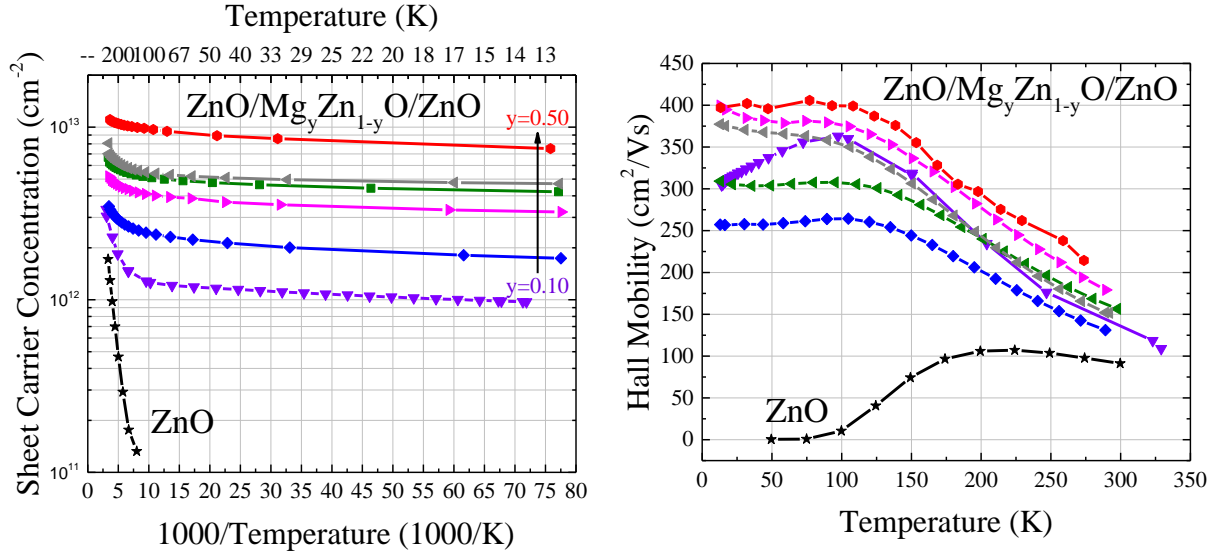
Figure 39. Dependance of a) sheet carrier density and b) Hall mobility on temperature of ZnO/MgZnO heterostructures and ZnO thin film (black curve)

Figure 40 shows the 2DEG carrier density dependence on the Mg content in O-polar ZnO/MgZnO/ZnO structures determined from Hall Measurement performed at 15 K where Mg content was deduced from the absorption edge. Higher Mg content results in higher spontaneous polarization which in turn allows higher 2DEG carrier density and near linear relationship on n_{2DEG} and Mg content is observed. Despite high Mg concentration in the MgZnO barrier layer, 2DEG carrier densities are limited below 10^{13} cm^{-2} for ZnO/MgZnO heterostructures.
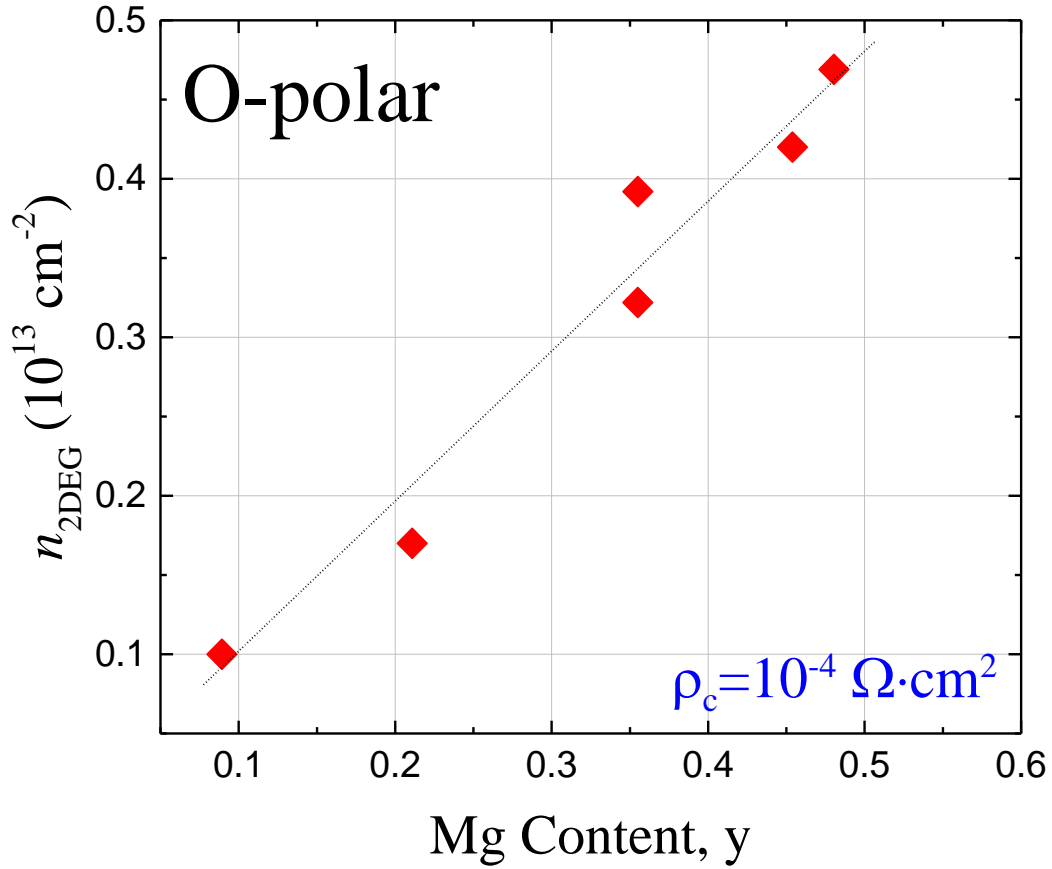
Figure 40. The 2DEG carrier density dependence on the Mg content in O-polar ZnO/MgZnO/ZnO structures determined from Hall Measurement performed at 15 K.

To get better insight into operation of HFET it is important to investigate electron transport at high electric fields, which is strongly controlled by longitudinal optical (LO) phonons in most polar materials. Strong LO-phonon-plasmon coupling is the condition for the ultrafast decay of hot phonons and the associated ultrafast relaxation of the hot electron energy. Indeed, a hot electron loses a considerable amount of energy when an LO phonon is emitted, but the energy loss is compensated when an LO-phonon is reabsorbed. The reabsorption rate is proportional to the occupancy of hot-phonon modes controlled by the lifetime of hot-phonon decay into acoustic phonons and other vibrations. Thus, the hot-phonon accumulation slows down the hot-electrons

energy dissipation, but the hot-phonon effect is reduced if plasmons assist the hot-phonon decay under near-resonance conditions.

We have studied hot electron effects in the $ZnO/Mg_{0.38}Zn_{0.62}O/ZnO$ heterostructures with two-dimensional electron gas (2DEG) channel subjected to pulsed electric field applied in the channel plane under near equilibrium thermal bath temperature. The microwave noise (at a frequency of 38.5 GHz) technique was applied to measure the hot-electron noise and estimate the electron energy relaxation time. The voltage pulse width was $\tau = 100$ ns, the gate pulse width was $\tau_{gate} = 50$ ns. The gate pulse was placed at the second half of the voltage pulse. The pulses were short enough to mitigate the self-heating effect. The dependence of the excess noise temperature on the electric field is shown in Figure 41. The dependence is interpreted in the following way. The electric field heats electron gas and causes the excess noise. The electron temperature T_e approximately equals the noise temperature T_n measured at the selected frequency in the range of white noise where other sources of noise do not manifest themselves. in the following way. The electric field heats electron gas and causes the excess noise. The electron temperature T_e approximately equals the noise temperature T_n measured at the selected frequency in the range of white noise where other sources of noise do not manifest themselves.
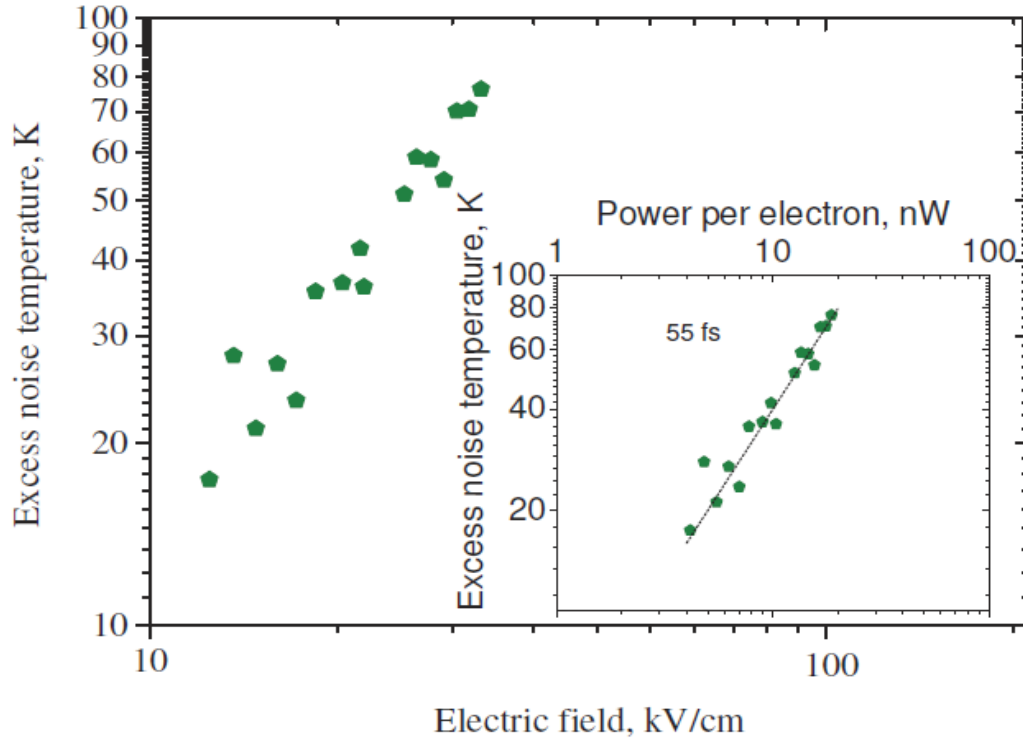
Figure 41. Dependence of the excess noise temperature on the electric field in the MgO/MgZnO/MgO structure with the 2DEG channel. Inset shows the dependence on the dissipated power per electron. Line corresponds to the constant electron energy relaxation time equal to 55 fs.

The electric power supplied to the electron gas P_s equals the dissipated power Pd because the voltage pulse is long enough for the strongly coupled subsystem of hot electrons and hot phonons to reach the quasi-steady state. The energy relaxation time approximation relates the electron gas temperature to the supplied power. The straight line in the inset of Figure 41 corresponds to the constant electron energy relaxation time. The self-heating effect is more easily avoided in 2DEG channels (100 ns pulses are short enough at the supplied power levels under discussion). The slope of the excess noise temperature versus the supplied power (inset in the Figure 41) is used to obtain the energy relaxation time. The value of $\tau_{en} = 55$fs is extracted.

The 2DEG density of ~5.5×10^{12} cm^{-2} was chosen to be near the possible LO-phonon–plasmon resonance where the electron energy relaxation is expected to be fast because of ultrafast decay of hot phonons. The results are compared with those for doped ZnO films. The hot-electron energy relaxation time of ~ 55 fs is extracted from the gated microwave noise measurements at the 2DEG density of ~5.5×10^{12} cm^{-2}. Figure 42 shows that this value is in between the resonance density reported for GaN 2DEG channels (~8x10^{12} cm^{-2}) 2DEG channels and InGaAs 2DEG channels (~2.5x10^{12} cm^{-2}).[103]
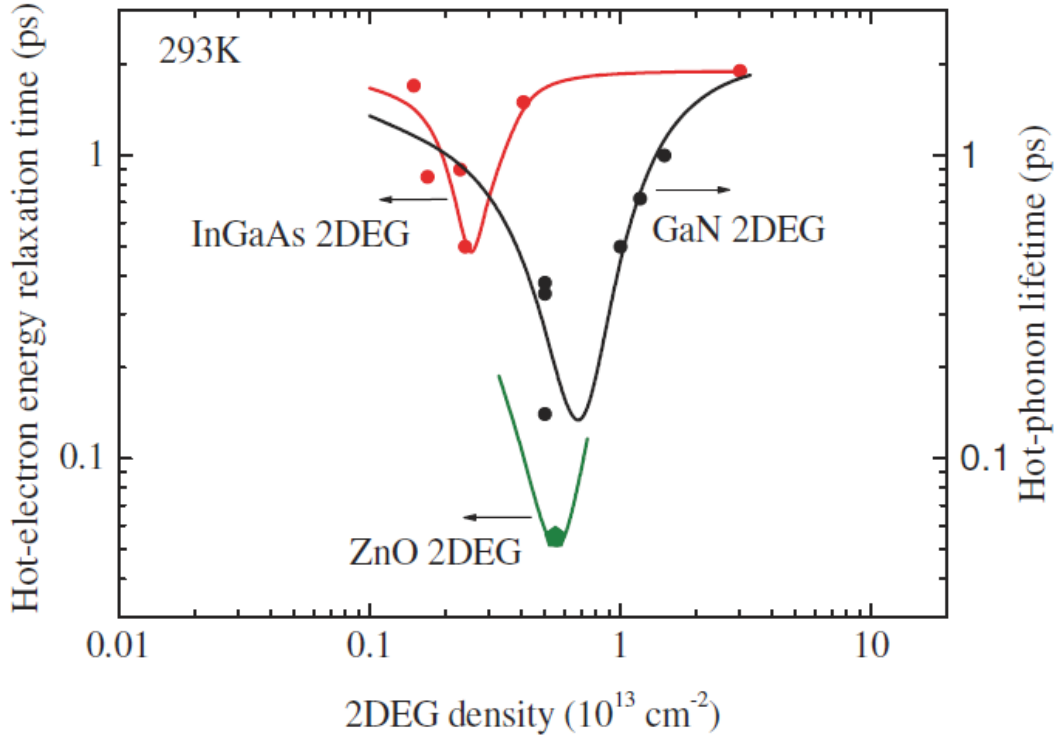
Figure 42. Illustration of the effect of LO-phonon–plasmon resonance for InGaAs 2DEG channels (red bullets) and GaN-based 2DEG channels (black bullets) together with the energy relaxation time for MgO/MgZnO/MgO 2DEG channel indicated by green pentagon. Solid curves guide the eye.

The ultrafast energy relaxation suggests that the power dissipation is enhanced by the LO-phonon–plasmon resonance. The results are in good agreement with those for doped ZnO films (Figure 43). However, it should be noted that, because of the limited 2DEG electron density in ZnO/MgZnO/ZnO heterostructures (our structure contains 38% Mg which is very close to a practical limit of 40% for Mg content), further studies of hot-electron effects in ZnO-based channels are required on ZnO/BeMgZnO/ZnO with higher 2DEG densities.
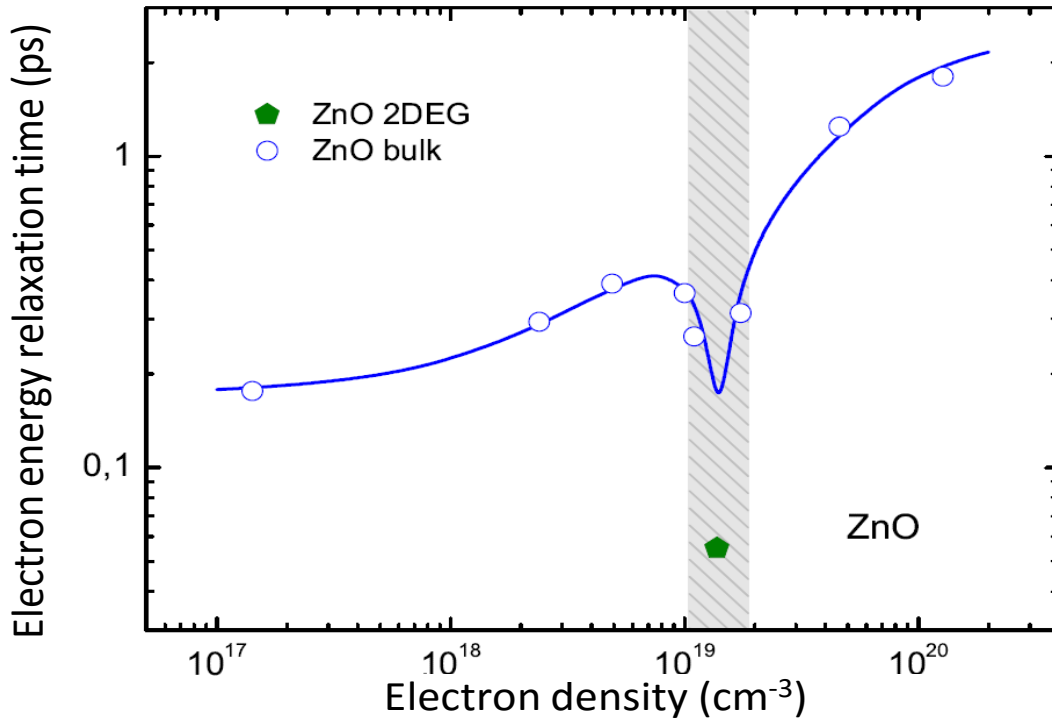
Figure 43. Energy relaxation time vs. the electron density in Ga-doped ZnO films (blue symbols) and the MgO/Mg$_{0.38}$ZnO/MgO 2DEG channel (green pentagon). Solid curve is to guide the eye. Dashed area indicates limits of an approximate conversion of the 2DEG density into the average 3DEG density for the MgO/Mg$_{0.38}$ZnO/MgO 2DEG channel.

For discussion of the resonance electron density (per unit volume) n_{res} let us make use of the expression for the infinite plasma:

$$n_{res} = \frac{E_{ph}^2}{\hbar} \frac{m\varepsilon}{e^2} \tag{29}$$

where E_{ph} is the LO-phonon energy, m is the electron effective mass, ε is the dielectric constant, e is the elementary charge and $\hbar$ is the reduced Planck constant. The effective electron mass and the LO-phonon energy are lower in arsenides as compared with oxides and nitrides. The fitted resonance density is in a qualitative agreement with Equation (11) though the comparison is not straightforward.

Because of large conduction band gap in MgZnO, the 2DEG is predominantly located in the top ZnO layer at the ZnO/MgZnO interface of the ZnO/MgZnO/ZnO structure. The and 92meV, respectively). Correspondingly, the 2DEG density in the ZnO channel (green pentagon, Figure 42) is lower as compared with the resonance density for GaN 2DEG layers (black bullets, Figure 42) in a qualitative agreement with Equation (11). The obtained energy relaxation time for the ZnO/MgZnO/ZnO is the shortest among the results presented in Fig. 3. This finding suggests that the density of 5.5×10^{12} cm^{-2} is close to the resonance density. In particular, the relaxation time (pentagon) is two times shorter than the LO-phonon lifetime in the GaN 2DEG channel (black bullets). Let us compare the result for the ZnO 2DEG channel with the recent results on doped ZnO films where the electron energy relaxation time was measured over a wide range of 3DEG densities (see Figure 43). The comparison is not straightforward because the 3DEG density is not constant in the 2DEG channel; it depends on the position in the transverse direction. The density profile resembles a rather asymmetrical Gauss function, and only some average 3DEG density can be specified for the 2DEG channel. We have used an approach where the thickness of the channel

is estimated as the width of the density profile at the Fermi level. Taking a realistic value of 4 nm, we get the average 3DEG density of $\sim 1.4 \times 10^{19}$ cm^{-3} for the 2DEG channel (Figure 43, green pentagon). A bit larger or smaller thickness would lead to the density values inside the shaded area. In this work we demonstrate that the hot electron energy relaxation is quite fast at the selected electron density. However, we do not know how sharp is the resonance. There is always a statistical variation in the electron density in the wafer. In particular, each open circle in the Figure 4 is an average over several devices having nominally the same electron density though the actual density differs. Because of the statistical averaging the fitting curve is less sharp than the resonance one. The ultrafast energy relaxation in the ZnO 2DEG channels is demonstrated for relatively low power per electron (the data are presented for ~ 4 nW per electron). The measurements above $\sim$ 20 nW are limited by onset of residual effect of the field on the channel resistance. The low field resistance measured after the short (100 ns) voltage pulse is higher as compared to its value before the pulse. The resistance slowly relaxes to its low-electric field value when the high field is switched off. Further comparing the data in Figure 4 we can notice that the electron energy relaxation in the 2DEG channel is faster than the energy relaxation obtained for the doped ZnO films at any electron density (blue circles). The energy relaxation time (blue circles) increases with the density except for the vicinity of the LO-phonon–plasmon resonance. The ultrafast energy relaxation is important for high-speed operation of power devices. Thus, high electron densities are of primary importance. The relaxation time of $\sim$55 fs at 5.5×10^{12} cm^{-2} is a good result. For comparison, the reported measurements yielded $\sim$200 fs at similar electron densities. The resonance helps to achieve the ultrafast relaxation at relatively high densities.

5.2. Strain Engineering for BeMgZnO/ZnO Heterostructure with 2DEG

In the BeO-MgO-ZnO system the knowledge of in-plane lattice parameters makes it possible to calculate the strain in ZnO-based heterostructures, including structures with 2DEG and quantum wells, which provides a guide for polarization charge engineering by tuning the sign and amount of piezoelectric polarization. The polarization charge is governed by the strain which sequentially depends on the lattice mismatch between the BeMgZnO and ZnO layers. Figure 44 represents strain in the quaternary $Be_xMg_yZn_{1-x-y}O$ thin film grown on a ZnO template ($a = 3.250$ Å) vs. Be and Mg content. The generic quadratic equation can produce better fit than Equation (1). Therefore, the result is obtained by fitting directly calculated values with a generic quadratic equation with ternary bowing parameters that are independent of each other. The in-plane lattice parameter can be expressed as:

$$a(x, y) = 3.284 - 0.468x - 0.094x^2 + 0.030y + 0.007y^2 \tag{30}$$

where a is expressed in Angstroms. The 0% strain line indicates the quaternary $Be_xMg_yZn_{1-x-y}O$ alloy that is lattice matched to ZnO which is described by the equation $y = 15.13x - 30.81x^2$. From Figure 44 it is clear that Be has a much stronger effect than Mg on the strain in the quaternary alloy film. As an example, in order to achieve lattice matched BeMgZnO with 40% of Mg, only about 3% of Be is needed, and the quaternary layers containing more than ~8% of Be are under tensile strain for the whole range of Mg concentrations.
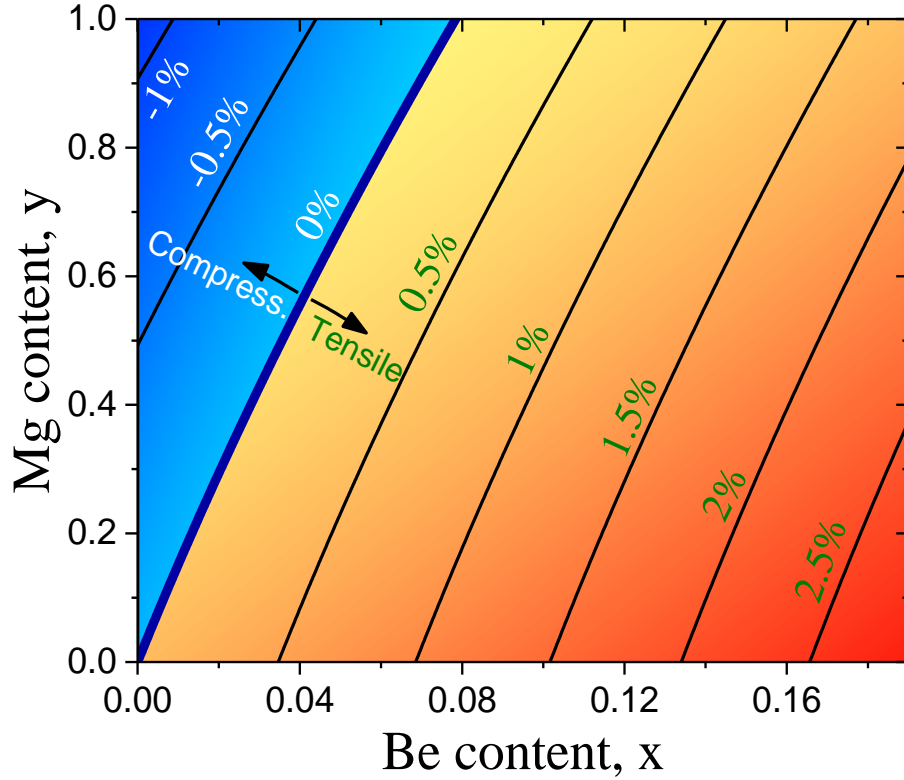
Figure 44. Strain in the Be$_x$Mg$_y$Zn$_{1-x-y}$O layer on ZnO template as a function of Be and Mg contents. The negative and the positive signs represent the compressive and tensile strain, respectively.

Alloying of ZnO with BeO and MgO gives rise to opposite signs for the changes of the in-plane lattice parameter, a, in BeO-MgO-ZnO solid solutions. The a parameter increases and decreases with increasing Mg and Be content, respectively. Therefore, by varying the Be and Mg content of BeMgZnO one can tune the in-plane lattice parameter a and thus control the sign and amount of strain in the ZnO/BeMgZnO heterostructures. This makes it possible to address the problem of limited densities ($<10^{13}$ cm^{-2}) of 2DEG in ZnO-MgO-based heterostructures.

Figure 4 with a cross-sectional schematic drawings illustrate spontaneous and piezoelectric polarization fields in Zn-polar heterostructures based on the BeO-MgO-ZnO system. At the

interfaces between the top barrier and the bottom ZnO layers of the heterostructures, the abrupt change in polarization value gives rise to a polarization sheet charge density:

$$\sigma = P_{top} - P_{bottom} \tag{31}$$

where σ is the interface polarization charge density, and P_{top} and P_{bottom} are the polarization charge densities in the top and bottom layers, respectively. If the net polarization charge is positive, screening by free electrons would cause accumulation near the interface, and thus form 2DEG.

For the Zn-polar MgZnO/ZnO heterostructure MgZnO is under compressive strain due to its larger in-plane lattice parameter than that of the relaxed ZnO buffer layer. The resulting piezoelectric polarization, P_{Pz}, in MgZnO is antiparallel to the spontaneous polarization, P_{Sp}, resulting in total polarization $P(MgZnO) = P_{Sp}(MgZnO) - P_{Pz}(MgZnO)$. Therefore, the polarization charge at the MgZnO/ZnO interface is lower as compared to the value expected for unstrained MgZnO:

$$\sigma = \left| P_{Sp}(MgZnO) \right| - \left| P_{Pz}(MgZnO) + P_{Sp}(ZnO) \right| \tag{32}$$

Addition of Be into the top MgZnO layer makes it possible to reduce the lattice parameter below that of the relaxed ZnO buffer, and therefore, reverses the sign of the piezoelectric polarization. As a result, the polarization charge at the interface increases, which is favorable for 2DEG.

$$\sigma = \left| P_{Sp}(BeMgZnO) + P_{Pz}(BeMgZnO) \right| - \left| P_{Sp}(ZnO) \right| \tag{33}$$

The spontaneous polarization can be obtained using linear interpolation between three binaries can be expressed as:

$$P_{Sp} = x P_{Sp}(BeO) + y P_{Sp}(MgO) + (1 - x - y) P_{Sp}(ZnO) \tag{34}$$

and the piezoelectric polarization can be expressed as follows:

$$P_{Pz} = 2\varepsilon_1 \left(e_{31} - e_{33} C_{13} / C_{33} \right) \tag{35}$$

where ε_1 is the biaxial in-plain strain in the top layer that is calculated as the relative difference in the in-plane lattice constants of the epitaxial layer and template (buffer or substrate) through $\varepsilon_1 = \left(a_{buffer} - a(x,y) \right) / a(x,y)$; e_{xx} are the components of the piezoelectric tensor; and C_{xx} are the elastic coefficients.

Table 11. Lattice parameters, the elastic and piezoelectric constants and spontaneous polarization P_{Sp} of the binaries BeO, MgO, and ZnO used in the calculation of the piezoelectric polarization P_{Pz} of the quaternary BeMgZnO,

	BeO	MgO	ZnO
a lattice parameter (Å)	2.698[a]	3.30[c]	3.2501[b]
C_{33} (GPa)	488[a]	109[d]	211[b]
C_{31} (GPa)	77[a]	58[d]	105[b]
e_{33} (C/m^2)	0.2[a]	1.64[d]	1.22[b]
e_{31} (C/m^2)	-0.02[a]	-0.58[d]	-0.51[b]
P_{Sp} (C/m^2)	-0.045[a]	-0.12[e]	-0.053[e]

[a] Ref. 104
[b] Ref. 31
[c] Ref. 105
[d] Ref. 106
[e] Ref. 27

The knowledge of the strain in the barrier layer allows the calculation of the 2DEG density for $Be_xMg_yZn_{1-x-y}O$/ZnO heterostructures. Figure 45 shows the dependence of calculated 2DEG sheet carrier density on Be in BeMgZnO/ZnO heterostructure with Mg content of 20% and 40%. Due to smaller lattice parameter of BeO, Be incorporation into the barrier supports the formation of 2DEG. In order to achieve carrier concentrations above 10^{13} cm^{-2} as small as 3-4% is needed in these quaternary heterostructures.
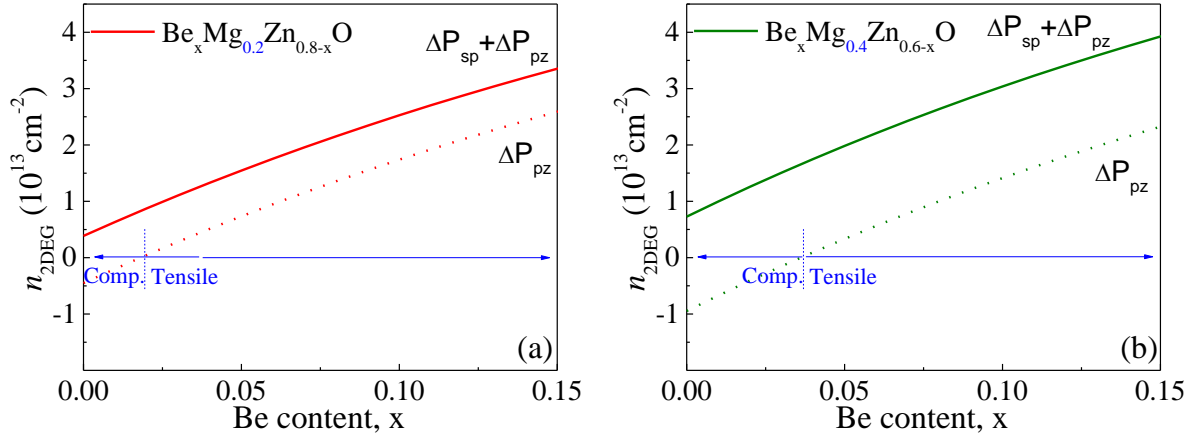
Figure 45. The dependance of calculated 2DEG carrier densities for Zn-polar (a) $Be_xMg_{0.2}Zn_{0.8-x}O/ZnO$ and (b) $Be_xMg_{0.4}Zn_{0.6-x}O/ZnO$ heterostcutres on Be conent.

In conclusion, BeMgZnO/ZnO heterostructures allow a clear advantage for the formation of high 2DEG carrier density in comparison to those in MgZnO/ZnO. As small as 3-4% of Be is sufficient to achieve carrier concentrations above 10^{13} cm^{-2} in the quaternary heterostructures with 20-40% of Mg. In fact, any amount of the Be in the barrier layer would increase the 2DEG carrier density.

Summary and Outlook

The synthesis and investigation of structural, electrical, and optical properties of quaternary BeMgZnO thin films and (Be,Mg)ZnO/ZnO heterostructures with 2DEG have been performed. Wide range of compositions (up to $Be_{0.19}Mg_{0.42}Zn_{0.39}O$ and $Be_{0.12}Mg_{0.52}Zn_{0.36}O$), bandgaps (from 3.3 eV to 5.2 eV) and a lattice parameters (from 3.27 Å to 3.16 Å, the latter one is equal to 2.8% strain) were achieved. Despite high Be and Mg contents that are not achievable with ternary BeZnO and MgZnO, the solubility limit in the quaternary alloy has not yet been reached; which is also evidence of the positive effect of Be and Mg atoms on each other's incorporation and stabilization in the lattice of ZnO.

The effect of metal-to-oxygen ratio on the surface morphology and electrical properties was investigated. It was found that samples grown under slightly oxygen rich conditions exhibit the lowest surface RMS roughness. Additionally, samples grown under O-rich conditions are insulating and samples grown under metal rich conditions are semiconducting. For FET applications, the lowers surface roughness and the highest crystal quality are desired. On the other hand, for TCO applications, doping possibilities and high conductivity are main concerns and for solar blind photodetectors low background conductivity may be an advantage. Therefore, the optimum metal-to-oxygen ratio depends on the use of the BeMgZnO alloy and may require additional tuning of its properties for the specific application.

The steady state and time-resolved measurements revealed that the carrier localization is in the inverse proportionality with Mg/Be ratio (at least up to Mg/Be = 6). This effect is observed due to compensation effects between Be and Mg atoms in the lattice of ZnO. Similar correlation is observed in the temporal redshift of the PL peak position that originates from removal of the band filling effect in the localized states. Based on steady state PL measurements at room and low

temperatures, it was found that optimum Be/Mg ratio for the room temperature optical performance is about 2.5.

For device fabrication it is necessary to have control over contact formation. Specific contact resistivity below 10^{-6} Ohm-cm^2 for 10^{18} cm^{-3} for ohmic contact to ZnO was realized. The optimum rapid thermal annealing conditions in the N$_2$ environment were found to be near 525 ℃, 10 seconds or 500 ℃, 20 seconds. In regard to Schottky contact, the presence of high density surface carrier concentration is responsible for Fermi level pinning which is responsible for limited height of the Schottky barrier. Further optimization of surface preparation prior metal deposition or utilization of metal deposition techniques with in situ oxygen plasma treatment is necessary. In regard to BeMgZnO, due to lower work function of BeO and MgO in comparison to that of ZnO, it is easier to form high Schottky barrier to the quaternary alloy. The latter one would be true only if high surface carrier concentration is eliminated. It is essential to find proper surface treatment to remove high defect density and maintain the functionality of the structures.

The investigation of O-polar MgZnO/ZnO heterostructures has shown that 2DEG electron densities are limited to 7.5 x 10^{12} cm^{-2} (for 45% of Mg). The advantage of BeMgZnO-based heterostructures to those based on MgZnO are that the first ones provide for the possibility to tune the piezoelectric polarization in a wide range by changing the in-plane lattice parameter of the barrier alloy and thus achieve high two-dimensional carrier densities at the interface. Due to larger *a* lattice parameters of MgZnO then that of ZnO, any amount of Be would play a beneficial role in the formation of 2DEG because of compressive strain compensation in the ternary barrier. It is shown that even small amount of Be (few %) would result in significant improvement in 2DEG carrier densities and values above 10^{13} cm^{-2}. The insertion of the very thin BeO interfacial layer may have a favorable influence on the device performance (similar to AlN layer in

AlGaN/AlN/GaN HFETs) and require further investigation with numerical simulations and fabrication experiments.

References

[1] Ü. Özgür, Y.I. Alivov, C. Liu, A. Teke, M.A. Reshchikov, S. Doğan, V. Avrutin, S.-J. Cho, and H. Morkoç, J. Appl. Phys. **98**, 041301 (2005).

[2] Y. Kozuka, A. Tsukazaki, and M. Kawasaki, Appl. Phys. Rev. **1**, 011303 (2014).

[3] Q. Yan, P. Rinke, M. Winkelnkemper, A. Qteish, D. Bimberg, M. Scheffler, and C.G. Van de Walle, Appl. Phys. Lett. **101**, 152105 (2012).

[4] A. Ohtomo, M. Kawasaki, T. Koida, K. Masubuchi, H. Koinuma, Y. Sakurai, Y. Yoshida, T. Yasuda, and Y. Segawa, Appl. Phys. Lett. **72**, 2466 (1998).

[5] A.K. Sharma, J. Narayan, J.F. Muth, C.W. Teng, C. Jin, A. Kvit, R.M. Kolbas, and O.W. Holland, Appl. Phys. Lett. **75**, 3327 (1999).

[6] X. Du, Z. Mei, Z. Liu, Y. Guo, T. Zhang, Y. Hou, Z. Zhang, Q. Xue, and A.Y. Kuznetsov, Adv. Mater. **21**, 4625 (2009).

[7] S. Choopun, R.D. Vispute, W. Yang, R.P. Sharma, T. Venkatesan, and H. Shen, Appl. Phys. Lett. **80**, 1529 (2002).

[8] Y.R. Ryu, T.S. Lee, J.A. Lubguban, A.B. Corman, H.W. White, J.H. Leem, M.S. Han, Y.S. Park, C.J. Youn, and W.J. Kim, Appl. Phys. Lett. **88**, 052103 (2006).

[9] M. Chen, Y. Zhu, L. Su, Q. Zhang, A. Chen, X. Ji, R. Xiang, X. Gui, T. Wu, B. Pan, and Z. Tang, Appl. Phys. Lett. **102**, 202103 (2013).

[10] L. Su, Y. Zhu, M. Chen, Q. Zhang, Y. Su, X. Ji, T. Wu, X. Gui, R. Xiang, and Z. Tang, Appl. Phys. Lett. **103**, 072104 (2013).

[11] B. Cordero, V. Gómez, A.E. Platero-Prats, M. Revés, J. Echeverría, E. Cremades, F. Barragán, and S. Alvarez, Dalton Trans. 2832 (2008).

[12] M. Toporkov, V. Avrutin, S. Okur, N. Izyumskaya, D. Demchenko, J. Volk, D.J. Smith, H. Morkoç, and Ü. Özgür, J. Cryst. Growth **402**, 60 (2014).

[13] D. Ye, Z. Mei, H. Liang, Y. Liu, A. Azarov, A. Kuznetsov, and X. Du, J. Phys. Appl. Phys. **47**, 175102 (2014).

[14] C. Yang, X.M. Li, Y.F. Gu, W.D. Yu, X.D. Gao, and Y.W. Zhang, Appl. Phys. Lett. **93**, 112114 (2008).

[15] L. Su, Y. Zhu, Q. Zhang, M. Chen, X. Ji, T. Wu, X. Gui, B. Pan, R. Xiang, and Z. Tang, J. Phys. Appl. Phys. **46**, 245103 (2013).

[16] C. Yang, X.M. Li, X.D. Gao, X. Cao, R. Yang, and Y.Z. Li, J. Cryst. Growth **312**, 978 (2010).

[17] L. Su, Y. Zhu, D. Yong, M. Chen, X. Ji, Y. Su, X. Gui, B. Pan, R. Xiang, and Z. Tang, ACS Appl. Mater. Interfaces **6**, 14152 (2014).

[18] C. Yang, X.M. Li, Y.F. Gu, W.D. Yu, X.D. Gao, and Y.W. Zhang, Appl. Phys. Lett. **93**, 112114 (2008).

[19] L. Su, Y. Zhu, Q. Zhang, M. Chen, T. Wu, X. Gui, B. Pan, R. Xiang, and Z. Tang, Appl. Surf. Sci. **274**, 341 (2013).

[20] N. Panwar, J. Liriano, and R.S. Katiyar, J. Alloys Compd. **509**, 1222 (2011).

[21] S.S. Chen, X.H. Pan, W. Chen, H.H. Zhang, W. Dai, P. Ding, J.Y. Huang, B. Lu, and Z.Z. Ye, Appl. Phys. Lett. **105**, 122112 (2014).

[22] L. Su, Y. Zhu, D. Yong, M. Chen, X. Ji, Y. Su, X. Gui, B. Pan, R. Xiang, and Z. Tang, ACS Appl. Mater. Interfaces **6**, 14152 (2014).

[23] C. Yang, X.M. Li, W.D. Yu, X.D. Gao, X. Cao, and Y.Z. Li, J. Phys. Appl. Phys. **42**, 152002 (2009).

[24] J.-H. Park, H.B. Cuong, S.-H. Jeong, and B.-T. Lee, J. Alloys Compd. **615**, 126 (2014).

[25] H.-Y. Lee, H.-Y. Chang, L.-R. Lou, and C.-T. Lee, IEEE Photonics Technol. Lett. **25**, 1770 (2013).

[26] R. Vettumperumal, S. Kalyanaraman, and R. Thangavel, J. Sol-Gel Sci. Technol. **68**, 334 (2013).

[27] S.-H. Jang and S.F. Chichibu, J. Appl. Phys. **112**, 073503 (2012).

[28] Q. Yan, P. Rinke, M. Winkelnkemper, A. Qteish, D. Bimberg, M. Scheffler, and C.G. Van de Walle, Appl. Phys. Lett. **101**, 152105 (2012).

[29] M. Shishkin and G. Kresse, Phys. Rev. B **75**, 235102 (2007).

[30] F. Oba, A. Togo, I. Tanaka, J. Paier, and G. Kresse, Phys. Rev. B **77**, 245202 (2008).

[31] Hadis Morkoç and Ümit Özgür, *Zinc Oxide: Fundamentals, Materials and Device Technology* (Wiley-VCH, Weinheim, 2009).

[32] E.H. Kisi and M.M. Elcombe, Acta Crystallogr. C **45**, 1867 (1989).

[33] S. Limpijumnong and W.R.L. Lambrecht, Phys. Rev. B **63**, 104103 (2001).

[34] K. Koike, K. Hama, I. Nakashima, G. Takada, K. Ogata, S. Sasa, M. Inoue, and M. Yano, J. Cryst. Growth **278**, 288 (2005).

[35] K. Shimada, N. Takahashi, Y. Nakagawa, T. Hiramatsu, and H. Kato, Phys. Rev. B **88**, (2013).

[36] M. Shishkin, M. Marsman, and G. Kresse, Phys. Rev. Lett. **99**, 246403 (2007).

[37] J. Heyd, J.E. Peralta, G.E. Scuseria, and R.L. Martin, J. Chem. Phys. **123**, 174101 (2005).

[38] C.F. Klingshirn, A. Waag, A. Hoffmann, and J. Geurts, *Zinc Oxide: From Fundamental Properties Towards Novel Applications*, 2010 edition (Springer, Heidelberg ; London, 2010).

[39] O. Madelung, in *II-VI -VII Compd. Semimagn. Compd.*, edited by U. Rössler and M. Schulz (Springer-Verlag, Berlin/Heidelberg, 1999), pp. 1–6.

[40] D.M. Roessler and W.C. Walker, Phys. Rev. **159**, 733 (1967).

[41] E.D. Palik and G. Ghosh, editors , *Handbook of Optical Constants of Solids* (Academic Press, San Diego, 1998).

[42] S.F. Ding, G.H. Fan, S.T. Li, K. Chen, and B. Xiao, Phys. B Condens. Matter **394**, 127 (2007).

[43] B. Amrani, F.E.H. Hassan, and H. Akbarzadeh, J. Phys. Condens. Matter **19**, 436216 (2007).

[44] L. Shi, Y. Qin, J. Hu, Y. Duan, L. Qu, L. Wu, and G. Tang, EPL Europhys. Lett. **106**, 57001 (2014).

[45] E.L. Shirley, J.A. Soininen, and J.J. Rehr, in edited by R. Soufli and J.F. Seely (2004), pp. 125–137.

[46] R.M. Hazen and L.W. Finger, J. Appl. Phys. **59**, 3728 (1986).

[47] J.W. Downs, F.K. Ross, and G.V. Gibbs, Acta Crystallogr. B **41**, 425 (1985).

[48] D.M. Roessler, W.C. Walker, and E. Loh, J. Phys. Chem. Solids **30**, 157 (1969).

[49] J. Falson, D. Maryenko, Y. Kozuka, A. Tsukazaki, and M. Kawasaki, Appl. Phys. Express **4**, 091101 (2011).

[50] A. Tsukazaki, S. Akasaka, K. Nakahara, Y. Ohno, H. Ohno, D. Maryenko, A. Ohtomo, and M. Kawasaki, Nat. Mater. **9**, 889 (2010).

[51] H. Tampo, H. Shibata, K. Maejima, A. Yamada, K. Matsubara, P. Fons, S. Kashiwaya, S. Niki, Y. Chiba, T. Wakamatsu, and H. Kanie, Appl. Phys. Lett. **93**, 202104 (2008).

[52] T.S. Herng, A. Kumar, C.S. Ong, Y.P. Feng, Y.H. Lu, K.Y. Zeng, and J. Ding, Sci. Rep. **2**, (2012).

[53] S.K. Hong, H.J. Ko, Y. Chen, T. Hanada, and T. Yao, J. Vac. Sci. Technol. B **18**, 2313 (2000).

[54] M. B. Ullah, V. Avrutin, S. Li, S. Das, M. Monavarian, M. Toporkov, Ü. Özgür, P. Ruterana, H. Morkoç, (n.d.).

[55] M. Toporkov, V. Avrutin, S. Okur, N. Izyumskaya, D. Demchenko, J. Volk, D.J. Smith, H. Morkoç, and Ü. Özgür, J. Cryst. Growth **402**, 60 (2014).

⁵⁶ H.-L. Shi and Y. Duan, Eur. Phys. J. B **66**, 439 (2008).

⁵⁷ F. Wang, S.-S. Li, J.-B. Xia, H.X. Jiang, J.Y. Lin, J. Li, and S.-H. Wei, Appl. Phys. Lett. **91**, 061125 (2007).

⁵⁸ J.H. Yu, D.S. Park, J.H. Kim, T.S. Jeong, C.J. Youn, and K.J. Hong, J. Mater. Sci. **45**, 130 (2009).

⁵⁹ Z. Zolnai, M. Toporkov, J. Volk, D.O. Demchenko, S. Okur, Z. Szabó, Ü. Özgür, H. Morkoç, V. Avrutin, and E. Kótai, Appl. Surf. Sci. **327**, 43 (2015).

⁶⁰ M.D. Neumann, C. Cobet, N. Esser, B. Laumer, T.A. Wassner, M. Eickhoff, M. Feneberg, and R. Goldhahn, J. Appl. Phys. **110**, 013520 (2011).

⁶¹ R. Schmidt, B. Rheinländer, M. Schubert, D. Spemann, T. Butz, J. Lenzner, E.M. Kaidashev, M. Lorenz, A. Rahm, H.C. Semmelhack, and M. Grundmann, Appl. Phys. Lett. **82**, 2260 (2003).

⁶² X. Su, P. Si, Q. Hou, X. Kong, and W. Cheng, Phys. B Condens. Matter **404**, 1794 (2009).

⁶³ Z. Zolnai, M. Toporkov, J. Volk, D. O. Demchenko, V. Avrutin, S. Okur, Z. Szabó, H. Morkoç, and Ü. Özgür, (n.d.).

⁶⁴ J.A. Dean and N.A. Lange, *Lange's Handbook of Chemistry*, 15th ed (McGraw-Hill, New York, 1999).

⁶⁵ B. Lee and L.-W. Wang, Phys. Rev. B **73**, 153309 (2006).

⁶⁶ B. Lee and L.W. Wang, J. Appl. Phys. **100**, 093717 (2006).

⁶⁷ M. Toporkov, D.O. Demchenko, Z. Zolnai, J. Volk, V. Avrutin, H. Morkoç, and Ü. Özgür, J. Appl. Phys. **119**, 095311 (2016).

⁶⁸ J.P. Perdew, K. Burke, and M. Ernzerhof, Phys. Rev. Lett. **77**, 3865 (1996).

⁶⁹ J.P. Perdew, Phys. Rev. Lett. **55**, 1665 (1985).

⁷⁰ X. Du, Z. Mei, Z. Liu, Y. Guo, T. Zhang, Y. Hou, Z. Zhang, Q. Xue, and A.Y. Kuznetsov, Adv. Mater. **21**, 4625 (2009).

⁷¹ H. Kato, M. Sano, K. Miyamoto, and T. Yao, J. Cryst. Growth **275**, e2459 (2005).

⁷² S.V. Ivanov, A. El-Shaer, T.V. Shubina, S.B. Listoshin, A. Bakin, and A. Waag, Phys. Status Solidi C **4**, 154 (2007).

⁷³ M. Toporkov, D. Demchenko, Z. Zolnai, J. Volk, V. Avrutin H. Morkoç, Ü. Özgür, J Appl Phys (2016).

⁷⁴ D.O. Demchenko, I.C. Diallo, and M.A. Reshchikov, J. Appl. Phys. **119**, 035702 (2016).

⁷⁵ A. Chernikov, S. Horst, M. Koch, K. Volz, S. Chatterjee, S.W. Koch, T.A. Wassner, B. Laumer, and M. Eickhoff, Phys. Status Solidi C **8**, 1149 (2011).

⁷⁶ T. Makino, N.T. Tuan, H.D. Sun, C.H. Chia, Y. Segawa, M. Kawasaki, A. Ohtomo, K. Tamura, T. Suemoto, H. Akiyama, M. Baba, S. Saito, T. Tomita, and H. Koinuma, Appl. Phys. Lett. **78**, 1979 (2001).

⁷⁷ I.A. Buyanova, J.P. Bergman, G. Pozina, W.M. Chen, S. Rawal, D.P. Norton, S.J. Pearton, A. Osinsky, and J.W. Dong, Appl. Phys. Lett. **90**, 261907 (2007).

⁷⁸ M.A. Reshchikov, G.-C. Yi, and B.W. Wessels, Phys. Rev. B **59**, 13176 (1999).

⁷⁹ L. Su, Y. Zhu, D. Yong, M. Chen, X. Ji, Y. Su, X. Gui, B. Pan, R. Xiang, and Z. Tang, ACS Appl. Mater. Interfaces **6**, 14152 (2014).

⁸⁰ P.G. Eliseev, P. Perlin, J. Lee, and M. Osiński, Appl. Phys. Lett. **71**, 569 (1997).

⁸¹ T. Lu, Z. Ma, C. Du, Y. Fang, H. Wu, Y. Jiang, L. Wang, L. Dai, H. Jia, W. Liu, and H. Chen, Sci. Rep. **4**, 6131 (2014).

⁸² H.J. Ko, Y.F. Chen, Z. Zhu, T. Yao, I. Kobayashi, and H. Uchiki, Appl. Phys. Lett. **76**, 1905 (2000).

83 Z.L. Liu, Z.X. Mei, R. Wang, J.M. Zhao, H.L. Liang, Y. Guo, A.Y. Kuznetsov, and X.L. Du, J. Phys. Appl. Phys. **43**, 285402 (2010).

84 M.D. Neumann, C. Cobet, N. Esser, B. Laumer, T.A. Wassner, M. Eickhoff, M. Feneberg, and R. Goldhahn, J. Appl. Phys. **110**, 013520 (2011).

85 D. Rosales, B. Gil, T. Bretagnon, B. Guizal, F. Zhang, S. Okur, M. Monavarian, N. Izyumskaya, V. Avrutin, Ü. Özgür, H. Morkoç, and J.H. Leach, J. Appl. Phys. **115**, 073510 (2014).

86 R. Heinhold, G.T. Williams, S.P. Cooil, D.A. Evans, and M.W. Allen, Phys. Rev. B **88**, 235315 (2013).

87 L.J. Brillson and Y. Lu, J. Appl. Phys. **109**, 121301 (2011).

88 R.-H. Chang, K.-C. Yang, T.-H. Chen, L.-W. Lai, T.-H. Lee, S.-L. Yao, and D.-S. Liu, J. Nanomater. **2013**, e560542 (2013).

89 C.S. Singh, G. Agarwal, G. Durga Rao, S. Chaudhary, and R. Singh, Mater. Sci. Semicond. Process. **14**, 1 (2011).

90 S.K. Mohanta, A. Nakamura, G. Tabares, A. Hierro, Á. Guzmán, E. Muñoz, and J. Temmyo, Thin Solid Films **548**, 539 (2013).

91 R. Schifano, E.V. Monakhov, U. Grossner, and B.G. Svensson, Appl. Phys. Lett. **91**, 193507 (2007).

92 S.K. Mohanta, A. Nakamura, G. Tabares, A. Hierro, Á. Guzmán, E. Muñoz, and J. Temmyo, Thin Solid Films **548**, 539 (2013).

93 H.L. Mosbacker, S.E. Hage, M. Gonzalez, S.A. Ringel, M. Hetzer, D.C. Look, G. Cantwell, J. Zhang, J.J. Song, and L.J. Brillson, J. Vac. Sci. Technol. B **25**, 1405 (2007).

94 S. Müller, H. von Wenckstern, F. Schmidt, D. Splith, R. Heinhold, M. Allen, and M. Grundmann, J. Appl. Phys. **116**, 194506 (2014).

95 M.W. Allen, R.J. Mendelsberg, R.J. Reeves, and S.M. Durbin, Appl. Phys. Lett. **94**, 103508 (2009).

96 N.R.C. Raju, K.J. Kumar, and A. Subrahmanyam, J. Phys. Appl. Phys. **42**, 135411 (2009).

97 M.W. Allen, M.M. Alkaisi, and S.M. Durbin, Appl. Phys. Lett. **89**, 103520 (2006).

98 M.W. Allen, S.M. Durbin, and J.B. Metson, Appl. Phys. Lett. **91**, 053512 (2007).

99 M.W. Allen, Schottky Contact Formation to Bulk Zinc Oxide, 2008.

100 J.H. Lee, C.H. Kim, A.R. Kim, H.S. Kim, N.W. Jang, Y. Yun, J.-G. Kim, M.W. Pin, and W.J. Lee, Jpn. J. Appl. Phys. **51**, 09MF07 (2012).

101 Z.L. Wang and J. Song, Science **312**, 242 (2006).

102 K.D. Jordan and R. Seeger, Chem. Phys. Lett. **54**, 320 (1978).

103 A. Matulionis, J. Liberis, I. Matulioniene, M. Ramonas, and E. Sermuksnis, Proc. IEEE **98**, 1118 (2010).

104 T. Hanada, in *Oxide Nitride Semicond.*, edited by P.T. Yao and P.D.S.-K. Hong (Springer Berlin Heidelberg, 2009), pp. 1–19.

105 Q. Xu, X.-W. Zhang, W.-J. Fan, S.-S. Li, and J.-B. Xia, Comput. Mater. Sci. **44**, 72 (2008).

106 P. Gopal and N.A. Spaldin, J. Electron. Mater. **35**, 538 (2006).

Curriculum Vitae

Mykyta Toporkov

DOB: November 23, 1989

Nationality: Ukrainian

email: toporkovm@vcu.edu

Education

2016 Ph.D., Virginia Commonwealth University, Richmond, VA / Department of Electrical and Computer Engineering

2012 B.Sc., Kharkiv National University of Radio Electronics, Ukraine / Department of Electrical Engineering

Publication List

Journal Papers

- R. B. Green, **M. Toporkov**, M. B. Ullah, V. Avrutin, Ü. Özgür, H. Morkoç, E. Topsakal. "*An Alternative Material for Transparent Antennas for Commercial and Medical Applications,*" submitted to IEEE Antennas Wireless Propag. Lett., April 4, 2016

- M. B. Ullah, V. Avrutin, S. Li, S. Das, M. Monavarian, **M. Toporkov**, Ü. Özgür, P. Ruterana, H. Morkoç, "*Polarity Control and Residual Strain in ZnO Epilayers Grown by Molecular Beam Epitaxy on (0001)-GaN/Sapphire,*" submitted to Appl. Phys. Lett., March 22, 2016.

- **M. Toporkov**, D. Demchenko, Z. Zolnai, J. Volk, V. Avrutin H. Morkoç, Ü. Özgür, "*Lattice Parameters and Electronic Structure of BeMgZnO Quaternary Solid Solutions: Experiment and Theory,*" J. Appl. Phys., **119**, 095311 (2016)

- E. Sermuksnis, J. Liberis, M. Ramonas, A. Matulionis, **M.Toporkov**, H.Liu, V.Avrutin, Ü. Özgür, H. Morkoç, "*Hot-electron energy relaxation time in Ga-doped ZnO films,*" J. Appl. Phys., **117**, 065704 (2015)

- Z. Zolnai, **M. Toporkov**, J. Volk, D. Demchenko, S. Okur, Z. Szabó, Ü. Özgür, H. Morkoç, V. Avrutin, E. Kótai, "*Nondestructive atomic compositional analysis of BeMgZnO quaternary alloys using ion beam analytical techniques,*" Appl. Surf. Sci. **327**, 43 (2015)

- **M. Toporkov**, V. Avrutin, S. Okur, N. Izyumskaya, D. Demchenko, J. Volk, D. J. Smith, H. Morkoç, Ü. Özgür, "*Enhancement of Be and Mg incorporation in wurtzite quaternary BeMgZnO alloys with up to 5.1 eV optical bandgap,*" J. Cryst. Growth **402**, 60 (2014)

Conferences and Proceedings

- SPIE Photonics West, USA, February 13, 2016
    - **M. Toporkov**, S. Hafiz, MD B. Ullah, N. Tanner, V. Avrutin, H. Morkoç, and Ü. Özgür, "*Exciton Localization and Large Stokes Shift in Quaternary BeMgZnO Grown by Molecular Beam Epitaxy,*" Spie-Int Soc Optical Engineering, **9749**, 974910 (2016)

- 23rd International Conference on Noise and Fluctuations, China, June 2, 2015
    - E. Sermuksnis, J. Liberis, A. Matulionis, **M. Toporkov**, V. Avrutin, U. Ozgur, H. Morkoc, "*Hot-electron noise and energy relaxation in wurtzite ZnO,*" Int. Conf. Noise Fluct. ICNF, pp. 1-4 (2015)

- 8th International Workshop on Zinc Oxide and Related Materials, Canada, September 7, 2014

- o **M. Toporkov**, B. Ullah, V. Avrutin, D. Demchenko, J. Volk, Z. Zolnai, H. Morkoc and U. Ozgur, "Wide bandgap quaternary BeMgZnO for ZnO-based heterostructures with high two-dimensional electron gas density"

- o E. Sermuksnis, J. Liberis, A. Matulionis, **M. Toporkov**, H. Liu, V. Avrutin, N. Izyumskaya, U. Ozgur and H. Morkoc, "Electron Energy Relaxation Time in n-Type Wurtzite ZnO"

- MRS Fall Meeting Symposium, USA, December 1, 2013

  - o **M. Toporkov**, S. Okur, N. Izyumskaya, V. Avrutin, D. Demchenko, U. Ozgur, and H. Morkoc. "Effect of plasma-enhanced MBE growth conditions on structural and optical properties of quaternary alloy BeMgZnO films"

- 16th International Symposium on Technology and Young People in the 21st Century, Ukraine, April 7-19, 2012

  - o **M. Toporkov** and O. Soroka, "Microwave resonant converter for investigation of layered dielectric materials"